UNIVERSITÉ DU LUXEMBOURG

PhD-FSTM-2024-049

The Faculty of Science, Technology and Medicine

DISSERTATION

Defence held on 07/06/2024 in Luxembourg

to obtain the degree of

DOCTEUR DE L'UNIVERSITÉ DU LUXEMBOURG EN *SCIENCES DE L'INGÉNIEUR*

by

Tahmineh ADILI

Born on 16 November 1990 in Langroud, (Iran, Islamic Republic of)

THERMAL HYDRAULIC ANALYSIS FOR ENHANCING PASSIVE HEAT REMOVAL SYSTEMS

Dissertation defence committee

Dr Stephan LEYER, dissertation supervisor

Professor, Université du Luxembourg

Dr Giuseppe BONFIGLI

Professor, Technische Hochschule Deggendorf

Dr Frank SCHOLZEN, Chairman

Professor, Université du Luxembourg

Dr Michael BUCK

Universität Stuttgart

Dr Manfred GREGER, Vice Chairman

Emeritus Professor, Université du Luxembourg

Abstract

Nuclear power plants play a pivotal role in satisfying worldwide energy requirements, aiding industrial operations, fostering economic development, and minimizing carbon emissions. The importance of nuclear safety has been heightened by past events such as Chernobyl and Fukushima, emphasizing the continual need for advancements in safety systems and regulations. This study concentrates on elevating the safety standards of nuclear power plants, with a specific focus on the emergency condenser (EC) within the passive safety system of the KERENA reactor.

The EC, a critical component in this context, plays a pivotal role in removing decay heat from the reactor core during emergencies. However, challenges arise in accurately predicting the thermal performance of the EC's secondary side, prompting questions regarding heat transfer models, numerical approaches, empirical models, and cost-effective methods for analyzing thermal-hydraulic behavior.

This thesis aims to improve the predictive and computational modeling capabilities of the thermal-hydraulic dynamics on the secondary side of ECs. A comprehensive review of contemporary heat transfer models is conducted, evaluating their applicability based on experimental data from the COSMEA and NOKO test facilities. Computational Fluid Dynamics (CFD) methods are explored to analyze temperature stratification, with a focus on addressing computational challenges and determining acceptable simplifications.

Recognizing the prevalent use of 1D codes in nuclear applications, efforts are made to develop a practical heat transfer model for integration into these codes, enhancing the precision of simulations. Additionally, the study explores the integration of Artificial Neural Networks (ANN) to model thermal-hydraulic dynamics, leveraging the universal applicability of artificial intelligence.

The findings of this research aim to provide valuable insights for optimizing the efficiency of emergency condenser systems, mitigating the risk of failures, and bolstering the safety of nuclear power plants. By addressing the identified questions and challenges, this thesis contributes to the broader goal of ensuring the reliability and sustainability of nuclear energy as a secure solution for meeting industrial energy demands in the future.

Nomenclature

Roman letters

A	Area [m²]	$\dot{q}$	Specific heat flux [kW/m²]
a	Thermal diffusivity [m²/s]	Re	Reynolds number
C	Constant	Ra	Rayleigh number
c_p	Specific heat at constant pressure [J/(kg K)]	r	Radius [m]
D	Diameter [m]	r	Specific heat of vaporization [KJ/mol]
D_h	Hydraulic diameter [m]	S	Momentum source [N/m³]
Gr	Grashof number	s	Length coordinate [m]
g	Gravitational constant [9.81m/s²]	T	Temperature [K]
H	Enthalpy (J/kg)	t	Time [s]
h	Heat transfer coefficient [W/(m²K)]	u	Velocity [m/s]
Δi_{lv}	Latent heat [J/kg]	X_{tt}	Martinelli number
Ja	Jakob number	x	Steam quality
L	Characteristic length [m]	***Greek***	
m	Mass [kg]	Γ	Interphase volumetric mass exchange [kg/(m³s)]
$\dot{m}$	Mass flow [kg/s]	α	Gas volume fraction
Nu	Nusselt number	ε	Void fraction
Pr	Prandtl number	$\varepsilon_{mod.}$	Modified void factor
p	Pressure	θ	Stratified angle [°]
p_{op}	Operating pressure	λ	Thermal conductivity [W/(mK)]
D	Diameter [m]	μ	Dynamic viscosity [kg/(ms)]

Subscripts

$mean$	Average	ρ	Density [kg/m³]
sec	Secondary side	σ	Surface tension [N/m]
sat	Saturation condition	τ	Shear stress [N/m²]
$turb$	Turbulent	δ	Film thickness [m]
F	Fluid		
g	Gas		
i	Interface		
l	Liquid		
m	Mixture		
v	Vapor		
w	Wall		

Abbreviations

COSMEA	COndenSation test rig for flow Morphology and hEAt transfer
HZDR	Helmholtz-Zentrum Dresden-Rossendorf
BWR	Boiling water reactor
HTC	Heat transfer coefficient
CFD	Computational fluid dynamic

CV	Control volume
EC	Emergency condenser
IAEA	International Atomic Energy Agency
CCC	Containment cooling condenser
PPPT	Passive pressure pulse transmitter
RPV	Reactor pressure vessel
INKA	Integral Teststand Karlstein
ANN	Artificial neural network
HX	Heat Exchanger

Contents

Acknowledgements

I am overflowing with gratitude for all the support and kindness extended to me on this journey. At the forefront, I am immensely grateful for the invaluable support and guidance provided by my supervisor, Prof. Stephan Leyer, throughout this journey. His continuous support and insightful advice have been invaluable in my research experience. The opportunity to join his research group in University of Luxembourg has been a privilege, and I am thankful for the enriching experiences it has offered.

I would like to thank Prof. Giuseppe Bonfigli, Prof. Manfred Greger and Dr. Michael Buck for their insightful advice and fruitful discussions. Their willingness to share their knowledge and engage in fruitful discussions has been precious for me. I would also like to thank Prof. Frank Scholzen for agreeing to be part of my thesis committee.

I am also deeply appreciative of the collaborative spirit within the applied thermodynamic group. My colleagues, including Dr. Filip Janasz, Dr. Iurii Dolganov, Dr. Veronika Wolf, Dr. Marie-Alix Dalle, Dr. Ali Arababadi, Dr. Yu Zhang, Dr. Karthick Paneer Selvam, and the rest of the team, have provided invaluable insights and support. A special thank goes to Dr. Tobias Jäger for his support and friendship since I joined the group.

The first two years of this work was dedicated to PANAS project funded by Federal Ministry of Education and Research (BMBF) in Germany. The calculations of this study have been carried out using the HPC facility at the University of Luxembourg.

My time at the University of Luxembourg has been more meaningful by the incredible friendships I have found. Their laughter and encouragement have infused my days with joy and purpose.

Lastly, I want to extend my deepest appreciation to my family especially my father, whose consistent support and encouragement have been a constant source of strength throughout my life. To my sister, Tahereh, and my brother, Vahid, whose presence has been a comforting shelter, always ready to lend an ear, warm my heart, and offer words of encouragement. And to my partner, Martin, who entered my life during the most challenging phase of this journey, his reliable support and encouragement have been making the difficult moments more bearable and the triumphs all the sweeter.

Luxembourg, May 2024

Tahmineh Adili

List of Figures

List of Tables

1 Introduction and Motivation

Nuclear Power plants play a major role in meeting the energy demands of the world, providing a stable and efficient source of electricity. As the end of 2022, there were a total of 411 functioning nuclear reactors globally [2]. Their capacity for large-scale power generation contributes significantly to industrial processes, leading to economic growth as well as reducing carbon emissions compared to traditional fossil fuel alternatives [3]. This rises the importance of nuclear safety in the design and operation of nuclear power plants. Even though safety improvements and developments have been always a central role in this field, accidents like Chernobyl in 1986 and Fukushima Daiichi in 2011, raised concerns and questions about the reliability of safety systems and regulations in nuclear energy [4]. Therefore, enhancing the safety of nuclear power plants in different aspects is now more necessary to restore confidence in the viability of nuclear energy as a secure and sustainable solution for meeting industrial energy demands. By prioritizing safety enhancements, we not only mitigate potential risks but also increase public confidence in the reliability and sustainability of nuclear energy as a crucial power source for the future.

The history of nuclear energy starts from the first generation of nuclear reactors called Gen I built in Soviet Union, France and the United states between 1950s to the early 1960s. Subsequently, the field experienced a continuous evolution, leading to the emergence of distinct generations of nuclear reactors, namely Gen I, Gen II, Gen III, Gen III+, and Gen IV [4]. Within the realm of Gen II reactors, safety systems were predominantly designed based on external forces, whether electrical or mechanical, constituting what are commonly referred to as active safety systems. However, pivotal incidents as mentioned earlier such as those in Chernobyl and Fukushima prompted a paradigm shift. The concept of passive safety systems was introduced, marking a significant advancement in reactor safety. This shift laid the foundation for the development of Gen III and Gen III+ reactors. While maintaining the fundamental characteristics of Gen II reactors, these newer generations incorporated improvements in safety systems by integrating passive safety measures and enhancement in thermal efficiency of these reactors. Gen IV reactors

were later developed in this field with the focus on minimizing waste, increasing the safety and economical sufficiency [4].

Within the framework of Gen III reactors, the utilization of a medium-capacity Boiling Water Reactor (BWR) is exemplified by the KERENA reactor, formerly designated as SWR1000. This reactor predominantly employs passive safety systems distributed across various components [5].

The definition provided by the IAEA for the term "passive" encompasses the following: A passive component does not need an external action or energy supply; any components that are not passive are considered active. Furthermore, a passive system is identified as either one equipped entirely with passive components and structures, or one employing minimal active components to trigger subsequent passive operation [6]. The activation of it is dependent to the requisite presence of both a heat sink and a heat source, as delineated in Figure 1-1 [7].

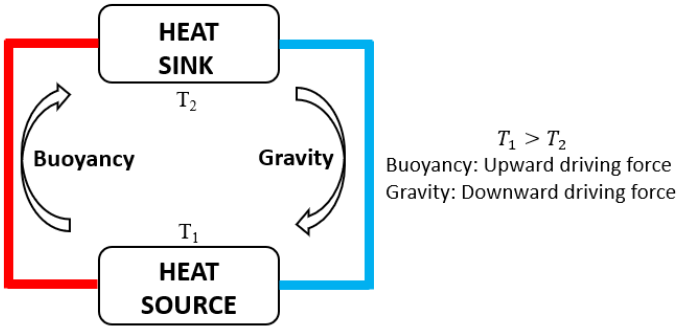

Figure 1-1. Schematic of natural circulation

In addition to increasing the reliability within passive safety systems due to their autonomous activation, which avoids any manual or automated intervention, their utilization proves economically advantageous. This stems from the simplified installation and maintenance protocols inherent in passive safety systems when compared with the more intricate demands associated with active safety systems [8].

The main components of passive safety system in KERENA^{TM} reactor are shown in Figure 1-2. The most important passive safety components in KERENA reactor are Emergency condenser (EC), Containment Cooling Condenser (CCC) and Passive Pulse Pressure Transmitter (PPPT). They are crucial for preventing core damage in case of an accident. These safety systems rely on condensation and evaporation in inclined pipes [9]. The ECs activate when the water level drops

in the reactor pressure vessel (RPV), removing decay heat and transferring it to a flooding pool. The CCC further condenses evaporated steam from the pool. The Passive Pulse Pressure Transmitter (PPPT) automatically triggers safety measures without external power. It's a heat exchanger connected to the reactor vessel, and if water level drops, steam activates it, leading to pressure increase and safety measures. This study mainly focuses on the performance of ECs.

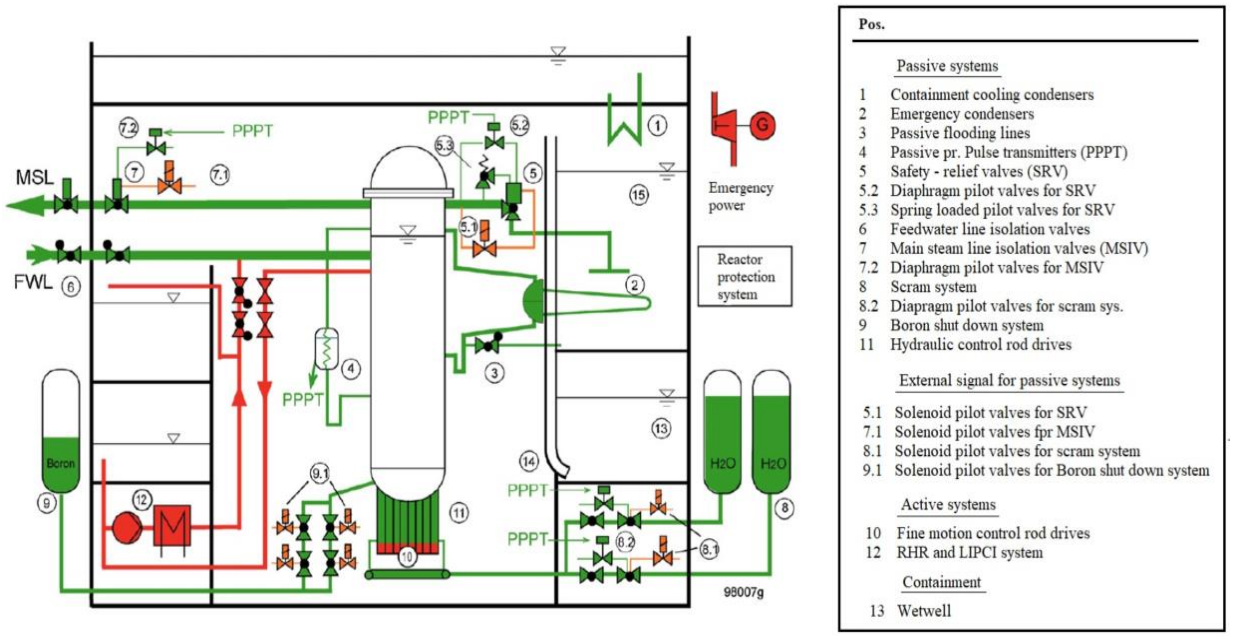

Figure 1-2. The KERENA reactor concept [10]

1.1. Emergency Condensers

The emergency condenser (EC) contributes significantly within the passive safety system of the KERENA reactor. Specifically designed to address emergency scenarios, its primary function is the removal of decay heat generated within the reactor core. The EC is composed of heat exchangers featuring inclined horizontal U-tubes arranged in parallel between two common headers. These headers, situated at the top and bottom, are connected to the steam plenum of the Reactor Pressure Vessel (RPV) below the water level.

During normal system operation, the U-tubes are entirely filled with water, with minimal heat transfer occurring. However, in the event of an accident leading to a reduction in reactor water level, steam infiltrates the U-tubes. Subsequently, the steam within the tubes undergoes

condensation, facilitating the transfer of heat into the secondary side of the condenser, as depicted in Figure 1-3. The resulting condensate then flows back to the RPV through the backflow tubes [11]. This alteration in operational conditions allows the water pool in the secondary side to function effectively as a heat sink [12].

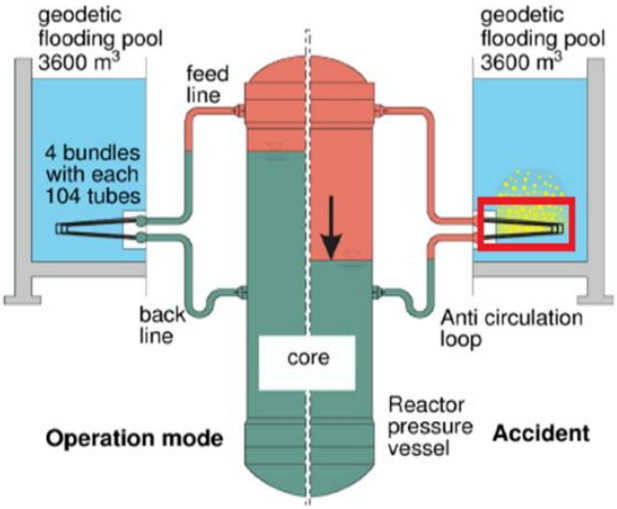

Figure 1-3. The sketch of EC and working principle [9]

During the condensation process of superheated steam within the tubes (primary side), simultaneous phenomena, namely natural convection and nucleate pool boiling, manifest in the cooling water situated in the secondary side (see Figure 1-4).

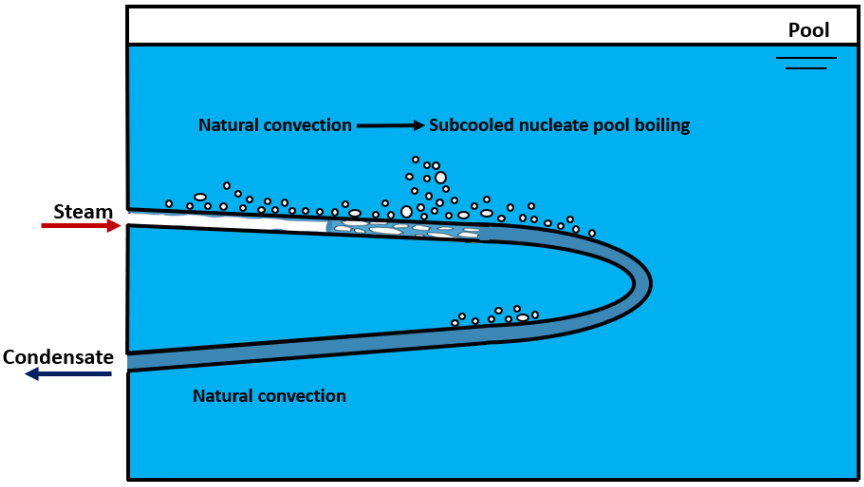

Figure 1-4. Heat transfer behaviour of the fluid in the secondary side

As it can be seen in Figure 1-4, when the superheated steam enters the primary side of the EC, the initiation of heat transfer occurs within the secondary side through natural convection. The steam within the tubes undergoes phase transitions, progressing through distinct flow regimes, including annular flow, slug flow, and ultimately transforming into hot liquid water. The consequential heat flux transferred to the secondary side instigates the formation of bubbles on the outer surface of the tube walls, giving rise to subcooled nucleate pool boiling. As the heat-up process persists, the likelihood of attaining saturation boiling in specific regions of the secondary side progressively escalates. This affects the heat removal capacity of the system.

1.2. Problem statement

On the secondary side, natural convection in a large pool with unstirred fluids, leads to the formation of temperature stratification which increases the difficulty of correct prediction of EC performance. During EC operation, the heat transfer on secondary side starts with single phase natural convection and then shifts to subcooled and nucleate pool boiling as the coolant heats up. The generation of steam in the pool has an impact on the fluid velocity and disrupts the established temperature stratification. Additionally, steam produced in the pool has the potential to escape into the containment atmosphere, thereby increasing the pressure inside a containment. This pronounced temperature stratification results in the attainment of the saturation condition at the uppermost region of a pool at an accelerated pace, in contrast to a condition where the temperature profile is uniformly distributed. Consequently, this triggers an early initiation of the boiling process in a pool due to elevated localized temperatures manifesting in the upper regions [13]. On the other hand, the lower temperature below the stratification layer may improve the heat transfer condition within lower bundles. This results in significant challenges in accurately predicting the system performance during operation. Therefore, the primary objective of this study is to attain an accurate prediction of the temperature profile in the pool and cooling capacity of the heat exchanger during the operation of an EC. This offers essential insights into the factors influencing temperature stratification in the pool, enhancing our understanding of the system's ability to dissipate decay heat during accidents.

Existing literature offers a multitude of empirical or semi-empirical correlations, which have been suggested to estimate the heat transfer coefficient for external flows around an individual tube or a bundle of tubes within various types of heat exchangers, incorporating natural convection and

nucleate pool boiling mechanisms [13-22]. Previous investigations have focused on the examination of heat transfer performance in heat exchangers, considering various factors that influence the heat transfer process and the determination of the heat transfer coefficient. Nonetheless, due to the limited application range of these studies and the intricate nature of the pool boiling mechanism in large size heat exchangers, their ability to accurately predict the heat transfer performance of an EC remains inadequate.

This problem prompts following questions that are intended to be addressed in the course of the thesis:

1. To what extent can the heat transfer models proposed in the literature accurately predict the thermal performance of the system on the secondary side?
2. What is the optimal numerical approach for analyzing the thermal-hydraulic behavior of the secondary side?
3. How a developed empirical heat transfer model can potentially predict the heat transfer performance of passive heat removal systems?
4. Are there alternative, more computationally economical methods for predicting the thermal-hydraulic behavior of the secondary side?

1.3. Thesis objectives and approach

This thesis aims to enhance the predictive and computational modeling capabilities of the thermal-hydraulic dynamics on the secondary side of ECs. The primary objective is to augment the precision and cost-effectiveness of the analytical process, thereby furnishing valuable insights for optimizing system reliability and mitigating the risk of system failures.

Within this framework, a comprehensive review of contemporary heat transfer models suitable for application in this specific context has been conducted. Subsequently, their applicability in predicting the heat transfer coefficient on the secondary side has been evaluated based on experimental data obtained from two distinct test facilities, namely the COSMEA test facility and the NOKO test facility.

In the analysis of thermal hydraulic behavior on the secondary side of the system, computational fluid dynamics (CFD) methods are found to be helpful. Enhanced insights into temperature

stratification and transient behavior of the system can be provided by these methods, which offer valuable means to model fluid dynamics. Significant contributions to the identification and mitigation of temperature stratification can be made by utilizing CFD techniques, thereby increasing the accuracy of performance predictions for the system.

Challenges are encountered when conducting a CFD analysis, which are attributable to the substantial computational costs associated with the scale and intricate nature of ECs. The complexity of the process necessitates the implementation of numerous fluid dynamic models to yield feasible solutions. In response to these challenges, simplifications and assumptions become imperative in CFD calculations to maintain computational feasibility while minimizing deviations from experimental results. Within the scope of this study, a notable challenge pertained to determining the acceptability of process simplifications without inducing significant deviations in the results. The investigation aimed at establishing the extent to which simplifications could be applied without introducing substantial disparities in the outcomes. To achieve this goal, the approach taken in this thesis involves initiating with simpler computational methods and progressively enhancing the model's complexity. In this regard, the CFD calculations commence with a single-phase 2D CFD model and subsequently incorporate various multi-phase models, such as the mixture model and inhomogeneous Eulerian model, along with different phase change sub-models. The computational process concludes with a 3D CFD simulation to give more insights about the 3D behavior of the system.

Despite efforts to enhance comprehension of the heat transfer phenomena occurring in the secondary side of ECs, there persists a requirement for a predictive model capable of assessing the heat transfer performance in a more practical manner, particularly within the context of nuclear applications. It is noteworthy that, in the realm of nuclear applications, 1D codes prevail due to their advantageous computational cost efficiency. Challenges have been encountered in accurately predicting the bundle power, representing the total power transferred from the primary side to the secondary side, in earlier simulations utilizing one-dimensional codes such as ATHLET [23]. The notable disparity in these calculations underscores the necessity to explore alternative approaches aimed at improving the precision of simulations. The focus is on developing methodologies that can reliably forecast the heat removal capacity of the heat exchanger, minimizing deviations from actual performance metrics. Accordingly, the pragmatic development of a heat transfer model

tailored for integration into these 1D codes becomes imperative for more effective and feasible utilization in nuclear applications.

Furthermore, acknowledging the universal integration of artificial intelligence across diverse industries, an endeavor has been undertaken to model the thermal-hydraulic dynamics of the secondary side utilizing Artificial Neural Network (ANN). This initiative is rooted in the premise that a well-suited neural network can construct a model capable of efficiently and cost-effectively predicting system behavior based on experimental data. The availability of pertinent data from test facilities such as NOKO serves as an indicative marker of the feasibility and compatibility of this approach.

1.4. Outline of the thesis

The first chapter in the thesis provides an explanation of the topic, describes the identified problem under investigation and the main goals, and defines the methodological approaches undertaken to achieve the specified objectives.

The second chapter presents the state-of-the-art of the studies related to model or simulate the heat transfer phenomenon in different setups.

Third chapter explains about the test facilities and experimental data used as validation base in this study. COSMEA and NOKO test facilities are the main validation base of this study.

The assessment of the state-of-the-art of heat transfer models that are applicable in the selected test facilities has been carried out in chapter four. The aim is to validate how accurately they can calculate the heat transfer coefficient of the secondary side in each test facility.

Chapter five is specifically devoted to the numerical examinations of the secondary side within the chosen test facilities. In this section, various computational fluid dynamics (CFD) methodologies are applied to depict the thermal-hydraulic dynamics of the secondary side in both test facilities. Subsequently, an assessment of their accuracy is conducted by comparing the computational

results with experimental data. The computational endeavors encompass a progression from single-phase computations to diverse frameworks of multi-phase CFD simulations.

In chapter six, a developed heat transfer model is proposed to accurately calculate the heat transfer coefficient of the secondary side in NOKO test facility.

A developed ANN model is proposed in chapter seven to model the temperature distribution in large volume pools of passive heat removal systems to reach a computationally economical solution in prediction of thermal hydraulic behavior of passive heat exchangers.

In the final chapter of this thesis, the conclusion and summary of this work is presented. It describes the major outcomes of this study, limitations and recommended ideas for future works.

2 Literature review

Extensive research efforts have been dedicated to investigating the thermal hydraulic properties and evaluating the heat dissipation capacity of ECs. This emphasis arises from the necessity to precisely forecast heat transfer capabilities, aiming for potential design improvements. Additionally, it involves gaining an accurate comprehension of system performance to provide correct data for nuclear power plant accident analysis and safety assessments. Numerous studies have been devoted to exploring the thermal hydraulic characteristics and assessing the heat dissipation potential of ECs. This focus stems from the need to accurately predict heat transfer capabilities with the aim of potential design optimization and an accurate understanding of the system performance to provide correct information for NPP accident analysis and safety assessments [14-16]. Notable advancements have been achieved in the analysis and prediction of condensation process of superheated steam in the primary side of ECs [24, 25]. Yu Zhang [10] proposed an advanced correlation to compute the condensation rate and heat transfer coefficient on the primary side of the COSMEA test facility [1], designed specifically to showcase the condensation process within ECs. In this study, the comparison of thermal resistances on both the primary and secondary sides of an EC, as well as the conduction resistance of the tube's surface, has been presented as the motivation for conducting further heat transfer analyses on both sides of such heat exchangers. Figure 2-1, illustrates this comparison under two different operational conditions.

Despite the advancement to predict the heat transfer coefficient of the primary side, there remains room for further progress to attain a comparable level of comprehension of the processes occurring on the secondary side of these heat exchangers. On the secondary side, natural convection in a large pool with unstirred fluids, leads to the formation of temperature stratification which increases the difficulty of correct prediction of EC performance. During EC operation, the heat transfer in secondary side starts with single phase natural convection and then shifts to subcooled and nucleate pool boiling as the coolant heats up. The generation of steam in the pool has an impact on the fluid velocity and disrupts the established temperature stratification. Additionally, steam produced in the pool has the potential to escape into the containment atmosphere, thereby increasing the pressure inside a containment. This pronounced temperature stratification results in the attainment of the saturation condition at the uppermost region of a pool at an accelerated pace, in contrast to

a condition where the temperature profile is uniformly distributed. Consequently, this triggers an early initiation of the boiling process in a pool due to elevated localized temperatures manifesting in the upper regions [13]. This results in significant challenges in accurately predicting the system performance during operation. Therefore, the primary objective of this study is to attain an accurate prediction of the temperature profile in the pool and cooling capacity of the heat exchanger during the operation of an EC. This offers essential insights into the factors influencing temperature stratification in the pool, enhancing our understanding of the system's ability to dissipate decay heat during accidents.

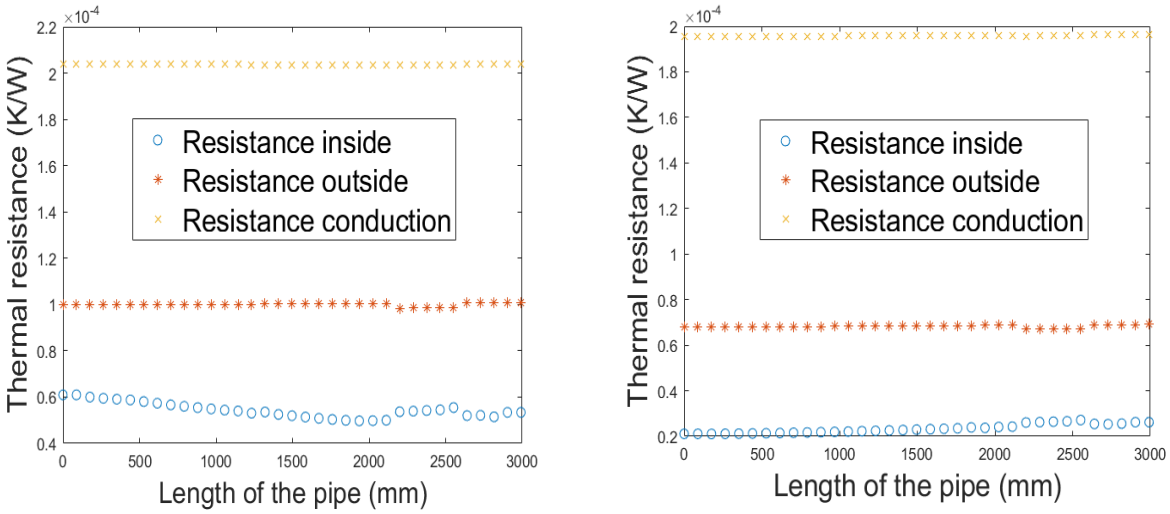

25 bars 65 bars

Figure 2-1. Comparison of thermal resistance of primary side (inside) and secondary side (outside) of COSMEA test facility as well as tube's surface thermal resitance in two different operating conditions [10]

Existing literature offers a multitude of empirical or semi-empirical correlations, which have been suggested to estimate the heat transfer coefficient for external flows around an individual tube or a bundle of tubes within various types of heat exchangers, incorporating natural convection and nucleate pool boiling mechanisms [13-22].

In 1974, Churchill [26] introduced a model for the computation of single-phase free convection on a horizontally oriented cylinder subject to a uniform heat flux. The formulation of this model was constrained within the bounds of laminar boundary layer theory. Later, Churchill and Chu [27]

extended the applicability of this model to a broader range of scenarios, specifically encompassing horizontal tubes and cases where the Rayleigh number (Ra) is less than 10^13. However, even during the validation process, substantial disparities were noted in certain experimental instances.

There have been also other models developed as McAdams [28], Eckert-Jackson [29]and Morgan [30] to calculate Nu number of horizontal tube in specific ranges and their own scope of application. Among them McAdam's model was more commonly used in other works specifically in Men et. al [31] works to calculate Nu number for a C-shaped tube submerged in a water pool.

Lu et al.[32] , Dittus-Boelter [33] and Kuehn-Goldstein [34] are more advanced models for the calculation of the Nusselt number (Nu) in natural circulation, incorporating the influence of forced convection during the heating process. In their formulations, these researchers employed Reynolds number (Re) to account for the augmented fluid velocity induced by the heating stimulus.

Despite all the research related to the single-phase natural convention, it is evident that nucleate pool boiling stands as the predominant and pivotal heat transfer mechanism within the secondary side of passive heat removal systems. In the event of accidents or abnormal conditions within nuclear power plants, the initiation of the heating process imparts a substantial heat flux to the secondary side, (also referred to as the heat sink), invariably resulting in subcooled or saturated pool boiling. The intricacies of this heat transfer process, characterized by its multi-phase nature, pose significant challenges in terms of modeling and investigation. This complexity is further compounded by the multitude of factors such as the geometry of the facility, operating pressure and saturation temperature as well as thermodynamic properties of the coolant influencing the behavior and performance of nucleate pool boiling.

The inherent difficulty in capturing the dynamics of this heat transfer mechanism stems from the interplay of these parameters, making it a formidable task to establish comprehensive models. In the literature, numerous semi-empirical and fully empirical correlations have been proposed to forecast the heat transfer coefficient in the context of nucleate pool boiling for diverse systems. These correlations serve as valuable tools for predicting and understanding the intricate heat transfer dynamics involved in nucleate pool boiling under different conditions, facilitating the design and analysis of passive heat removal systems in nuclear power plants.

In 1963, Mostinski [35] introduced a reduced pressure-based correlation aimed at determining the heat transfer coefficient in nucleate pool boiling. This correlation, however, did not account for the influence of surface effects from the heat source, resulting in an unsatisfactory representation

of the phenomenon. Then in 1980, Stephen and Abdelsalam [13] addressed this limitation by proposing fully-empirical correlations to investigate saturated nucleate pool boiling heat transfer. Their approach took into consideration various factors, including fluid physical properties, tube properties, and operating conditions. The study involved the application of regression analysis to 5000 experimental data points categorized into four substance groups: water, hydrocarbons, cryogenic fluids, and refrigerants. This comprehensive analysis aimed to enhance the understanding of nucleate pool boiling heat transfer across diverse substances and conditions.

Another fully-empirical correlation of saturated nucleate pool boiling is presented by Cooper [14]. This model incorporates the roughness of the boiling surface and establishes relationships with nucleate site size, reduced pressure, and molecular weight. Gorenflo [15] has contributed to this field by developing a novel fully-empirical reduced pressure correlation, accounting for surface roughness and fluid type in a horizontal single tube. This development is grounded in a substantial dataset of experimental observations. In a study by Chun and Kang [16] the impact of various parameters, including surface roughness and tube diameter, on nucleate pool boiling heat transfer was investigated. The authors proposed fully-empirical correlations tailored for both vertical and horizontal tube external heat transfer calculations.

On a different note, Rohsenow [17, 36] introduced a widely utilized semi-empirical correlation for nucleate pool boiling. This correlation is derived from a microscopic examination of the characteristics exhibited by the heated surface and the fluid combination. The model provides a comprehensive understanding of the nucleate pool boiling phenomenon by considering the intricate interplay between surface attributes and fluid properties. Pioro [37] demonstrated that optimizing the power within the Pr number, tailored to the specific surface–fluid pairing, significantly enhances the predictive accuracy of the Rohsenow correlation [17]. However, a drawback of this method lies in its restricted applicability beyond the surface–fluid combinations investigated in the study [38].

The above-mentioned models exhibit certain limitations or necessitate simplifications when applied to the secondary side of a substantial volume of fluids experiencing nucleate pool boiling. However, alternative models, as proposed by Kutateladze et al. [20], Kruzhilin [21], and Labuntsov [22], present enhanced flexibility and applicability across a broader spectrum of

scenarios, particularly demonstrating efficacy in addressing large pool volumes. More details of these specific models and related correlations are mentioned in the appendix section (chapter 9).

As previous investigations have focused on the examination of heat transfer performance in heat exchangers, considering various factors that influence the heat transfer process and the determination of the heat transfer coefficient. Nonetheless, due to the limited application range of these studies and the intricate nature of the pool boiling mechanism in large size heat exchangers, their ability to accurately predict the heat transfer performance of an EC remains inadequate. In addition, to demonstrate the physical behavior of the fluid in this process, some numerical studies have been conducted to explore the phenomena of natural convection and pool boiling in large, confined spaces in ECs [39]. The most relevant study is from Krepper et al. [40] who conducted a numerical analysis of natural circulation and temperature stratification in large pools in a two-dimensional (2D) setting. They focused on the application of an EC, specifically studying large volume pools heated by a bundle of U-shaped tubes submerged in a water tank based on NOKO test facility experiments. The objective of their work was to predict temperature distribution and stratification of the fluid in the secondary side of this test apparatus. Using experimental data, they showed that in NOKO test facility the contribution of the U-bend region of heated tubes compared to total heat flux transferred to the cooling water in the secondary side is negligible [41, 42]. Therefore, 2D CFD modeling seems like a feasible approach. However, the scale of simplifications they used in their calculations, led to considerable discrepancy of calculations from experimental data. For instance, they employed a constant heat flux as boundary condition only in the upper bundle and considered a moment in accident progression when lower part of the bundle is still filled with cold water. In contrast, this study adopts more precise boundary conditions derived from the inherent characteristics of the heat-up process and corroborated by experimental data. Furthermore, because of high computational efforts they needed for their calculations, their work suffers from a lack of comprehensive evaluation based on the experimental data of NOKO facility.

3 Test facilities

This section provides a detailed description of two test facilities considered as the validation base for this work. The discussion encompasses their configuration, instrumentation, and the rationale behind their construction.

3.1. COSMEA test facility

COSMEA, short for COndenSation test rig for flow Morphology and hEAt transfer studies, is a testing apparatus situated within the TOPFLOW facility at HZDR (Helmholtz-Zentrum Dresden-Rossendorf). Its primary objective is to examine steam condensation within a slightly inclined pipe under high pressure, simulating conditions similar to the emergency condenser in the KERENA containment's passive decay heat removal system. The COSMEA setup consists of two concentric annular pipes facilitating countercurrent flow: an inner pipe crafted from stainless steel (primary side) and an outer pipe made of a titanium alloy (secondary side). Saturated water and steam mixture are introduced into the mixer on the primary side, traversing through the inclined condensation pipe set at a 0.76° angle. The outlet connects to a separation tank for measuring condensation rate through the observation of water level gradients. The separation tank, featuring upper and lower sections, enables the separation of steam and water via centrifugal forces. The liquid is then directed back to the blow-off tank of the TOPFLOW facility through a liquid drain line. Cooling water circulates on the secondary side to condense the steam-water mixture (see Figure 3-1). The cooling circuit operates within a pressure range of 2 to 5 bar. The facility is equipped with thermocouples, flow meters, and pressure transducers on both the inner and outer sides of the condensation pipe. A mixture of saturated steam and water is injected into the mixing system in the primary side passing through a flow straightener at the inlet. The flow is fully developed in the beginning of the test section after passing through 460 mm long adiabatic horizontal tube. The condensation part is the main part of the test section where the mixture of steam and water starts to condensate. This section is followed by 560 mm insulated outlet line. The total length of the test rig’s pipe including inlet, condensation and outlet pipe, is 2992 mm.

The test rig ends to a separation vessel which is used to measure the pressure and temperature of the condensate.

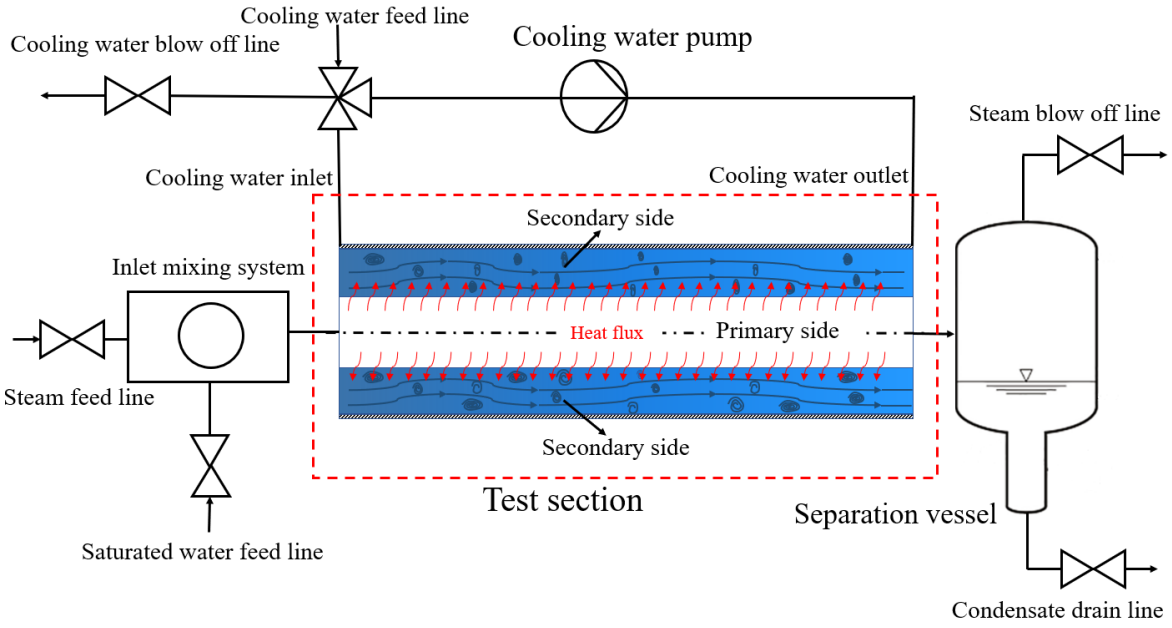

Figure 3-1. COSMEA test facility scheme [43]

The condenser tube, constructed from stainless steel, features a 43.1 mm inner diameter, 2.6 mm wall thickness, a 2992 mm active heat transfer length, and a slight nominal inclination angle of 0.76±0.05°. The cooling tube, made of grade 2 titanium alloy, has a 120 mm inner diameter and 2.0 mm wall thickness. Experimental tests were conducted under high temperature and pressure conditions, reaching up to 554 K and 65 bar. A counter-current flow of cooling water inside the outer tube facilitates forced convection, preventing phase change by means of the high mass flow rate and the designed feed and split system. Temperature measurements involve 24 thermocouple lances with a total of 80 thermocouples, strategically positioned at five axial positions downstream of the inlet for cooling water temperature measurement. This instrumentation provides local temperature data for validating flow simulations in the area.

Furthermore, positioned at a distance of 2183 mm from the inlet on the primary side, a heat flux probe is installed to assess the heat transferred to the secondary side. This probe calculates the temperature distribution at five azimuthal positions (see Figure 3-2) of the condensation test rig and calculates the heat flux for each position using the temperature disparity between the inner and outer sides of the surface of the primary side tube, employing the linearized equation 3-1 .

$$\dot{q} = \lambda(T)\frac{(T_{in} - T_{out})}{d_k} \qquad 3\text{-}1$$

where, $T_{in}$is the inner wall temperature of the primary side, T_{out} is the outer wall temperature of the primary side, d_k is the wall thickness and λ(T) is thermal conductivity of stainless steel versus temperature.

The main experimental parameters for secondary side of COSMEA can be seen in Table 3-1.

Table 3-1. Experimental parameters of COSMEA secondary side

No.	P_{sec} (bar)	$t_{cw\ in}$ (°C)	$\dot{m}_{in}$ (kg/s)	Re	$\dot{q}_{ave}$ (kW/m^2)
5-1	3.57	43.33	13.54	175970	445.01
12-1	3.63	43.09	17.85	231980	649.66
25-1	3.70	42.88	25.00	322700	890.65
45-1	3.73	43.03	32.98	428610	1132.17
65-1	3.65	43.03	36.35	472400	1278.59

The experimental heat transfer coefficient (h_{exp}) can be calculated by equation 3-2.

$$h_{exp} = \frac{\dot{q}}{(T_{out} - T_b)} \qquad 3\text{-}2$$

where, T_b is bulk temperature of the cooling water measured by thermocouple lances [1].

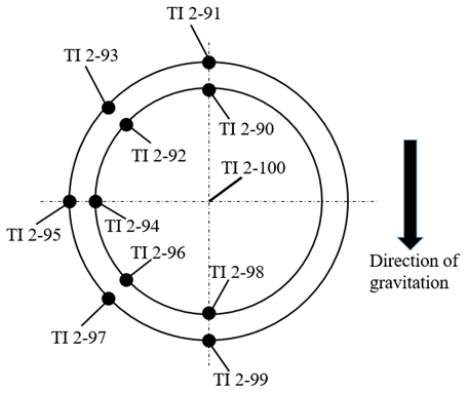

Figure 3-2: Schematic of the location and labels of each thermocouple in heat flux probe [1]

More detailed description of COSMEA facility and the experiments recorded data is published in [1].

3.2. NOKO Test facility

The NOKO test facility, established at Forschungszentrum Jülich (FZJ), with the main goal to evaluate the thermal hydraulic efficiency of passive decay heat removal systems across a range of operating conditions, including diverse pressures (up to 7 MPa) and power levels (4 MW) [23]. In 2005, the facility underwent relocation to Forschungszentrum Rossendorf (FZR), where experiments were conducted to conduct a thorough analysis of two-phase flow on the secondary side. The NOKO-HZDR has been integrated into the TOPFLOW (Transient TwO-Phase FLOW) test facility (see Figure 3-3) , featuring an improved instrumentation concept designed to measure temperature gradients on the secondary side with enhanced precision [23].

Figure 3-3. NOKO component located in TOPFLOW test facility

3.2.1 Configuration and Instrumentation

The NOKO-HZDR module was assembled using identical materials and dimensions as those employed in an emergency condenser within an SWR1000 reactor. The only modification involved reducing the number of tubes within the bundles. The NOKO facility consists of eight U-shaped

tubes oriented horizontally, each measuring around 10,000 mm in length, with an inner diameter of 44.5 mm and a tube wall thickness of 2.9 mm. These tubes are grouped into bundles and immersed in a cooling water medium inside a horizontally cylindrical tank. The tank spans 6 m in length, has an inner diameter of 2 m, and a total volume of 20 m^3 (see Figure 3-4) [23, 44].

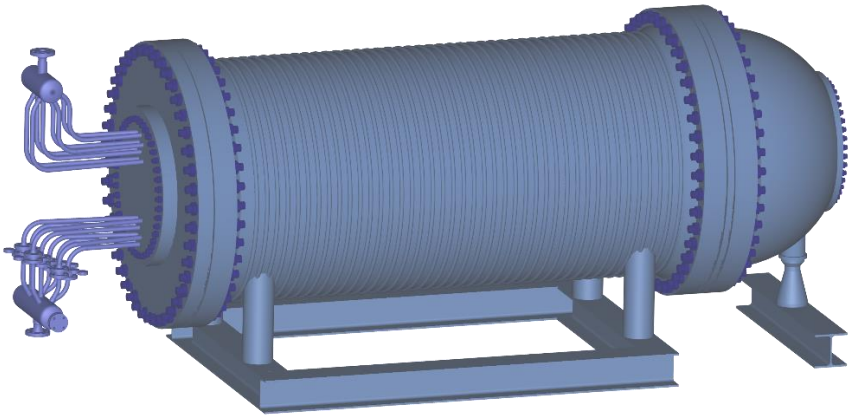

Figure 3-4. schematic of the NOKO-HZDR test rig

The enhanced instrumentation of the FZR's NOKO secondary side includes a configuration of 11 sets of 8 thermocouples with type K, strategically positioned within the tank. These thermocouples are tasked with capturing transient temperature during heat up process. Specifically, at each of the each cross- sectional measuring planes which are labeled A to H along the tubes (see Figure 3-5), eleven thermocouples are distributed in distinct locations as shown in Figure 3-6.

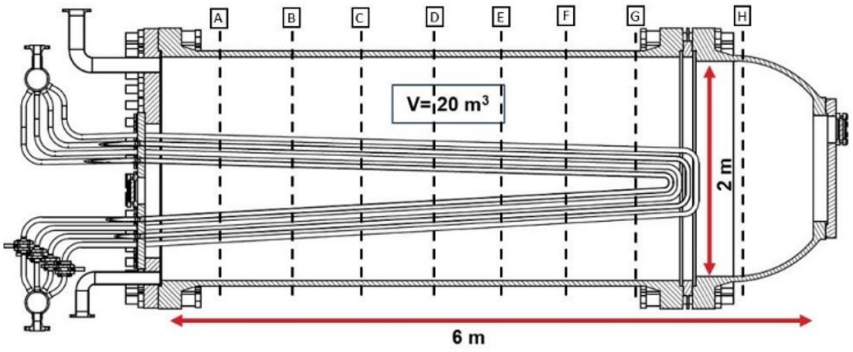

Figure 3-5. The locations of cross-sectional measuring planes A-H

The heat transfer mechanism from the bundle to the cooling water initiates following a reactor accident, wherein steam replaces water in the upper U-tubes of the bundle. Initially, the lower part of the bundle remains filled with cold water. As the process continues, steam within the bundle

undergoes condensation, transforming into liquid water with higher temperature. Consequently, shortly after the commencement of the heating process, the lower bundle is also influenced by the warmed liquid water, intended to circulate back through the lower bundle to the pressure vessel.

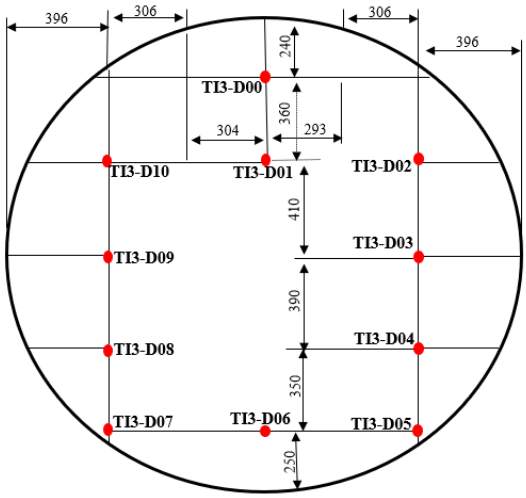

Figure 3-6. Estimated location of type K thermocouples on each measuring planes

Observing the condensation process within the bundles faces challenges due to limitations in the instrumentation of NOKO. Consequently, difficulties arise in monitoring the thermal-hydraulic properties of the fluid within the primary side. Nevertheless, a definitive aspect of this process is the complete condensation of incoming superheated steam through the bundles due to the heat transfer with cooling water of the secondary side. The resulting liquid water, at a higher temperature, returns to the pressure vessel.

3.2.2 Experimental results

The main purpose of this experiments at HZDR was to evaluate the performance of NOKO vessel. For this aim, the tests were carried out at four different operating conditions: 10, 30, 50 and 65 bar. These are the adjusted working pressures inside the bundle of tubes. In all tests the NOKO secondary side was heated from approx. 30 ℃ to boiling by condensing saturated steam in the primary side NOKO bundle. The secondary blow off valves of the vessel was completely open so that the transient heat up process starts from ambient pressure (0.1 MPa). However, after onset of boiling in the secondary side, a slight built up pressure has been observed due the pressure loss

when the gas mixture is blown off. The level of water in the vessel for all experiments has been chosen in a way that all the bundles are completely submerged in the water (approx. 1.8m). The attempt during the experiments was to make the condensation process complete so that the liquid water goes back to the pressure vessel. Table 3-2 shows the range of most important parameters measured during the experiments.

Table 3-2. Measured values of general parameters of NOKO experiments

Experiment No.	Primary side Pressure [MPa]	Secondary side pressure [MPa]	Initial temperature of Secondary side [°C]	Level of water in tank [m]	Power of the HX at steady state [MW]
10 bar	0.994-1.072	0.137-0.156	Approx. 32.5	1.688-1.743	1.35
30 bar	3.024-3.070	0.133-0.182	Approx. 20.0	1.688-1.792	2.545
50 bar	5.076-5.090	0.133-0.186	Approx. 22.0	1.673-1.717	3.117
65 bar	6.476-6.820	0.133-0.155	Approx. 25.5	1.653-1.719	4.011

The intense heat transfer from the primary side to the secondary side while the heat exchanger is in operation results in a non-uniform temperature distribution within the tank. The experiments conducted at the NOKO facility have revealed significant thermal stratification and abrupt temperature changes at various levels of the cooling water in the tank. Figure 3-7, illustrates the recorded temperatures from 11 thermocouples positioned on measuring plane D, which is situated approximately in the middle of the bundle's length (see Figure 3-5) during the experiment No. 65bar under conditions shown in Table 3-2.

Thermocouples TI3-D05, TI3-D06, and TI3-D07 shown in Figure 3-7, are sensors placed in the lower section of the tank, as illustrated in Figure 3-6. Analysis of the corresponding diagrams reveals a significant temperature increase (Big jumps) occurring after 1500 seconds, with no noteworthy temperature changes observed prior to this point. Before this temperature surge, a region with low thermal activity forms in the lower part of the tank during the initial heat-up phase. This has been deduced from the consistent recorded temperatures from these thermocouples

located in the lower regions of the tank. Temperature increases substantially in this area when the upper part of the tank approaches saturation conditions.

In the upper part of the tank, thermocouples TI3-D00, TI3-D01, TI3-D02, and TI3-D10 (refer to Figure 3-6) exhibit a rapid temperature rise a few seconds into the process. However, after the big sudden temperature increase in the lower part of the tank, another noticeable jump in temperature is recorded (small jump shown in Figure 3-7) indicating a faster increase compared to the previous temperature pattern in these locations. Accordingly, Thermocouples TI3-D08, TI3-D09, TI3-D03, and TI3-D04, situated in the middle of the tank, also show a considerable temperature increase. It is also evident that the small temperature jumps occur simultaneously in all locations, indicating the establishment of saturation conditions in the tank. One reason for such behavior in recorded temperatures is that during the heat up process, steam generation in secondary side effects the velocity of the fluid in the tank. Therefore, the heat transfer rate in some areas changes drastically as well as the recorded temperatures.

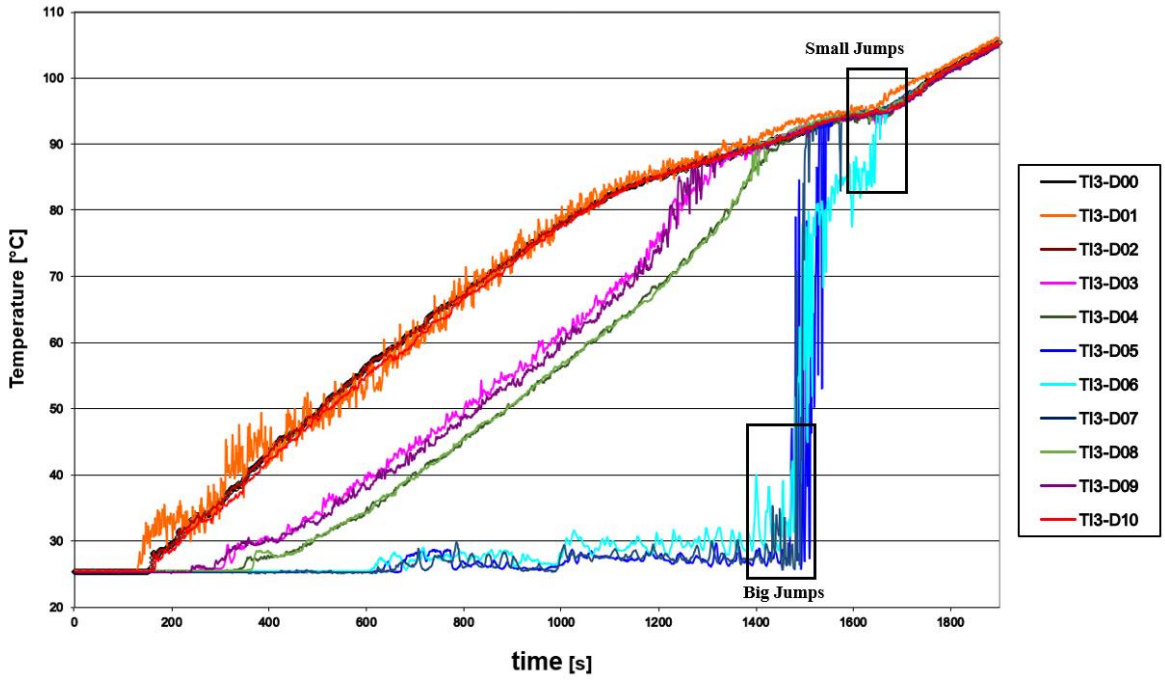

Figure 3-7. Experimental transient temperature distribution of the secondary side on plane D under conditions of experiment No. 65bar [41]

The same behavior has been observed in the recorded data of thermocouples located on other measuring planes from A to H. There is only a slight difference related to the planes closer to the

U-bend region. However, because of the insignificance of heat transfer from primary side to the secondary side in this location, it is feasible to assume that the temperature distribution along the length of the tubes bundle is nearly uniform [41]. In order to assess this claim, three distinct points of interest were selected on every measurement plane, designated as TI3-02, TI3-03, and TI3-05 (respectively related to the top, middle and bottom areas of the tank). A comparative analysis of the recorded data obtained from these designated locations was subsequently conducted across all eight measurement planes. Figure 3-8 shows the results of this demonstration. Figure 3-8 (a), shows that the temperature in the upper region of the tank exhibits a consistent increase following an identical pattern across all longitudinal locations. A comparable behavior is evident in Figure 3-8 (b), for almost all the measuring planes. Only a marginal deviation of about 4 to 5 degrees is noted only for measuring plane G, which is situated within the confined area at the edges of the U-bend region. The close proximity of two bundles in this region results in a heightened temperature record for the middle-level location. A slightly larger deviation is observed in Figure 3-8 (c), pertaining to the bottom of the tank on measuring plane H. Based on this diagram it is evident that in the bottom of the tank, the temperature increase aligns with the same pattern observed in most longitudinal locations, with temperature jumps occurring simultaneously. However, the recorded data for measuring plane H reveals a distinctive behavior. The recorded data related to this location, shows a gradual temperature increase starting significantly earlier that locations related to the other measuring planes. However, a minor sudden temperature increase happens to reach to the same temperature as other locations, while other points experience more substantial jumps to attain the same thermal level. Therefore, after about 1500 seconds, the temperature continues to increase with the exact same pattern for all measuring planes. This varied pattern of temperature increase in the beginning of the heat up process until t=1500 s, is attributed to the location of measuring plane H, positioned outside the zone occupied by the tubes. Consequently, the mixing process of cold and warm liquids occurs more rapidly in this region, leading to greater heat transfer in the lower regions compared to areas within the tube zone. This phenomenon arises due to the positioning of the measurement plane H outside the U-shaped

bundles, where mixing the fluid is less restricted. Nevertheless, the behavior of measuring plane H aligns with other measuring points after 1500 seconds into the process.

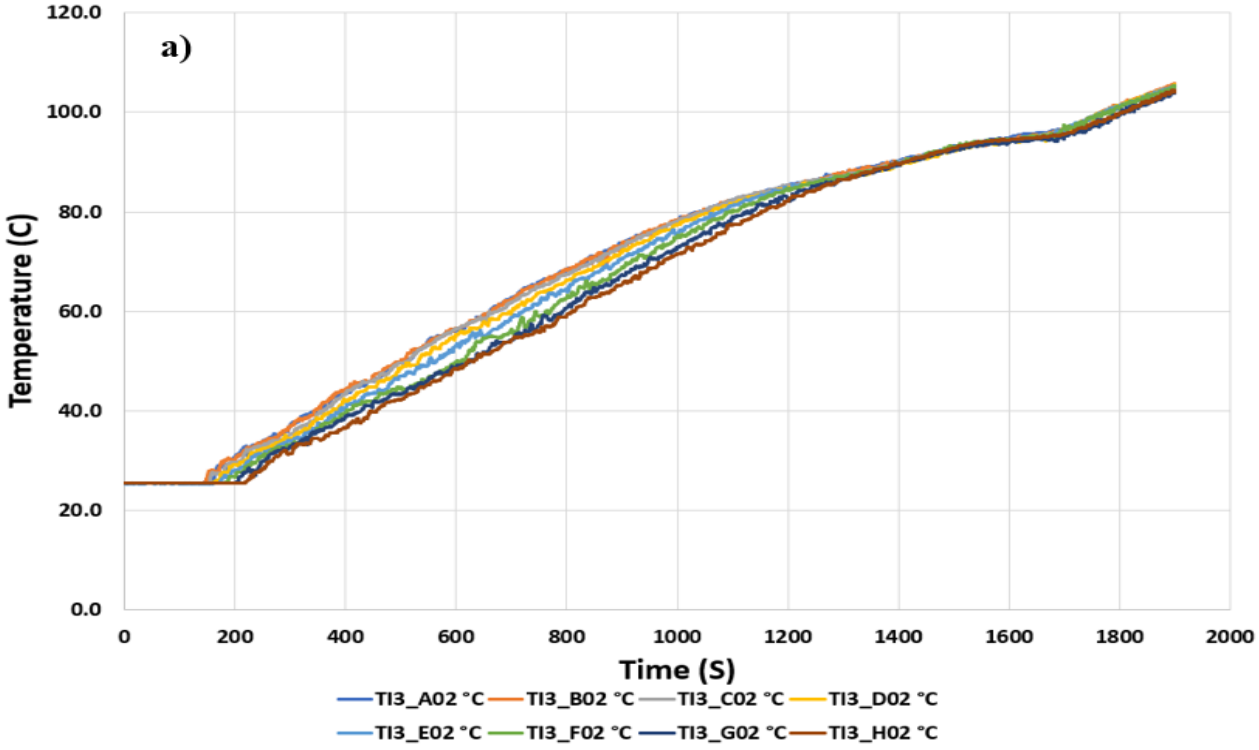

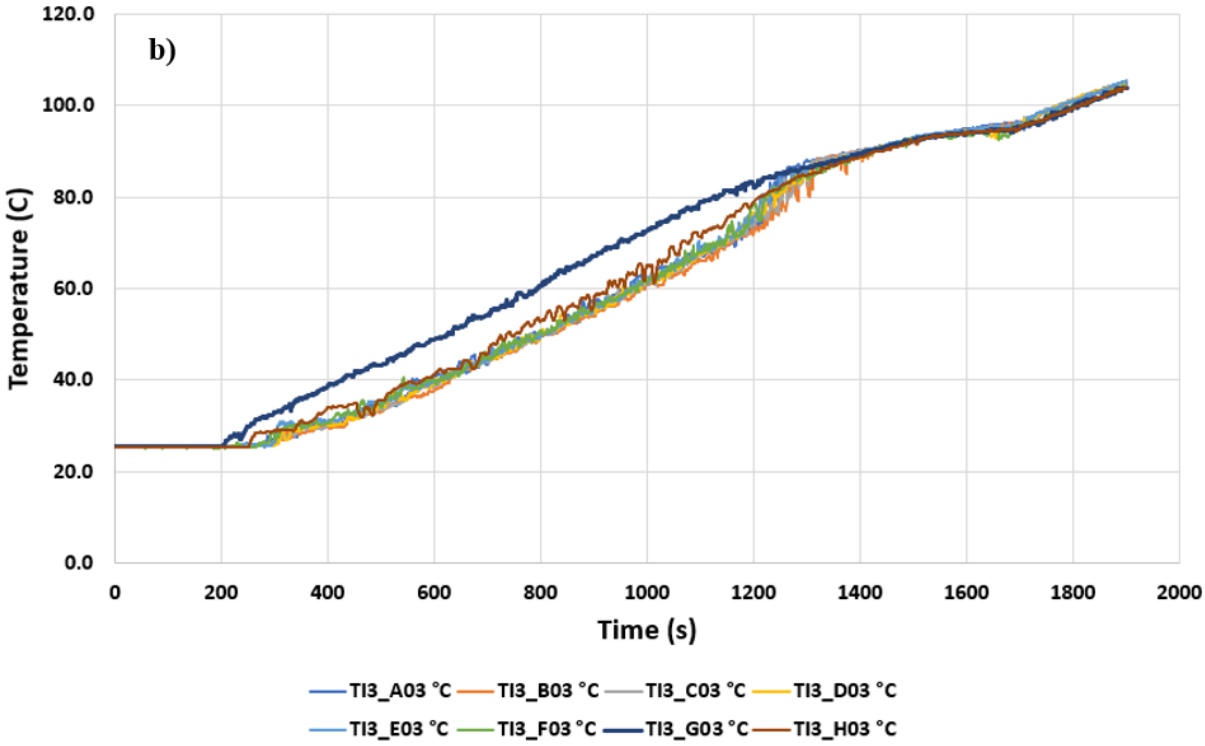

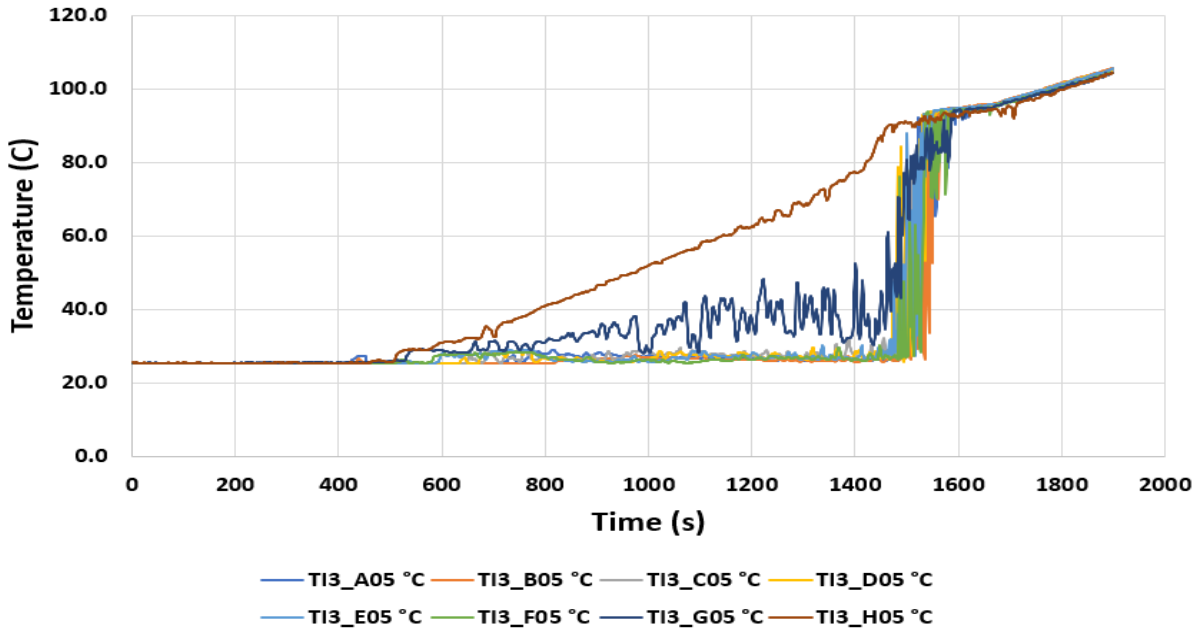

Figure 3-8. Temperature increase of thermocouples NO. TI3-02 (a), No. TI3-03 (b) and TI3-05 (c) for measuring planes A-H

A similar thermal-hydraulic behavior has been systematically identified through a series of NOKO experiments conducted under diverse operational conditions and varied power levels, as detailed in Table 3-2. The uniformity in the thermal-hydraulic response provides valuable insights into the system's behavior and enhances the comprehensiveness of the findings, establishing a foundation for further analyses and applications in diverse contexts within the specified operational range.

4 Heat Transfer Assessment

Within this chapter, an evaluation is undertaken on the state-of-the-art heat transfer models relevant to the secondary side of each test facility expounded upon in the preceding section. This examination is conducted to assess the precision of these models in predicting the heat transfer coefficient on the secondary side across various applications.

4.1. Heat Transfer Assessment for COSMEA secondary side

In this section, focus is placed on the secondary side of the COSMEA test facility. Despite differences in the heat-up process governing the secondary side compared to that of an emergency condenser, commencing the investigation with an exploration of the processes occurring in this facility is deemed necessary. This preliminary examination is required to ensure that our findings are comprehensive and that a solid foundation is established for further investigations in more complex test facilities.

The dominant heat transfer mechanism in this specific part of the facility is recognized as single-phase forced convection, as detailed in the COSMEA test facility description in chapter 3.1. . This crucial insight guided the systematic selection of heat transfer models, carefully chosen to match the specific features in single-phase forced convection and suitably adapted to the concentric annular geometry defining the structure of the COSMEA secondary side. The detailed heat transfer models with related correlations have been described in Chapter 2.

In the assessment of the COSMEA experiment heat transfer models, emphasis has been placed on the Reynolds number of the secondary side as a key parameter for characterizing internal flow. The heat transfer coefficient of the secondary side has been calculated for three different primary side working pressures (Experiments No. 25-1, 45-1 and 65-1) using state-of-the-art heat transfer models for concentric annular ducts in MATLAB. Subsequently, a comparison between the calculated results and experimental data has been undertaken, and the findings are presented in Figure 4-1. The vertical axis of the figures shows a comparison factor ($h_{cal.}/h_{exp}$) to investigate the deviations of the calculated results with experimental data. h_{cal} is calculated by using the heat

transfer models from Table 0-3 and h_{exp} is obtained by Eq. 3-2. The horizontal axis shows the Reynolds number increase in each operating condition.

As it can be seen in Figure 4-1, there is a substantial disparity between the calculated outcomes and the experimental data. While Foust and Christian's correlation, as well as Gnielinski's correlation, align well with the experimental data at certain points, significant discrepancies persist under varying conditions.

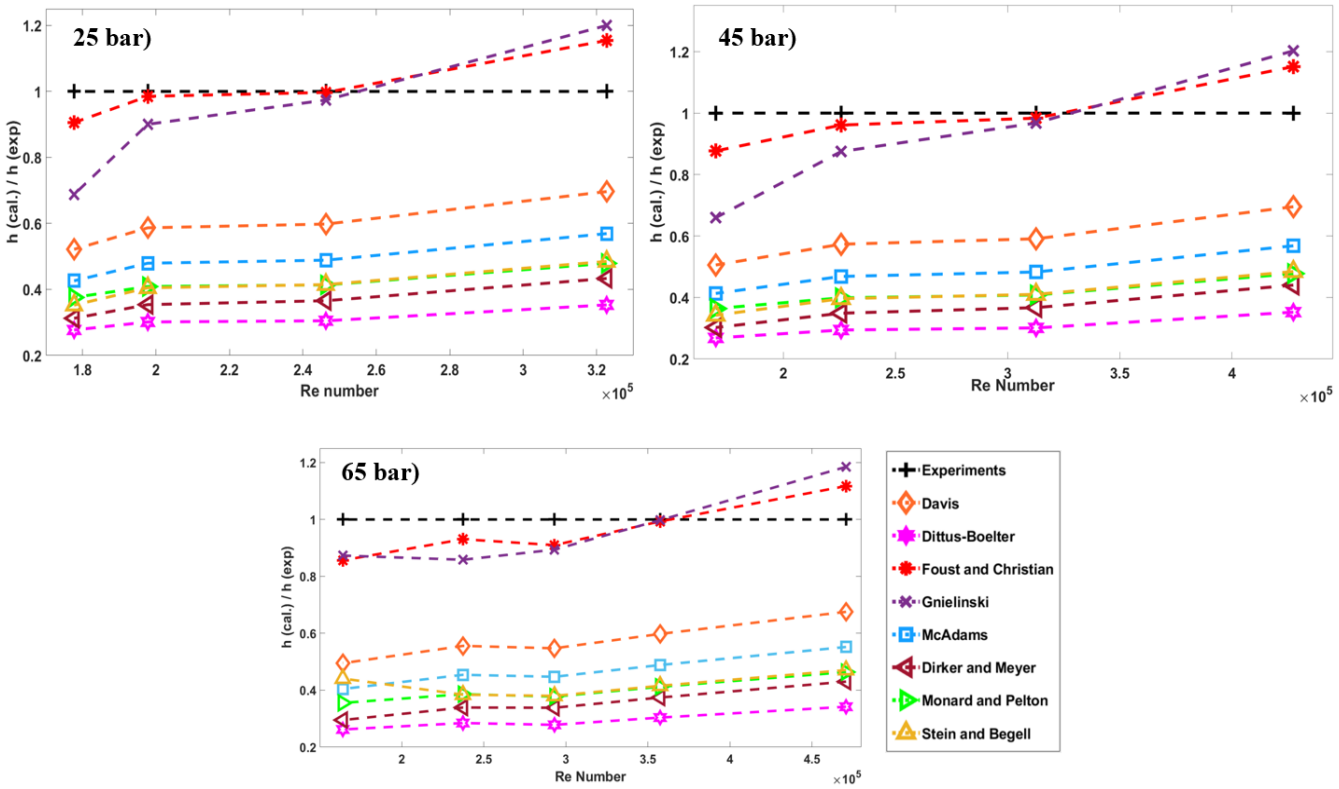

Figure 4-1. Model evaluation for Experiments No. 25-1, 45-1 and 65-1

It is worth noting that the discrepancies in underprediction and overprediction of Foust and Christian's correlation, as well as Gnielinski's correlation, significantly escalate with variations in the Reynolds number. The friction factor of turbulent flow (f_{ann}), employed in Gnielinski's correlation, is dependent to the Reynolds number, rendering the calculated heat transfer coefficient more responsive to Reynolds number fluctuations (see Table I). As previously mentioned, aside from the Reynolds number, Prandtl number (Pr) and diameter ratio (a) are two additional

influential parameters in heat transfer models. The impact of these parameters on the calculated heat transfer coefficient varies across models and different Reynolds numbers. Changes in the thermodynamic characteristics of the flow on the secondary side induce alterations in Reynolds number and Prandtl number. Consequently, under different operating pressures and temperatures, these parameters significantly influence the calculated heat transfer coefficients.

In Figure 4-1 at 25 bar, when the Reynolds number equals 250,000, the deviation of results from Foust and Christian's correlation and Gnielinski's correlation is minimal. Conversely, in Figure 4-1 at 65 bar, the minimum deviation occurs at a Reynolds number of 350,000. Deviation increases at both lower and higher Reynolds numbers in each figure. Moreover, the calculated results from other correlations exhibit larger discrepancies with experimental data, indicating a complete failure to accurately predict the actual heat transfer coefficient on the secondary side of the COSMEA facility. These deviations stem from the empirical development of the proposed correlations using diverse test setups in varying working conditions. Consequently, when applied to a heat exchanger with different geometry and operating conditions, the results prove unsatisfactory. Additionally, these correlations have limitations as they overlook other influential factors such as buoyancy, eddy diffusivity, and turbulence models.

These comparisons underscore that turbulent forced convection flow correlations for concentric annulus ducts are inadequate for predicting the heat transfer coefficient on the secondary side of the COSMEA facility. While some methods provide relatively accurate heat transfer coefficients, deviations vary across different operating conditions of COSMEA experiments. This underscores the importance of CFD calculations to provide deeper insights into the thermal-hydraulic behavior of the COSMEA secondary side and to enhance the accuracy of secondary side heat transfer coefficient calculations. Despite considerable differences between the features of the process in the COSMEA secondary side and those in real-scale ECs, gaining a better understanding of the

heat transfer process in these facilities can lay the groundwork for comprehending fluid dynamic behavior on the exterior of condensation tubes in ECs and the cooling process within ECs.

4.2. Heat transfer model assessment for NOKO secondary side

On the secondary side of the NOKO test facility, two predominant heat transfer mechanisms are observed: initially, single-phase natural convection, followed by subcooled nucleate pool boiling mechanisms. Notably, once the primary side reaches a steady-state condition, the outer wall temperature surpasses the saturation temperature, indicating the commencement of subcooled pool boiling. It should be noted that "steady state condition" here refers to the point when the inlet and outlet temperatures on the primary side have stabilized to relatively constant values. Consequently, heat transfer models designed for nucleate pool boiling are employed to compute the heat transfer coefficient on the secondary side. Among the models available in the literature, Kutateladze [20], Rohsenow [17], Kruzhilin [21] and Labuntsov [22] are identified as the most applicable for the secondary side of NOKO under steady-state conditions. The selection of these models is based on their suitability for the application range and their development specifically for nucleate pool boiling in large volumes of coolant surrounding cylindrical or flat heat sources. These chosen models serve as computational tools to ascertain the heat transfer coefficient during the steady-state condition of the process. Subsequently, the total heat flux from the primary side to the secondary side is quantified based on experimental data. Consequently, the experimental heat transfer coefficient for the adjacent fluid in contact with the tube surface on the secondary side is derived. To achieve this objective, first, the total heat flux transferred from the primary side to the secondary side, along with the thermal conductivity and thickness of the tube surface, and the inner wall temperature are extracted from experiments. Then, the outer wall temperature is computed using the conduction correlation. (Equation 4-1).

$$Q = -kA\frac{dT}{dx} \qquad 4\text{-}1$$

Subsequently, Equation 4-2 is employed to calculate the heat transfer coefficient on the secondary side, having the outer wall temperature, saturation temperature, the total area of heat transfer and total heat flux transferred to the secondary side.

$$\dot{Q}_{total} = h_{exp}.A.(T_{out-}T_{sat}) \quad 4\text{-}2$$

T_{out} is calculated using equation 4-1. It should be mentioned that the calculated h_{exp} is the average heat transfer coefficient (HTC) of the secondary side considering the outer wall temperature distribution of the heated tubes is uniform.

The comparison of the calculated heat transfer coefficient (HTC) from nucleate pool boiling model and experimental data are represented in Table 4-1. In this table, it can be observed that these models inadequately predict the heat transfer coefficient on the secondary side with significant deviations.

Table 4-1. Accuracy of selected heat transfer models against experimental data and CFD calculations

Author	**Experimental results** $\boldsymbol{HTC_{exp}}$**, W/m²K**	**Calculation result** $\boldsymbol{HTC_{calc}}$**, W/m²K**	**Error, %**
Kutateladze [20]	3.858×10^3	$2.006 \cdot 10^4$	419.95
Rohsenow [17]		$4.79 \cdot 10^4$	1141.57
Kruzhilin [21]		$2.7 \cdot 10^4$	599.84
Labuntsov [22]		5.905×10^3	53.06

$$Error = \left|\frac{\alpha_{calc} - \alpha_{exp}}{\alpha_{exp}}\right| \cdot 100\% \quad (4\text{-}3)$$

The large differences in classical heat transfer models' calculations of the outer fluid's heat transfer coefficient arise from diverse experimental and geometrical conditions used in their development [38, 45]. Examination of the physical model's geometry utilized in this investigation reveals significant deviations from the classical benchmarks of pool boiling. This suggests that variations in heat transfer coefficient calculations can be ascribed to the specific experimental conditions and distinct geometric features of the model under study, particularly in the realm of pool boiling. Consequently, it emphasizes the necessity of taking these unique factors into account when interpreting and comparing heat transfer predictions across various studies and models. The U-

shaped configuration of heated tubes, along with a slight inclination, influences the heat transfer efficiency of the heat exchanger differently compared to the conventional benchmarks of pool boiling geometry.

4.3. Conclusion

The assessment of heat transfer models, as discussed in existing literature and implemented for determining the heat transfer coefficient on the secondary side in various test facilities, exposes limitations in their ability to reliably forecast the thermal performance of these systems in heat removal applications. The significant discrepancy observed between the outcomes predicted by traditional heat transfer models and the empirical data obtained from the COSMEA and NOKO test facilities emphasizes the necessity to explore alternative methodologies for accurately modeling the phenomena on the secondary side. This exploration is crucial for achieving a more thorough comprehension of the underlying processes and, as a result, devising effective solutions to improve the overall performance of the system.

5 Numerical Modeling

Within this chapter, computational fluid dynamics (CFD) is applied to model the thermal-hydraulic behavior of the secondary side in both COSMEA and NOKO test facilities. The primary objective of this chapter is to offer comprehensive insights into the heat transfer processes occurring on the secondary side. The COSMEA test facility serves as a valuable platform for gaining deeper insights into the dynamics of forced convection in the cooling process of superheated steam in the primary side, leading to the transformation into liquid water via condensation. This elucidation is crucial for advancing studies pertaining to the primary side of operations. Specifically, it sheds light on the evolution of high-temperature profiles in the vicinity of heated tubes and the resulting changes in bulk temperature induced by forced convection mechanisms.

Conversely, the numerical modeling of the NOKO secondary side offers enhanced understanding of the thermal-hydraulic characteristics exhibited by fluids within the secondary side of an EC. The geometric resemblance and shared heat transfer mechanisms between the NOKO secondary side and real ECs underscore the relevance of this modeling endeavor. Moreover, the limitations in visually observing natural fluid circulation within the NOKO test facility, attributed to the intricacies of the heat transfer processes, serve as an additional motivation for this investigation.

This analytical pursuit aims to achieve several objectives, including the simulation of temperature stratification, analysis of fluid velocity distribution throughout the process, and precise prediction of transient coolant temperatures. This leads to address the most effective parameters on the performance of an EC, leading to find ways to improve its operation. The main goal is to attain a high degree of predictive accuracy while ensuring computational efficiency, thereby optimizing cost-effectiveness in the solution approach.

5.1. CFD simulation of COSMEA secondary side

Utilizing ANSYS CFX, a 3D steady-state computational fluid dynamics (CFD) simulation has been conducted to model the turbulent single-phase flow within the secondary side of the COSMEA facility. The primary objective of this simulation is to undertake a thermal analysis of

the secondary side under various operating conditions and generate precise prediction of the heat transfer coefficient within this segment.

The first setup for the CFX simulation involves the utilization of an annular duct featuring geometric characteristics as the COSMEA secondary side. Employing ICEM ANSYS software the geometry has been meshed, resulting in a total of 1,148,400 nodes. The configuration of the test setup can be observed in Figure 5 1. Within the secondary side of the heat exchanger, the flow experiences a transmitted heat flux from the primary side along the tube's length. To reduce the computational demands of simulating the condensation process on the primary side, the high-resolution inner wall temperature data obtained from experiments conducted at the COSMEA facility is applied as a boundary condition. This boundary condition encompasses temperature variations along the length of the tube as well as angular positions around the tube. Additionally, the characteristics of the inlet and outlet flow on the secondary side have been incorporated as part of the boundary conditions for the simulation.

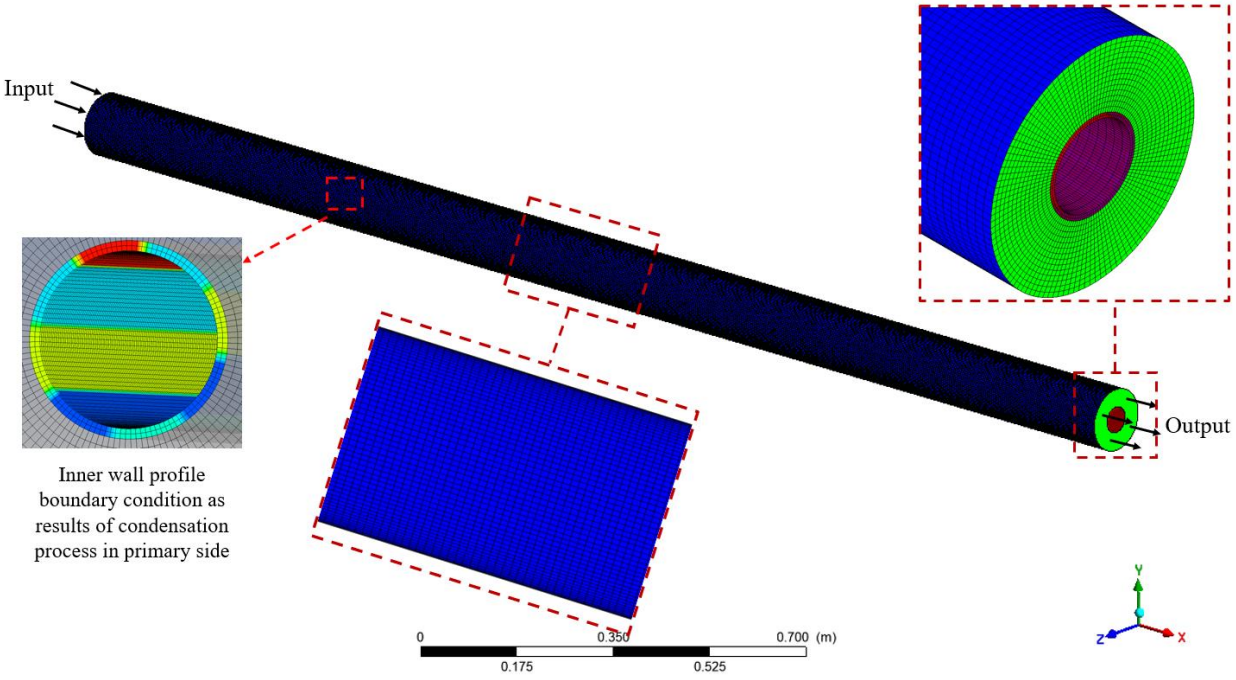

Figure 5-1. CFD setup and mesh structure of COSMEA secondary side

In simulating turbulent flow within the concentric annular duct, the shear stress transport (SST) model has been employed. This model, distinct from standard k-ε and k-ω models, combines

features of both, addressing their limitations and excelling in areas of good performance. The SST model mitigates the overprediction of eddy viscosity, enhancing predictions of onset and degree of separation from smooth surfaces [46]. Furthermore, the simulation considers conjugate heat transfer between solid and fluid domains, utilizing the conservative interface heat transfer flux option in ANSYS CFX. The current set of simulations employs a high-resolution discretization scheme.

The ANSYS CFX CFD simulation was conducted for all five distinct sets of experiments, shown in Table 3-1. Based on experimental results and the calculations done by Zhang et al. [1, 24], when the primary side inlet is pure steam, the variations in inner wall temperature along the length of the tube on the primary side are negligible. Consequently, the local heat transfer coefficient on the secondary side is considered equivalent to the average heat transfer coefficient.

To assess the reliability of the CFD simulation, an analysis of mesh independency was undertaken. Four distinct mesh sizes (400,000, 680,000, 920,000, and 1,100,000 nodes) were created using ICEM ANSYS software and subsequently applied to the CFX codes. Figure 5-2 illustrates the results for one specific experimental condition (No. 25-1), with the average interface temperature between solid and fluid domains serving as the testing parameter.

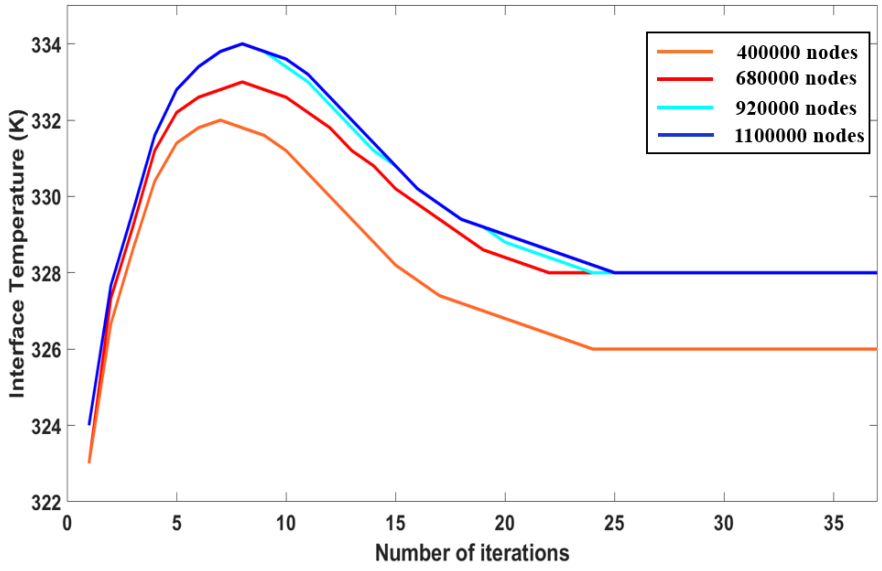

Figure 5-2. Results of mesh sensitivity assessment

Furthermore, the temperature distribution of the fluid within the secondary side was extracted from CFD calculations for a specific case (experiment No. 25-1), showcasing variations along the length

of the tube and across the cross-sectional area in Figure 5-3 and Figure 5-4. These figures reveal a more pronounced temperature gradient occurring near the outer surface of the primary side. However, in the bulk region, farther from the heated wall, the temperature exhibits consistence temperature. It means that the boundary layer experiences a temperature gradient, with higher temperatures closer to the surface due to heat transfer. However, as the water moves away from the surface, the heat disperses, resulting in a less pronounced temperature gradient in the bulk flow. This phenomenon highlights the significance of boundary layers in heat transfer processes.

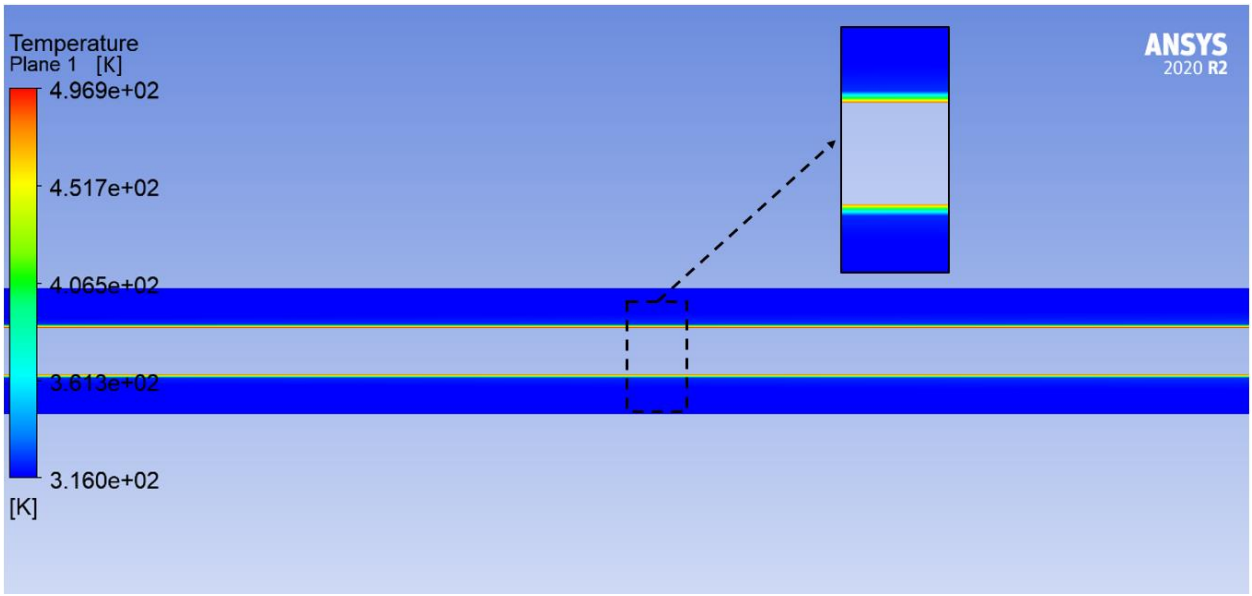

Figure 5-3. Temperature distribution of cooling water along the lenght of the COSMEA secondary side

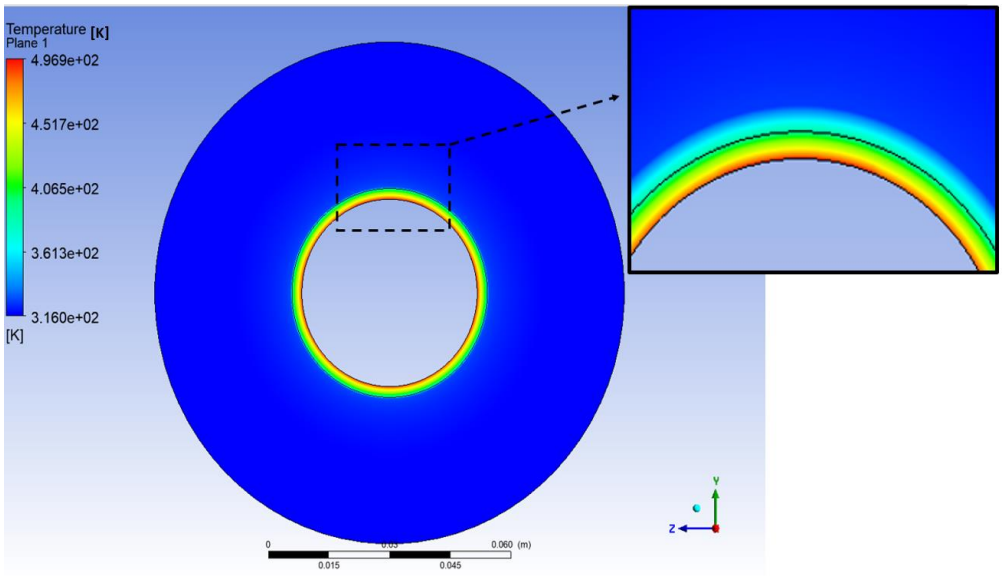

Figure 5-4. Temperature gradients on the cross sectional area of the COSMEA secondary side

In chosen experiments outlined in Table 3-1, the average heat transfer coefficient was computed using CFX code and subsequently compared with outcomes from heat transfer models in existing literature. This comparative analysis is depicted in Figure 5-5. Notably, the CFD simulations effectively align with the experimental data, and has a minimum deviation compared to other heat transfer models proposed in the literature. The figure illustrates the disparities between heat transfer models proposed by various studies and their alignment with experimental data,

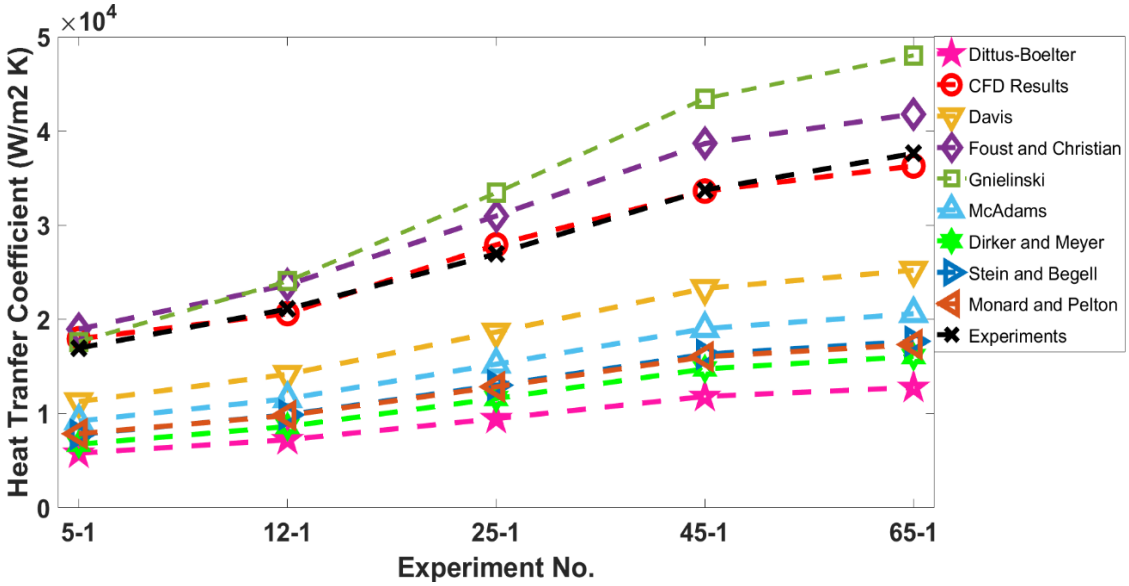

Figure 5-5. Heat transfer coefficient calculated by CFD, experimental data and empirical heat transfer models

highlighting the enhanced accuracy of CFD results in predicting the heat transfer coefficient of the COSMEA secondary side.

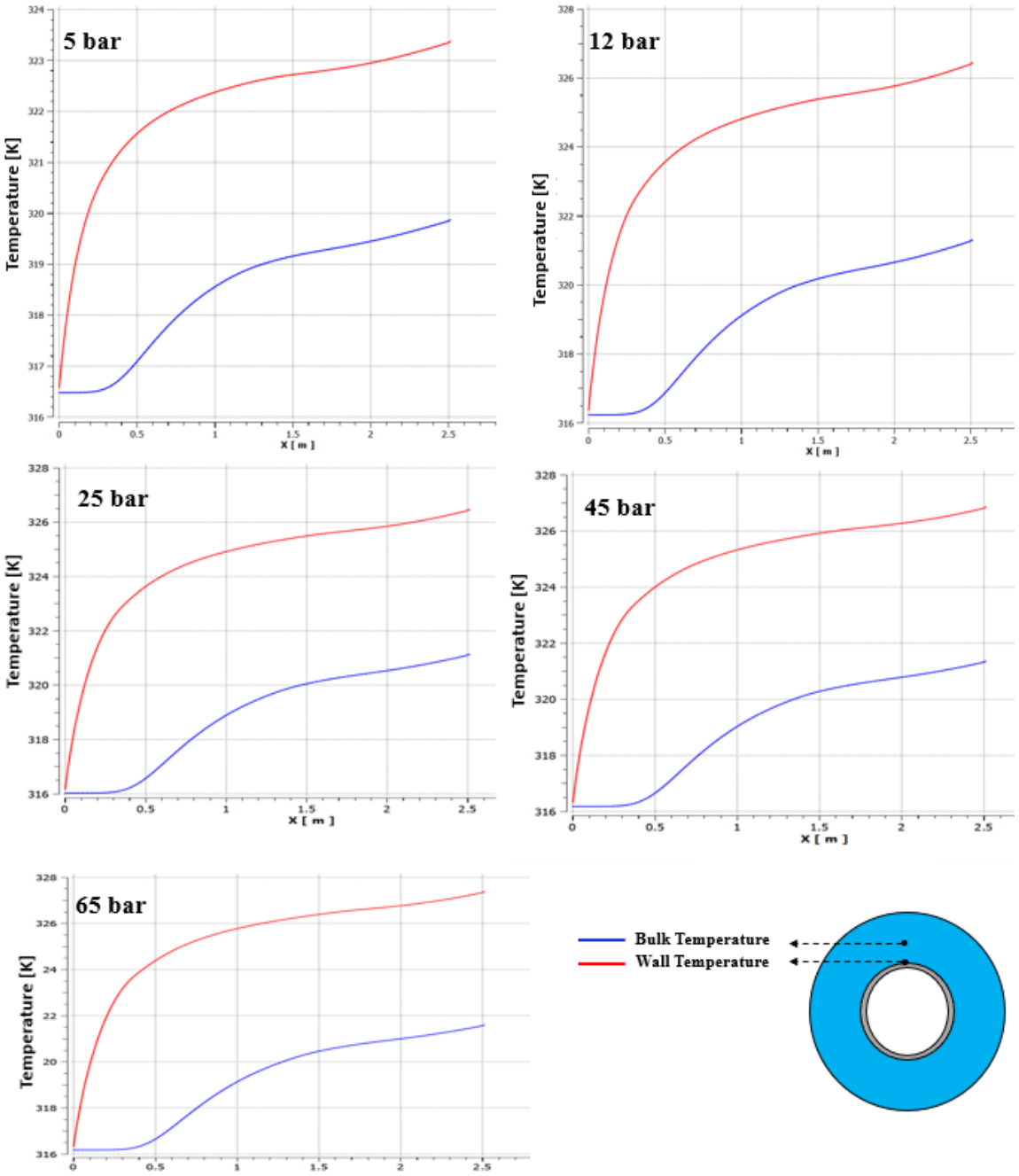

Figure 5-6. Temperature profile along the length of horizontal tube

Finally, to illustrate the progression of both the bulk temperature of the cooling water and the wall temperature at the interface between the solid and fluid domains, temperature diagrams for these

two parameters along the length of the tube were generated for all five distinct operating conditions. These diagrams, depicting the evolution of temperatures, are presented in Figure 5-6.

The variation in wall temperature along the tube's length correlates with boundary conditions derived from COSMEA experimental data. During different phases of condensation in the primary side, there is a progressive increase in heat flux, leading to a rise in wall temperature. The disparity between wall and bulk temperatures indicates the presence of a boundary layer. The temperature gets noticeably hotter near the wall, showing that heat moves well from the surface to the nearby fluid within the boundary layer. This reminds us how important it is to understand how fluids move, especially when dealing with heat. The difference in temperature between the wall and the rest of the fluid tells us there's a lot going on with how the fluid flows, how heat spreads, and what happens right next to the surface.

5.2. Single phase CFD Simulation for NOKO test facility

The investigation of the secondary side of the NOKO-EC system involved conducting comprehensive single-phase CFD simulations using ANSYS CFX. The primary focus of initiating these simulations was to capture the initial phase of the heat-up process preceding the onset of evaporation. In this early stage, heat transfer was exclusively facilitated through single-phase natural convection. To accurately represent this process, a two-dimensional (2D) model was employed to depict the axial cross-sectional area of the NOKO tank at a specific measuring plane denoted as D, as illustrated in Figure 3-5 and Figure 3-6. As mentioned in chapter 2, the research by Krepper et al. [41] indicated that the horizontal temperature gradient along the length of the bundles was negligible. This feasibility of this assumption has been also demonstrated in section 3.2. Consequently, opting for a 2D CFD simulation was a pragmatic approach to minimize computational expenses.

The simulation mesh, comprising 154,813 elements, was strategically designed to capture the details of the process. At the free surface of the cooling water in the tank, a free-slip boundary condition was imposed. This boundary condition was crucial in replicating real-world conditions and ensuring the fidelity of the simulation. This boundary condition is often considered the best fit for free surface simulations because in large scale tanks or bodies of water, the surface tension of the water and the absence of any solid boundary in immediate contact with the water allow for slip to occur naturally. This means that the velocity of the water at the surface is not necessarily zero,

but rather allows for some degree of tangential movement. In terms of thermal considerations, a constant heat flux of 369 kW/m2 was applied at the upper tube bundle's surface. This heat flux was derived from the total heat transferred from the primary side to the secondary side at steady state condition, divided by the total surface area of the tubes. This approach aimed to mirror the thermal conditions during a specific stage of an accident scenario, where the lower portion of the bundle retained cold water. This chosen moment was expected to manifest the most pronounced temperature stratification within the cooling water pool.

The fluid domain was defined as compressible liquid water, and the Boussinesq approximation was employed as the fluid buoyancy model. This model allowed for representation of the buoyancy-driven flow dynamics within the system. Figure 5-7 provides a visual representation of the boundary and initial conditions utilized in the simulations.

For turbulence modeling, the k-ω shear stress turbulence (SST) model, renowned for its high accuracy in resolving turbulence behavior, was implemented. This choice was made to ensure the fidelity of the simulation results. Overall, the employed simulation strategy was a systematic and detailed approach to investigate the single-phase natural circulation stimulated by transferred heat flux to the cooling water in the pool due to condensation of super-heated steam in primary side of the NOKO facility, laying the foundation for subsequent stages of analysis involving more complex phenomena.

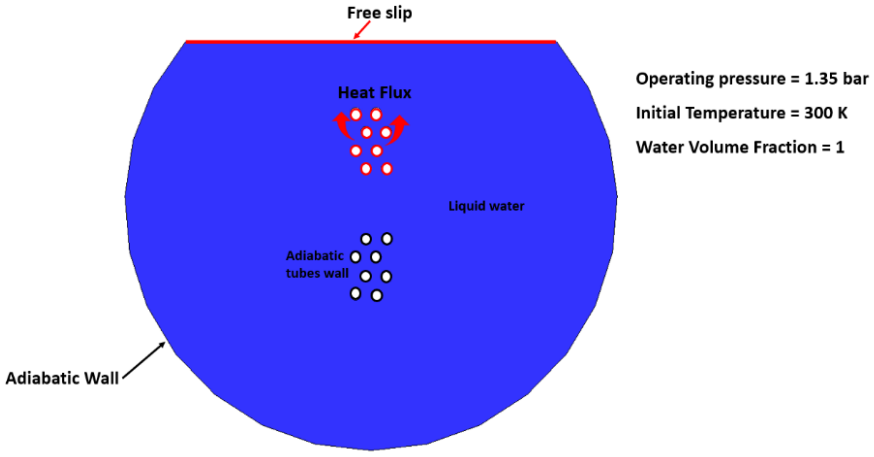

Figure 5-7. Initial and boundary conditions for single-phase CFD simulation set up

The high-resolution discretization scheme has been chosen in the solution section of the CFX software to increase the order-accuracy of discrete approximation [46]. The total simulation time is 2500s with time step equal to 0.01 s. Maximum Courant number calculated is equal to 0.25 and convergence is reached after 2-5 iterations for each time steps. Figure 5-8 shows the calculated temperature distribution in the fluid domain at 1800 s. This temperature profile of the fluid shows the temperature stratification within NOKO secondary side. Even after 1800 seconds after the beginning of the process, a very small volume of the fluid at the bottom of the tank is significantly colder than other areas because temperature rise in this region exhibits a gentler slope compared to the elevated areas.

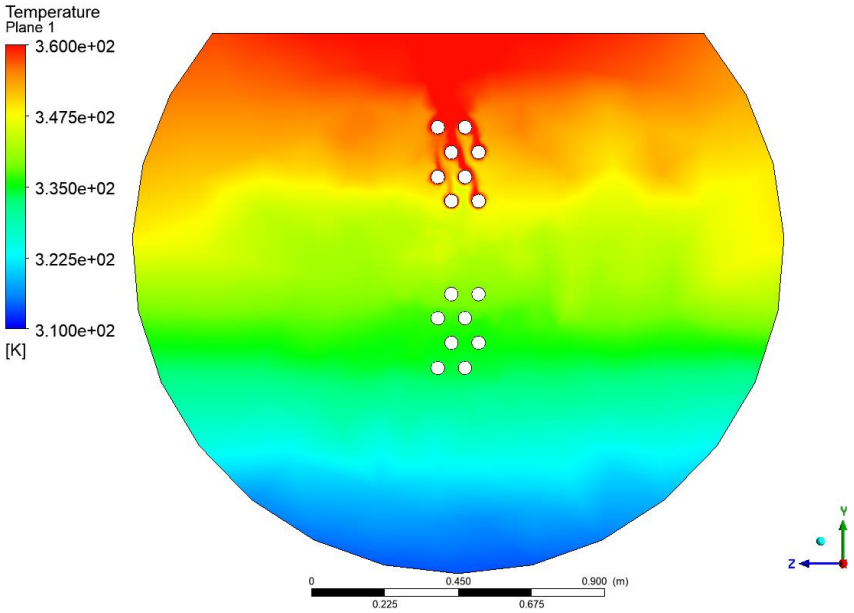

Figure 5-8. Temperature distribution calculated using single-phase CFD simulation at simulation time=1800 s

In order to show natural circulation of the fluid, velocity vectors in the secondary side and around the heated tubes are extracted from simulation and shown in Figure 5-9. As expected, the fluid in

contact with the heated tubes moves upwards due to buoyancy. This leads to a natural circulation of the fluid in the secondary side.

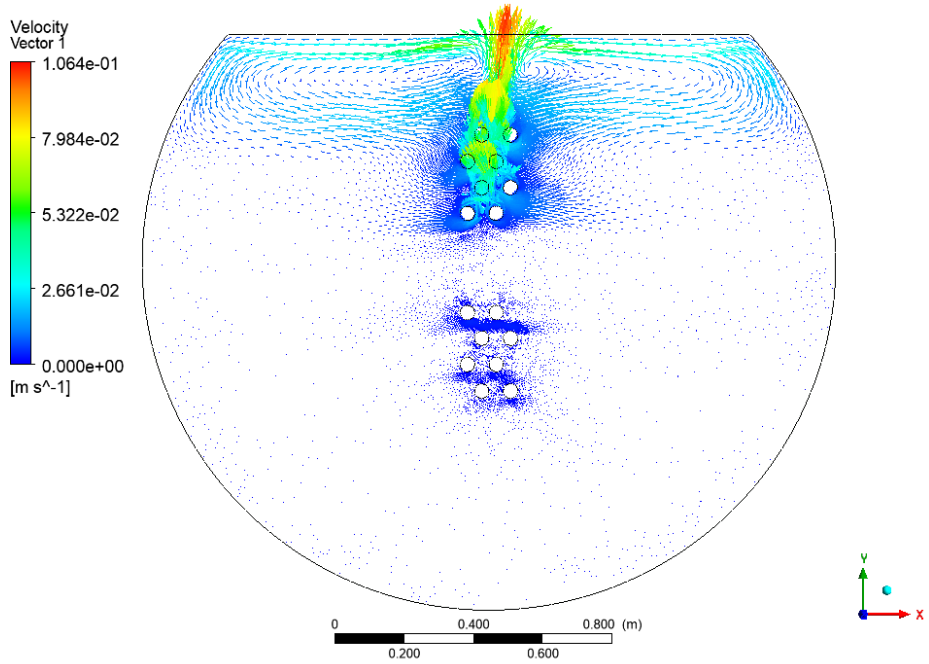

Figure 5-9. Velocity contours of the fluid in NOKO secondary side at t=1800 s

Furthermore, the transient temperature of all 11 locations corresponding to the thermocouples in the measurement plane D (see Figure 3-6) have been calculated in the simulation. The results have shown a symmetrical thermal behavior in the secondary side, so the thermocouples with the same elevation represented the same values during our calculations. Therefore, to show the evaluation of the results in a more organized way, the results of three thermocouples (TI3-D02, TI3-D03 and

TI3-D05) are selected from top to bottom and compared them with the experimental data of the NOKO_HZDR test facility. The results can be seen in Figure 5-10.

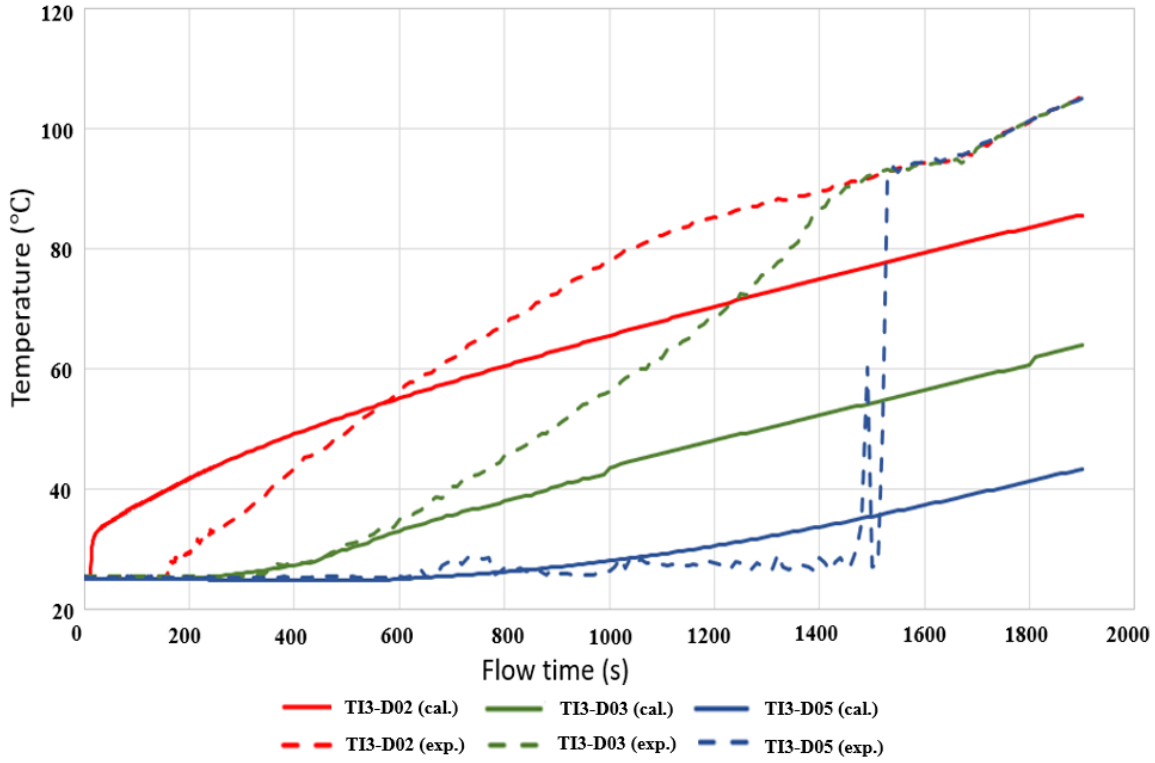

Figure 5-10. Comparison of the calculated results of the single-Phase simulation with NOKO experimental data

Figure 5-10 shows that the deviation between calculated results of the single-phase simulation with experimental data increases over the time. The reason for this behavior is the effect of the phase change is not resolved in these simulations. When the heating process continues, the evaporation happens; first in top of the secondary side and then in lower elevations. This affects the heat transfer rate of the heat exchanger and speeds up the temperature increase. The single-phase simulation is not capable to reproduce such thermal behavior in the calculation and that is the reason of showing uniform temperature increase during the time. Additionally, a notable spike occurs at the outset of the calculations, particularly in the region near the uppermost section of the tank. This discrepancy suggests that heat is being transferred more rapidly in this area than indicated by the experimental data. The sudden increase can be attributed to the time required for

heat to propagate to regions further from the heated surfaces via natural circulation. Moreover, this jump is observed in the experimental results as well, albeit with a slight delay and lesser magnitude compared to the calculated values. This inconsistency highlights another limitation of the current calculations. Therefore, single phase simulation is only suitable for a short period of the process, when the dominant heat transfer mechanism is single-phase natural convection.

5.3. Multi-phase CFD simulation for NOKO test facility

The phase change occurring within a large volume of water, coupled with the dynamic behavior of the free surface during the heat-up process, presents a complex yet compelling scenario that necessitates the adoption of multi-phase CFD simulations. In the case of large volumes of fluid undergoing heating, multi-phase CFD simulations are indispensable to accurately model the thermal hydraulic behavior of the fluid as free convection, subcooled and nucleate pool boiling phenomena happens.

In this section, two distinct conventional frameworks for conducting multi-phase CFD simulations have been used to assess their accuracy in predicting the intricate thermal characteristics of the fluid on the secondary side. The first employed framework was a Mixture model combined with Lee condensation-evaporation model for the calculations of the phase change. Mixture model is more suitable for subcooled boiling phenomenon and considers the two-phase flow as a composite of vapor and liquid phases, treating these phases as intermingling continua governed by a common set of equations. The model assumes that the phases are in a state of local thermodynamic equilibrium and computes interfacial phase change transfer terms by employing empirical closure relationships. The second framework uses an inhomogeneous Eulerian approach, which is well-regarded for its precision in predicting the thermal behavior of bubbly flows, especially when they are close to saturation. In this model, each phase is treated as a separate entity with its own properties like density, speed, and heat. It assumes that the phases fully mix, and it considers their interactions through transfer terms at their interfaces. In this framework, first Lee model for phase change has been used, then RPI wall boiling model has been added to the simulation set-up. In the

following section, the key equations for each model are presented, then it is explained how the simulations were set up, and at the end the results are discussed.

5.3.1 2D simulation with Mixture model

The mixture model is capable of simulation of different phases by solving the momentum, continuity and energy equations for the mixture. Additionally, it employs volume fraction equations for the secondary phase and algebraic expressions for the relative velocities. The momentum equation used for the mixture is shown in Equation 5-1. In this equation, *n* is the number of the phases, α is the volume fraction of each phase, $\vec{F}$ is a body force, ρ_m and $\vec{v}_m$ are mixture density and mass-averaged velocity, calculated using Equations 5-2 and 5-3.

$$\frac{\partial}{\partial t}(\rho_m \vec{v}_m) + \nabla.(\rho_m \vec{v}_m \vec{v}_m) = -\nabla p + \nabla.[\mu_m(\nabla \vec{v}_m + \nabla \vec{v}_m^T)] + \rho_m \vec{g} + \vec{F} - \nabla.\left(\sum_{p=1}^{n} \alpha_p \rho_p \vec{v}_{dr,p} \vec{v}_{dr,p}\right) \quad 5\text{-}1$$

$$\rho_m = \sum_{p=1}^{n} \alpha_p \rho_p \quad 5\text{-}2$$

$$\vec{v}_m = \frac{\sum_{p=1}^{n} \alpha_p \rho_p \vec{v}_p}{\rho_m} \quad 5\text{-}3$$

And μ_m is the mixture viscosity which can be calculated by Equation 5-4.

$$\mu_m = \sum_{p=1}^{n} \alpha_p \mu_p \quad 5\text{-}4$$

And $\vec{v}_{dr,p}$ is the drift velocity for the secondary phase as shown in the following:

$$\vec{v}_{dr,p} = \vec{v}_p - \vec{v}_m \quad 5\text{-}5$$

The continuity equation used in mixture model is described in Equation 5-6.

$$\frac{\partial}{\partial t}(\rho_m) + \nabla.(\rho_m \vec{v}_m) = 0 \qquad 5\text{-}6$$

The energy equation in mixture model is as follows:

$$\frac{\partial}{\partial t}\sum_p (\alpha_p \rho_p E_p) + \nabla.\sum_p \left(\alpha_p \vec{v}_p (\rho_p E_p + p)\right) = \nabla.\left(k_{eff}\nabla T - \sum_p \sum_q h_{q,p}\vec{J}_{q,p} + (\bar{\bar{\tau}}_{eff}.\vec{v})\right) + S_h \qquad 5\text{-}7$$

In this equation, $h_{q,p}$ is enthalpy of species q in phase p, $\vec{J}_{q,p}$ is the diffusive flux of species q in phase p, and k_{eff} is the effective conductivity calculated as follows:

$$k_{eff} = \sum \alpha_p (k_p + k_t) \qquad 5\text{-}8$$

In Equation 5-8, k_t is the turbulent thermal conductivity and $E_p = h_p$ (sensible enthalpy for phase k). The first three terms on the right-hand side of Equation 5-7 represents energy transfer due to conduction, species diffusion, and viscous dissipation, respectively. The last term, S_h is also the volumetric heat source which is eliminated in this simulation.

In this model, interfacial transfer plays a pivotal role in predicting the mass, momentum, and energy exchanges across the boundary separating phases. Within this framework, the interfacial area concentration, denoting the interface area between phases per unit mixture volume, is determined via transport equation-based models. This approach accommodates the variability in bubble diameters and incorporates the effects of coalescence and breakage. Notably, in this model, the discrete (particles) and continuous phases exhibit dynamic changes in size and distribution, driven by processes such as mass transfer between phases, expansion due to pressure fluctuations,

coalescence, breakage, and nucleation mechanisms. The transport equation governing the interfacial area concentration is expressed as follows:

$$\frac{\partial\left(\rho_g X_g\right)}{\partial t}+\nabla.\left(\rho_g \overrightarrow{u_g} X_p\right)=\frac{1}{3}\frac{D\rho_g}{Dt}X_p+\frac{2}{3}\frac{\dot{m}_g}{\alpha_g}X_p+\rho_g(S_{RC}+S_{WE}+S_{TI})$$

In this equation, X_p represents the interfacial area concentration ${m^2}/{m^3}$, and α_g is the gas volume fraction. The first two terms on the right-hand side account for gas bubble expansion resulting from compressibility and mass transfer (phase change), with $\dot{m}_g$ representing the mass transfer into the gas phase per unit mixture volume. S_{RC} and S_{WE} denote the coalescence sink terms due to random collision and bubble mixing, respectively, while S_{TI} represents the breakage source term attributed to turbulent impact. Notably, in this model S_{RC} and S_{TI} are computed using the Hibiki-Ishii Model, which provides a robust framework for their calculation. However, S_{WE} has been omitted in this formulation since the Hibiki-Ishii model does not incorporate this effect [47].

The mixture model, which solves fewer equations than other multiphase models, can achieve comparable performance in numerous situations especially in sub-cooled boiling regions [48]. In this simulation Schiller-Naumann model is used to calculate the drag force coefficient and a k-ω shear stress transport (SST) model is applied as turbulence model. To model phase change, Lee's model [49] is used as evaporation and condensation mechanism. In this model, the mass transferred between phases is calculated by evaluating the temperature of the liquid phase as Equation 5-9.

$$\dot{m}_{lv}=C.\alpha_l\rho_l\frac{(T_l-T_{sat})}{T_{sat}} \qquad 5\text{-}9$$

Where, α is the phase volume fraction, ρ is the phase density and *C* is related to the physical properties of the fluid.

In addition, a semi-Mechanistic boiling model has been added to this simulation. It is an empirical model to calculate the boiling on the heated walls developed by Chen [50]. In this model, the heat transfer coefficient to model nucleate boiling during heat up process is calculated by using Foster and Zuber correlation [50]. To calculate the slip velocity the Manninen-et-al model [51] has been employed. A continuum surface tension force modelling for water and vapor phases is added to the simulation setup [48]. To solve all the equations, different methods have been applied in the solution setup of the simulation. The SIMPLE iterative algorithm has been used to couple the

pressure and velocity in the solution method. In addition, the Least Square Cell Based gradient is used to discretize the diffusive terms. For energy, momentum, and volume fraction calculation, the first order upwind method and for the turbulent kinetic energy the second order upwind scheme are used [48].

5.3.2 2D simulation with Inhomogeneous Eulerian model

Eulerian model is a computational framework to simulate multi-phase problems by solving the conservation equations for each phase separately. This allows a comprehensive investigation of the complex interactions and dynamics between different phases. The momentum equation in Eulerian model is solved for q^{th} phase as follows:

$$\begin{aligned}\frac{\partial}{\partial t}\left(\alpha_q \rho_q \vec{v}_q\right) + \nabla.\left(\alpha_q \rho_q \vec{v}_q \vec{v}_q\right) \\ = -\alpha_q \nabla p + \nabla.\bar{\bar{\tau}}_q + \alpha_q \rho_q \vec{g} \\ + \sum_{p=1}^{n}\left(\vec{R}_{pq} + \dot{m}_{pq}\vec{v}_{pq} - \dot{m}_{qp}\vec{v}_{qp}\right) + \left(\vec{F}_q + \vec{F}_{vm,q}\right)\end{aligned} \quad 5\text{-}10$$

Where, $\vec{F}_q$ is external body force and $\vec{F}_{vm,q}$ is virtual mass force. $\bar{\bar{\tau}}_q$ is stress-strain variable. $\vec{v}_{pq}$ and $\vec{v}_{qp}$ are interphase velocities and the interphase force is defined by $\vec{R}_{pq}$.

The energy conservation equation in the Eulerian model is also formulated as Equation 5-11 and is solved for each phase during the computations in this framework.

$$\begin{aligned}\frac{\partial}{\partial t}\left(\alpha_q \rho_q (e_q + \frac{\vec{v}_q^2}{2})\right) + \nabla.\left(\alpha_q \rho_q \vec{v}_q \left(h_q + \frac{\vec{v}_q^2}{2}\right)\right) \\ = \nabla.\left(\alpha_q k_{eff,q} \nabla T_q - \sum_j h_{j,q}\vec{J}_{j,q} + \bar{\bar{\tau}}_{eff,q}.\vec{v}_q\right) + p\frac{\partial \alpha_q}{\partial t} \\ + \sum_{p=1}^{n}\left(Q_{pq} + \dot{m}_{pq}h_{pq} - \dot{m}_{qp}h_{qp}\right) + S_q\end{aligned} \quad 5\text{-}11$$

Where, $k_{eff,q}$ is the effective conductivity, Q_{pq} is the intensity of heat exchange between phases, $h_{j,q}$ is the enthalpy of species, $\vec{J}_{j,q}$ is the diffusive flux of species, e_q is internal energy ($e_q = h_q - \frac{p_{op}+p}{\rho_q}$), and S_q is enthalpy source term.

And Equation 5-12 is solved for phase q^{th} as continuity equation in the Eulerian model.

$$\frac{1}{\rho_q}\left[\frac{\partial}{\partial t}(\alpha_q\rho_q) + \nabla.(\alpha_q\rho_q\vec{v}_q) = \sum_{p=1}^{n}(\dot{m}_{pq} - \dot{m}_{qp})\right] \quad 5\text{-}12$$

Another benefit of Eulerian model is using various models to employ the interphase exchange between different phases. In this simulation Schiller and Naumann model [52] is used to calculate the fluid-fluid exchange coefficient (f) which is applied as drag force using Equation 5-13 to calculate.

$$f = \frac{C_D Re}{24} \quad 5\text{-}13$$

Where,

$$C_D = \begin{cases} 24(1 + 0.15Re^{0.687})/Re, & Re \leq 1000 \\ 0.44, & Re > 1000 \end{cases} \quad 5\text{-}14$$

Re is relative Reynolds number and is calculated for primary phase q and secondary phase p by using the Equation 5-15.

$$Re = \frac{\rho_q|\vec{v}_p - \vec{v}_q|d_p}{\mu_q} \quad 5\text{-}15$$

Also, to calculate lift force, Tomiyama [53] model is used. Turbulent dispersion and turbulence interaction have been taken into account by using Burns et al [54] model and Sato model [55] respectively.

To incorporate the phase transition phenomena into the computational analyses, two distinct approaches have been explored within the scope of this investigation. The initial approach involves the utilization of the Lee model, specifically designed to address evaporation-condensation processes, and the second one is RPI wall boiling model. The Lee model is used within the Eulerian framework when employing a singular interfacial heat transfer model for both phases. Under this

circumstance, the computation of liquid-vapor mass transfer is computed through the vapor transport correlation, as expressed by Equation 5-16.

$$\frac{\partial}{\partial t}(\alpha_v \rho_v) + \nabla.\left(\alpha_v \rho_v \vec{V}_v\right) = \dot{m}_{lv} - \dot{m}_{vl} \qquad 5\text{-}16$$

Where, $\dot{m}_{lv}$ and $\dot{m}_{vl}$ are the mass transfer rates due to evaporation and condensation, respectively and are calculated based on the temperature difference of the fluid with saturation temperature as follows:

$$f(x) = \begin{cases} \dot{m}_{lv} = coeff \times \alpha_l \rho_l \dfrac{(T_l - T_{sat})}{T_{sat}}, & T_l < T_{sat} \\ \dot{m}_{vl} = coeff \times \alpha_v \rho_v \dfrac{(T_{sat} - T_v)}{T_{sat}}, & T_v \geq T_{sat} \end{cases} \qquad 5\text{-}17$$

$coeff$ represents a coefficient requiring precise adjustment, akin to a relaxation time, while α and ρ denote the phase volume fraction and density, respectively. More detailed description of how to calculate $coeff$ can be found in [56, 57]. In this simulation, $coeff$ is used as the inverse of the relaxation time.

The second approach involving the incorporation of phase change phenomena is characterized by the utilization of a wall boiling model known as the RPI wall boiling model. Originating from the work of Kurul and Podowski [58] at Rensselaer Polytechnic Institute (RPI), this model was developed to quantify boiling occurrences in regions proximal to a heated surface, even though the bulk temperature remains below the saturation temperature. The distinctive attribute of the RPI wall boiling model lies in its determination of the total wall heat flux. This model operates as a superposition model, encompassing various heat transfer mechanisms occurring in the immediate vicinity of the heated wall within the adjacent liquid.

In this operational framework, distinct heat transfer mechanisms contribute to the effective wall heat flux. These include single-phase liquid convective heat transfer occurring in areas of the wall unaffected by nucleation sites, evaporative heat transfer transpiring at nucleation sites for vapor generation, and quenching heat transfer resulting in the superheating of the liquid to rise the bubbles from the surface (see Figure 5-11). Within the RPI wall boiling model, the cumulative heat flux originating from the wall is expressed as the combination of these diverse heat transfer

mechanisms, denoted as wall heat flux partitioning, and can be formulated as Equation 5-18. In this equation, $\dot{q}_c$, $\dot{q}_Q$ and $\dot{q}_E$ are convective, quenching and evaporation heat flux, respectively.

$$\dot{q}_{Wall} = \dot{q}_c + \dot{q}_Q + \dot{q}_E \quad 5\text{-}18$$

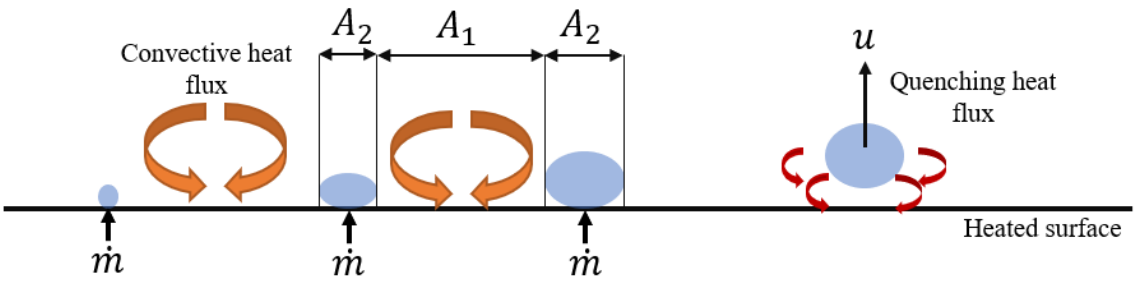

Figure 5-11. Different heat fluxes happening on a heated surface

Convective heat flux ($\dot{q}_c$) in Equation 5-18, is calculated as follows:

$$\dot{q}_c = A_1 . h_c . (T_W - T_L) \quad 5\text{-}19$$

In Equation 5-19, h_c is heat transfer coefficient of the single-phase liquid, T_W and T_L are the wall and liquid temperature, respectively. In this equation, A_1 defines the surface area of the heated wall that is not affected by nucleation sites ($1 - A_b$). This can be calculated using Equation 5-20.

$$A_b = \min\left(1, K\frac{N_w \pi D_w^2}{4}\right) \quad 5\text{-}20$$

Where, N_w is the active nucleation sites density, D_w is bubble departure diameter and K is an empirical constant that is dependent to the subcooled Jacob number (Ja_{sub}) as follows [59]:

$$K = 4.8e^{\left(\frac{Ja_{sub}}{80}\right)} \quad 5\text{-}21$$

$$Ja_{sub} = \frac{\rho_l C_{pl} \Delta T_{sub}}{\rho_v h_{lv}} \quad 5\text{-}22$$

In Equation 5-22, $\Delta T_{sub} = T_{sat} - T_l$ is the liquid subcooling, C_{pl} and ρ_l are specific heat and density of liquid, h_{lv} is also the latent heat of phase change.

There are different methods to calculate the active nucleation site density (N_w) and bubble departure diameter (D_w). In this work, Lemmert and Chawla [60] correlation is used to calculate

N_w and Tolubinski and Kostanchuk model [61] is used to calculate D_w. The related correlations can be seen in Equations 5-23 and 5-24.

$$N_w = C^n(T_w - T_{sat})^n \qquad 5\text{-}23$$
$$c = 185, n = 1.805$$

$$D_W = min\left(d_{ref}.exp\left(-\frac{\Delta T_{sub}}{\Delta T_{ref}}\right), d_{max}\right) \qquad 5\text{-}24$$
$$d_{max} = 1.4\ [mm], d_{ref} = 0.6\ [mm], \Delta T_{ref} = 45\ [K]$$

There are also other to calculate bubble departure diameter such as models proposed by Ünal [62] or Fritz [63].

The quenching heat flux in Equation 5-18, is calculated by Equation 5-25.

$$q_Q = \frac{2k_l}{\sqrt{\pi\lambda_l\tau}} A_b(T_w - T_l) \qquad 5\text{-}25$$

Where, k_l and λ_l are the thermal conductivity and diffusivity of the liquid, respectively, and τ is the periodic time.

The evaporation heat flux in Equation 5-18, is also calculated by Equation 5-26.

$$\dot{q_E} = \dot{m}.(h_v - h_l) \qquad 5\text{-}26$$

Where $\dot{m}$, is the mass flux transferred from liquid to vapor calculated as follows:

$$\dot{m} = \rho_v \frac{\pi D_w^3}{6} N_A f \qquad 5\text{-}27$$

Where, f is the frequency of bubble departure defined by Cole [64] model as shown in Equation 5-28.

$$f = \sqrt{\frac{4g(\rho_l - \rho_v)}{3\rho_l D_w}} \qquad 5\text{-}28$$

5.3.3 Boundary conditions of 2D CFD simulations

To avoid the huge computational time and complicated geometry, the influences of the primary side of the NOKO test facility are incorporated with appropriate boundary conditions. The boundary conditions for this simulation have been adjusted in accordance with experimental data. However, the experimental data of the NOKO test facility exhibits limitations in representing the

temperature profile of the fluid within the tubes. The available data reveals the temperature difference of the inlet and outlet fluid during the heat-up process, as illustrated in Figure 5-12.

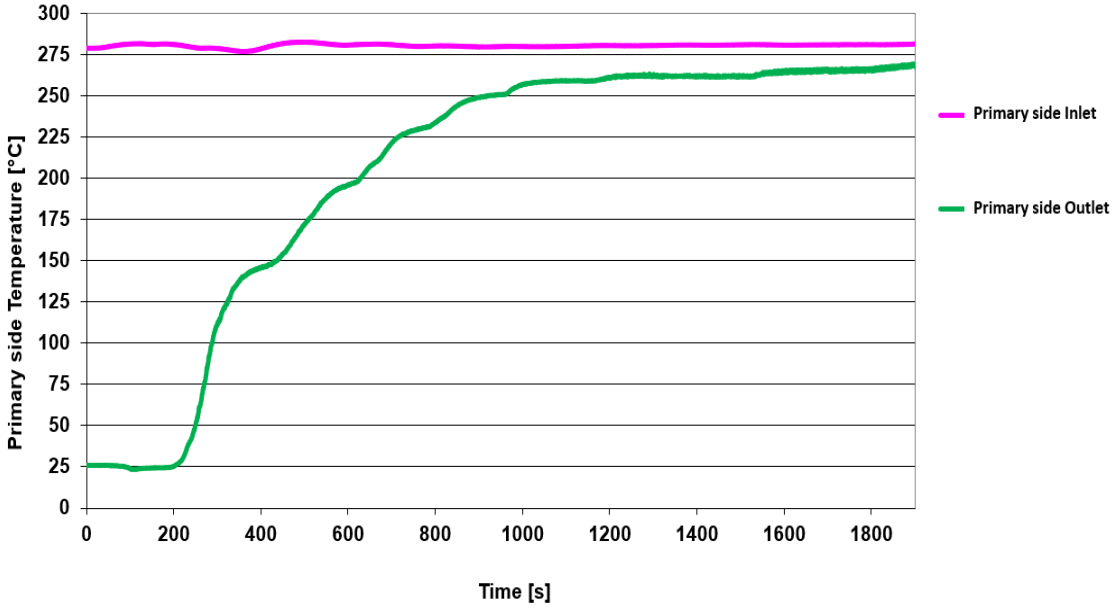

Figure 5-12. Temperature profile of the inlet and outlet of the primary side for experiment No. 65bar

As it can be seen in Figure 5-12 the inlet temperature of superheated steam in the primary side demonstrates a consistent profile, maintaining relative stability throughout the observed period. This is for Experiment No. 65bar where the primary side pressure is 65bar and saturation temperature is 275 ℃. This controlled inlet has been specifically designed for experiments, drawing inspiration from accidental scenarios in the reactor. In contrast, the outlet temperature undergoes distinct variations until it reaches the steady state condition. As time progresses, there is a rapid increase in the outlet temperature, which then gradually levels off. This happens because, at the start, the bundles are filled with cold water, and the temperature of the incoming superheated fluid is carefully controlled. As time passes, steam condenses in the upper bundle, and the resulting warm condensate mixes with the cold water in the lower bundle. This causes the outlet temperature to increase until the lower bundle is filled only with warm condensate, matching the steady-state condition of the upper bundle, where the temperature remains relatively constant.

Assuming that the phase change is happening in the upper bundle, it is observed that both the fluid temperature and the temperature of the wall maintain a relatively constant value in the upper

bundle [65]. In the lower bundle, the condensate water mixes with the cold water already present in the tubes, causing the fluid's temperature to rise gradually. As a result, the inner wall temperature of the lower bundle also increases gradually due to the change in fluid temperature in the primary side of the lower bundle. With the behavior of the inner wall temperature of the primary side elucidated for both the upper and lower bundles, and with knowledge of the total heat flux transferred from the walls to the secondary side, as well as their respective thermal conductivity and thickness, the transient outer wall temperature of both the upper and lower bundles can be calculated using Equation 5-29. After conducting a 2D CFD simulation for measuring plane D's location, its distance from both the inlet and outlet of the bundles has been considered. This information was gleaned from observations indicating that the temperature increase in the lower bundle begins approximately 200 seconds after the start of the process, which is for a length equivalent to 10 meters. However, for the upper bundle, situated at a length of 2.5 meters (the location of measuring plane D), the onset of temperature increase is estimated at 50 seconds. Conversely, for the lower bundle, where the fluid must traverse a 7.5-meter length to reach this location, the initiation of temperature rise is calculated to be 150 seconds.

$$Q = -kA\frac{dT}{dx} \qquad 5\text{-}29$$

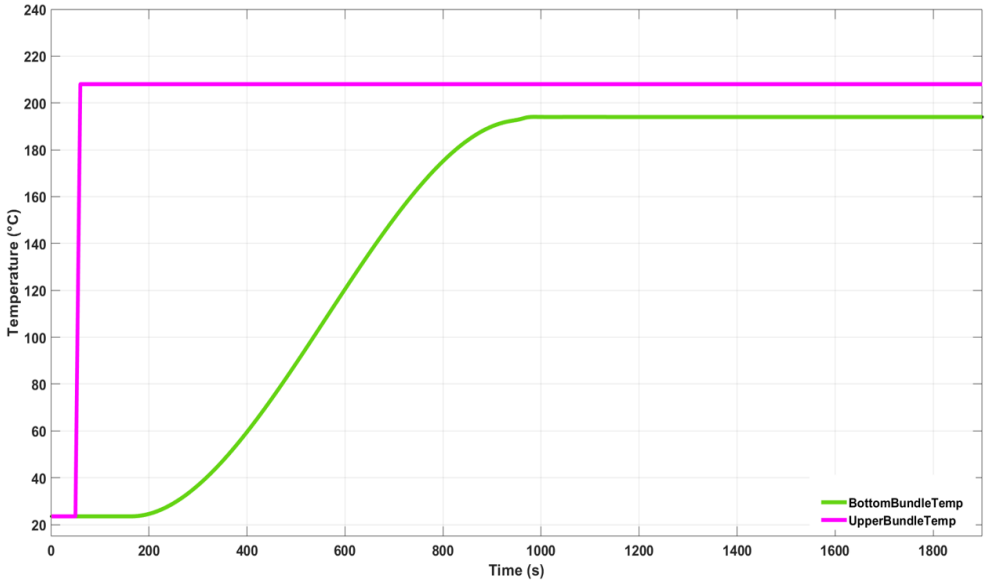

Figure 5-13. Profile temperature boundary conditions for tubes' bundle

The profile boundary condition that has been applied for outer wall temperature of upper and lower bundles in 2D CFD simulations has been shown in Figure 5-13.

The tank's wall is designated as an adiabatic barrier, and a free-surface boundary condition, ensuring free-slip, is implemented at the cooling water's top. The tank's wall is designated as an adiabatic barrier, and a free-surface boundary condition, ensuring free-slip, is implemented at the cooling water's top. The initial operating pressure is set at 0.1 MP (ambient pressure) due to the experiment's configuration, where the blow-off valves of the secondary side tank remain open. The initial temperature of the liquid on the secondary side is established at 300 K. The schematic of boundary conditions is demonstrated in Figure 5-14. This carefully designed setup creates specific conditions for the experiment, including thermal considerations and boundary conditions that contribute to the controlled nature of the system.

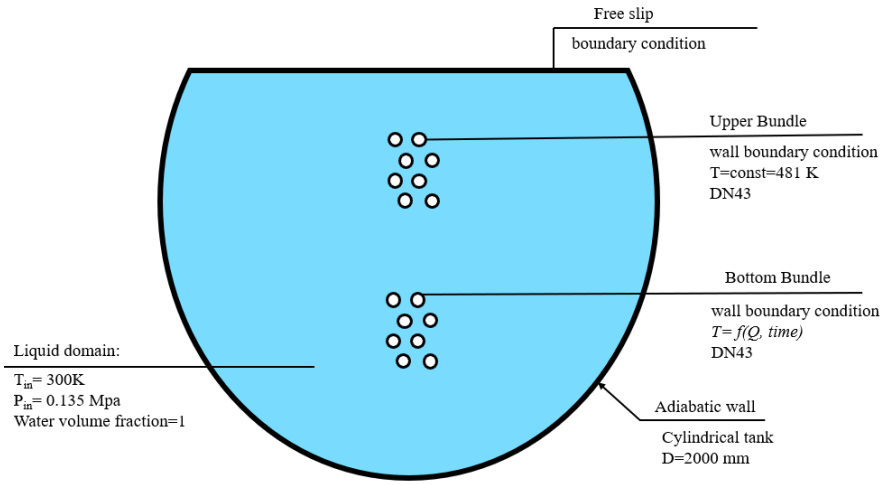

Figure 5-14. Initial and Boundary conditions of 2D CFD simulation

5.3.4 Results of 2D CFD simulation of mixture model

The results of the 2D CFD simulation in mixture framework are evaluated in this section. The calculations this model utilized unstructured mesh containing 114,254 elements, and the computational processes were performed on a High-Performance Computing (HPC) cluster. The

cluster utilized a single node equipped with 128 processing cores. The simulations spanned a duration of 2000 seconds and demanded a cumulative CPU time of 96~ 100 hours.

Throughout the heating phase, steam generation initiates near the surface of the heated tubes, circulating within the tank thereafter. Subsequent to this, steam condensation occurs within subcooled regions. The simulation results, specifically the volume fraction of vapor at t=1400 s (depicted Figure 5-15), shows the phase change that happened around the surface of heated tubes.

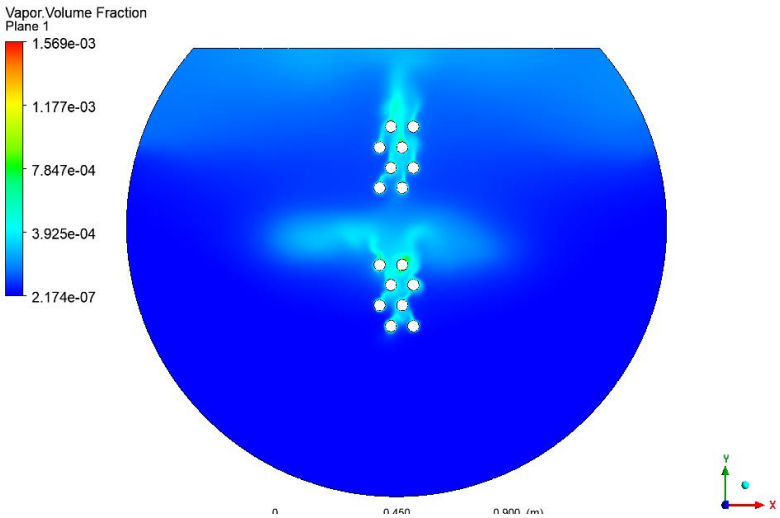

Figure 5-15. Calculated volume fraction of vapor in the secondary side at t=1400 s

Figure 5-16, Figure 5-17 and Figure 5-18, depict the temperature distribution in the secondary side for experiment No. 65 bar for different simulation times, respectively. To show the evolution of the temperature distribution in the secondary side during heating up process.

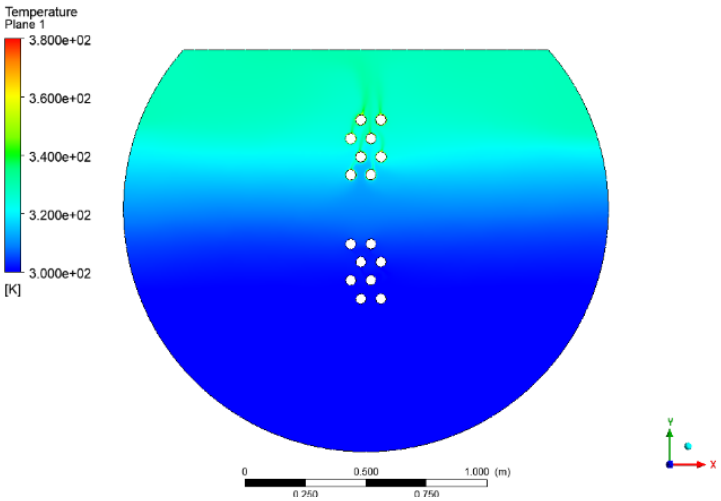

Figure 5-16. Calculated temperature distrubution of the secondary side at t=400 s

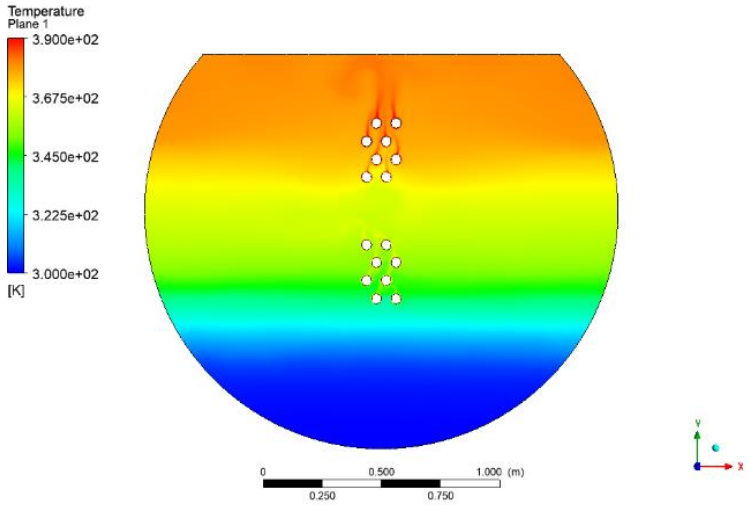

Figure 5-17. Calculated temperature distrubution of the NOKO secondary side at t=1400s

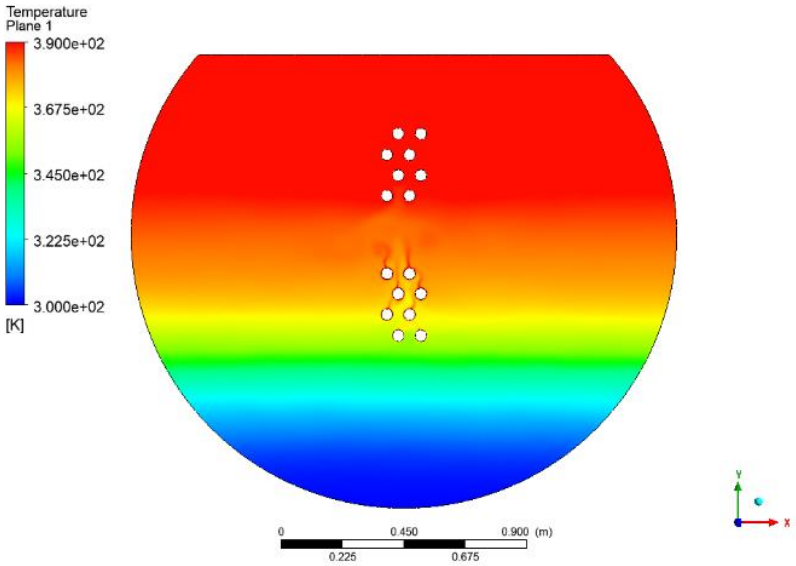

Figure 5-18. Calculated temperature distrubution of the NOKO secondary side at t=1800

Figure 5-16 , Figure 5-17 and Figure 5-18, reveal the presence of temperature stratification and how it evolves in the secondary side. It has been observed in both the experimental data and simulations that a stagnant zone is developed at the tank's bottom. Within this region, the temperature undergoes minimal change until the upper part of the tank approaches saturation temperature, as illustrated in Figure 3-7. Continuing through the process, the stagnant zone gradually heats up until it dissipates, leading to the observation of saturation temperatures throughout the entire tank. According to the experimental data, this transition occurs when a

sudden temperature increase is recorded in the lower part of the tank, typically around 1500 seconds of heat up process (refer to Figure 3-7).

Figure 5-19, Figure 5-20, and Figure 5-21, provide insights into the flow pattern of the natural circulation and its evolution during heating up process established within the tank. Notably, areas

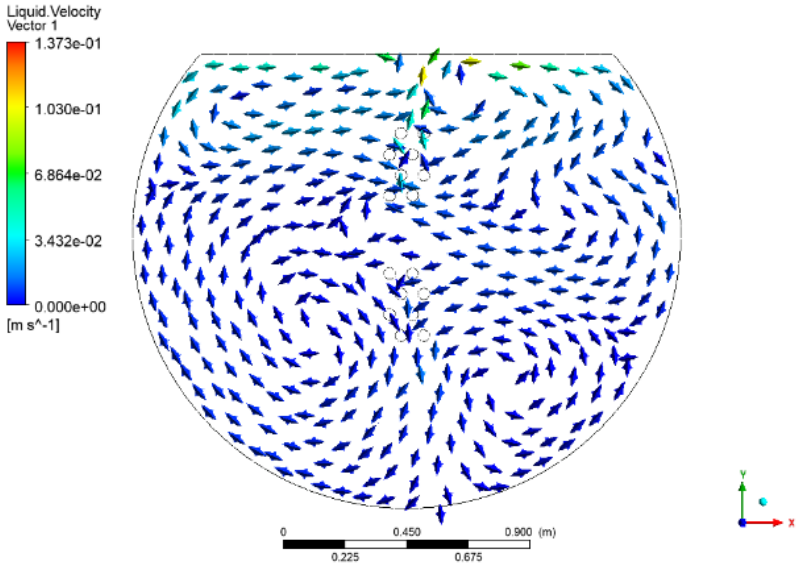

Figure 5-20. Velocity vectors from CFD calculation for NOKO secondary side at t=400 s

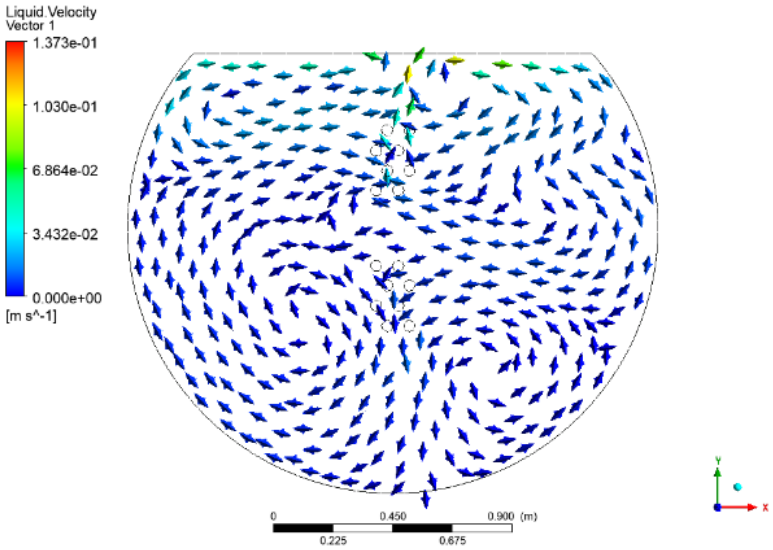

Figure 5-19. Velocity vectours from CFD calculations of the NOKO secondary side at t=1400 s

characterized by higher fluid velocity exhibit a more rapid increase in temperature due to enhanced convective processes.

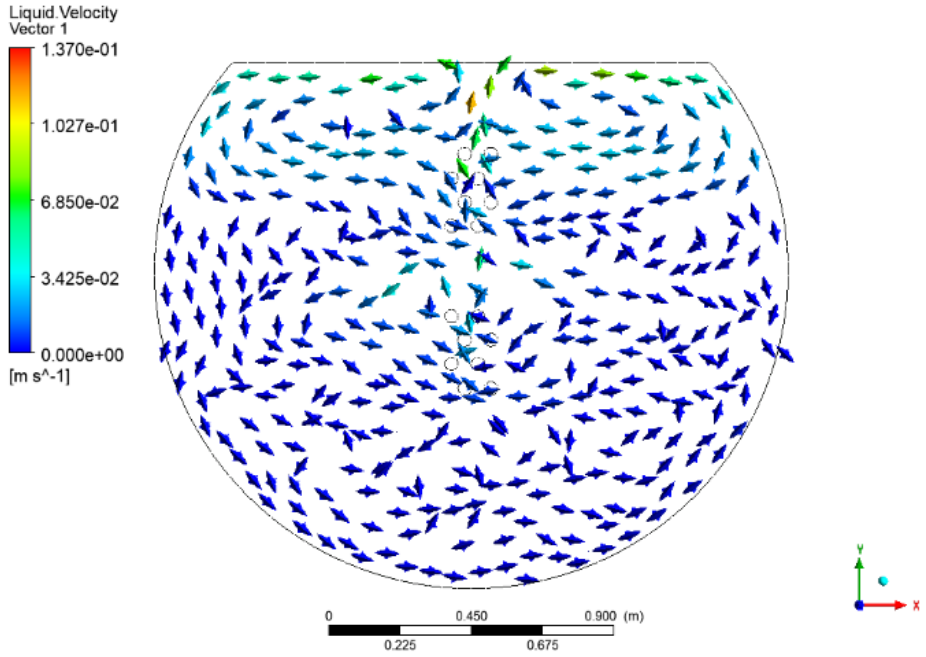

Figure 5-21. Velocity vectors from CFD calculations of the NOKO secondary side at t=1800 s

This main reason to depict these values is to shed light on the dynamic interplay between temperature distribution, fluid movement, and the evolution of the stagnant zone, contributing to a comprehensive understanding of the system behavior under the specified conditions. However, as expected, opting for this simplified approach led to significant differences when compared to experimental data. The transient temperatures calculated at three specified points extracted from

CFD simulation using mixture model were compared with the experimental data, as illustrated in Figure 5-22.

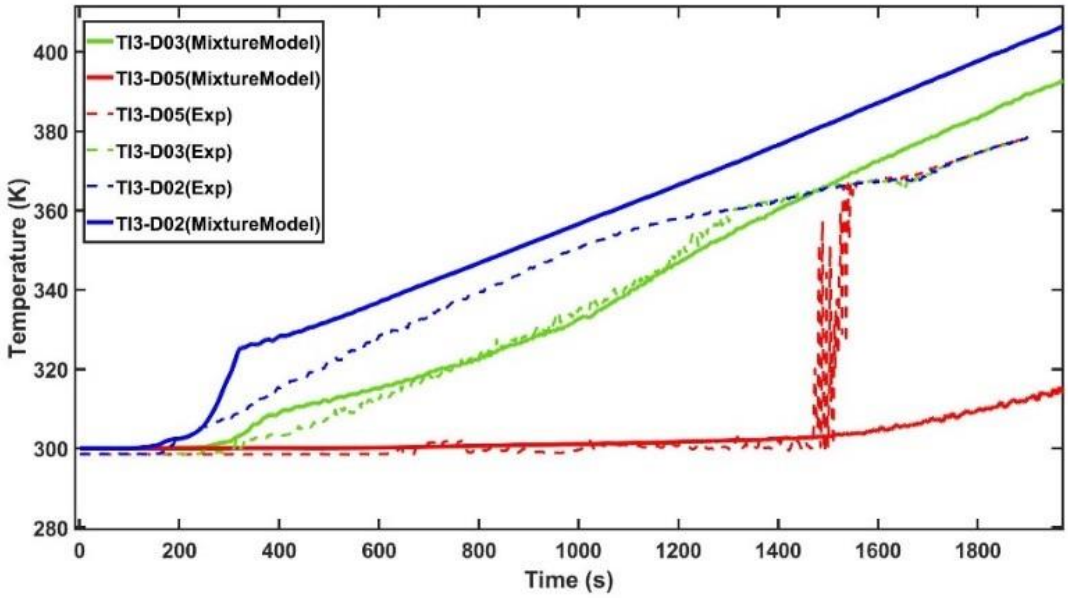

Figure 5-22. Comparison of calculated transient temperature from CFD simulation with mixture model and experimental data

Derived from experimental findings, the inactive zone at the tank's base undergoes a rapid temperature surge at time around 1500 s of the heat up process, until its complete disappearance. The entire tank volume is then enveloped by a two-phase flow regime, characterized by a mixture of water and vapor. This occurrence is understood as the consequence of a localized acceleration in velocity, attributed to steam generation and the downward progression of the boiling front. Interestingly, simulations employing the mixture model failed to replicate this abrupt temperature rise pattern (see Figure 5-22).

The phenomenon under consideration arises from the occurrence of steam condensation in proximity to the tubes within the system. This condensation is predominantly influenced by the subcooling effect. The complexity of this process is exacerbated by the fact that the thermocouples, are strategically positioned at locations distanced from the primary region of phase change. Consequently, the mixture model employed in the analysis proves insufficient in comprehensively accounting for the independent impact of this phase change on the evolution of fluid velocity. This limitation extends to its inadequacy in elucidating the consequential escalation in the heat transfer

coefficient within the secondary side of the system. Thus, the intricacies of the subcooling effect and the associated phase change dynamics necessitate a more refined model for a comprehensive understanding of the thermal processes at play.

In order to perform a mesh assessment, multiple mesh configurations with varying structural patterns and element counts were applied to the 2D geometry of the test study. The characteristics of each mesh for the mixture model are displayed in Table 5-1.

Table 5-1. The features of each mesh structure for mixture model

Mesh	Number of nodes	Number of elements	Inflation layer		CPU time (hour)
			Maximum Layers	Growth rate	
A	194220	87559	3	1.1	100
B	223681	103284	5	1.2	120
C	239628	114254	No inflation layer		128
D	252379	123481	No inflation layer		157

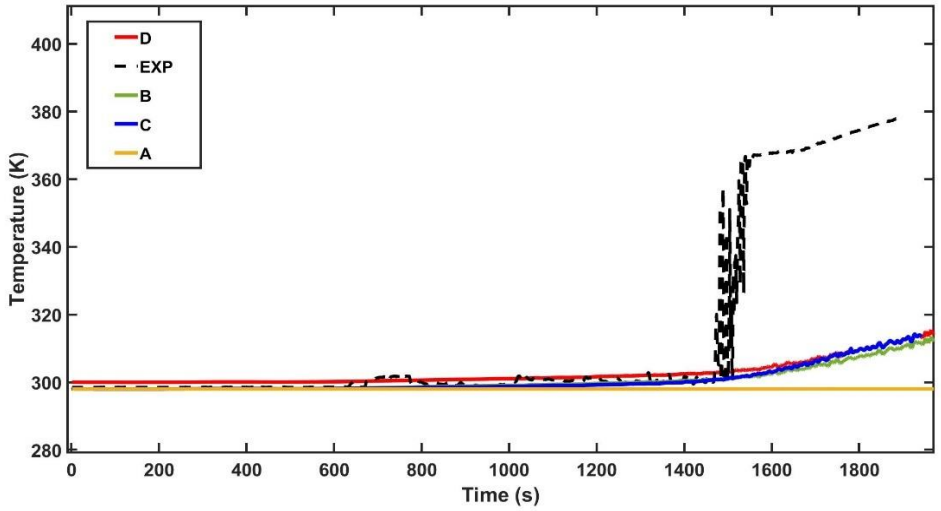

Figure 5-23. Measured and calculated transient temperature of thermocouple TI3-D5 for mixture model

The outcome of the 2D simulation using mixture model are assessed in this section. To depict this assessment, the calculated transient temperature at the most crucial location in the secondary side

—near the lower region of the tank, identified as thermocouple No. TI3-D5— is extracted and displayed in Figure 5-23.

These results demonstrate the clear independence of simulation outcomes from finer mesh structures. Consequently, the chosen mesh structure is affirmed as the optimized configuration.

5.3.5 2D CFD simulation results with Inhomogeneous Eulerian model

The outcomes of 2D CFD simulation in the framework of Inhomogeneous Eulerian model are presented here. The results include two distinct parts: one incorporating the Lee model as the phase change sub-model, and the other integrating the RPI wall boiling model.

Figure 5-24, Figure 5-24 and Figure 5-25, showcase the temperature distribution and its evolution on the secondary side during the heat up process, employing the Inhomogeneous Eulerian

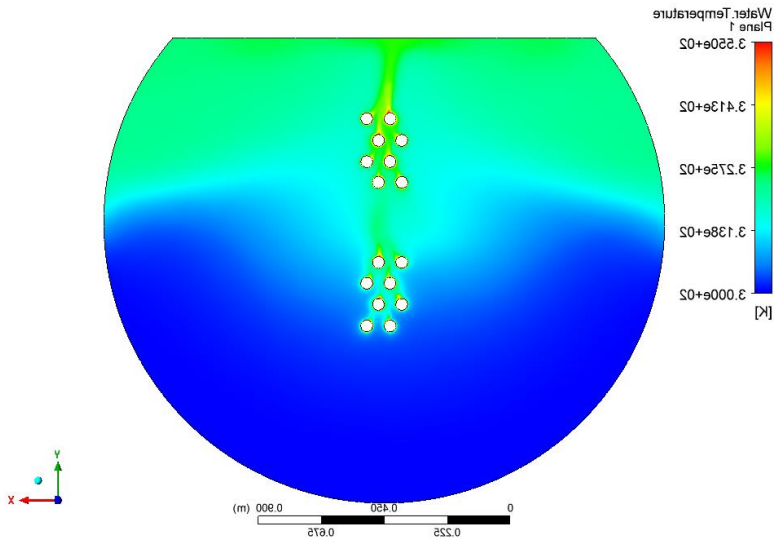

Figure 5-24. Temeprature distribution of CFD calculation with Inhomogenous Eulerian model with Lee model at t=400 s

framework with the Lee model. The sequential representation of temperature distribution over simulation time reveals a notable disparity between the calculated temperature evolution during the heating-up process with inhomogeneous Eulerian model and the results obtained via the mixture model.

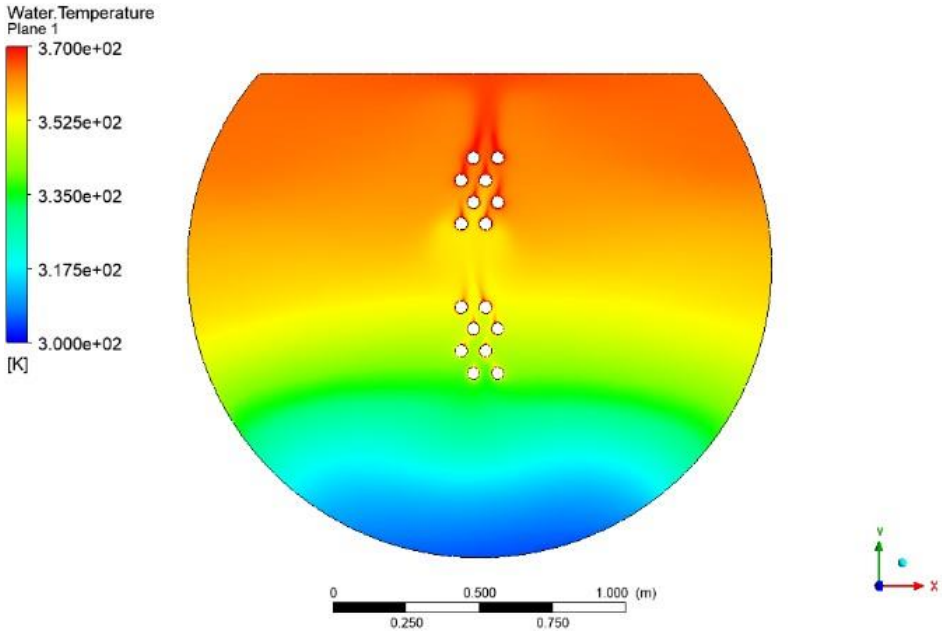

Figure 5-25. Temperature distribution of CFD calculation with Inhomogeneous Eulerian framewrok with Lee model at t=1400 s

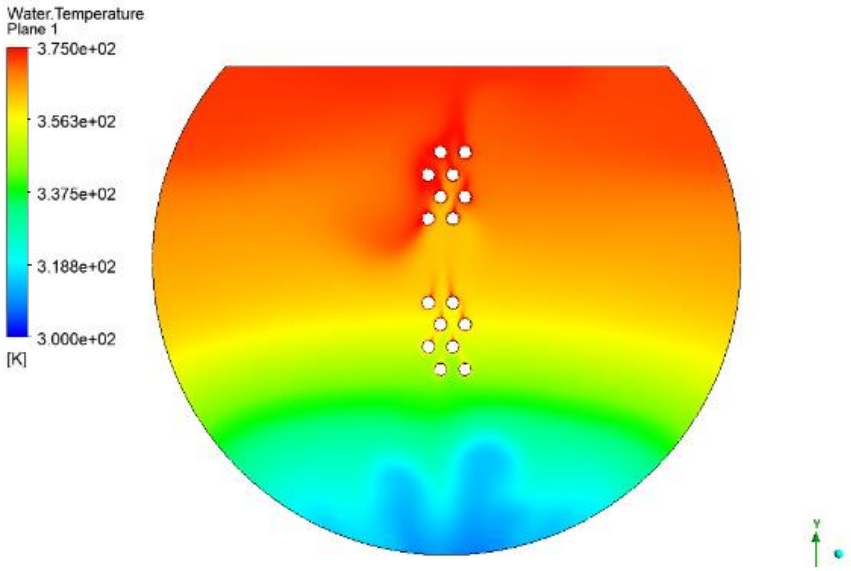

Figure 5-26. Temperature distribution of CFD calculation with Inhomogeneous Eulerian framewrok with Lee model at t=1800 s

In the Eulerian model outputs, although a stagnant zone is also observed at the bottom of the tank, it tends to dissipate gradually and faster after a certain duration from the start of the simulation. Initially, the temperature distribution exhibits greater resemblance to the mixture model in the earlier simulation times (e.g., t=400). However, this pattern undergoes significant changes as the simulation time progresses.

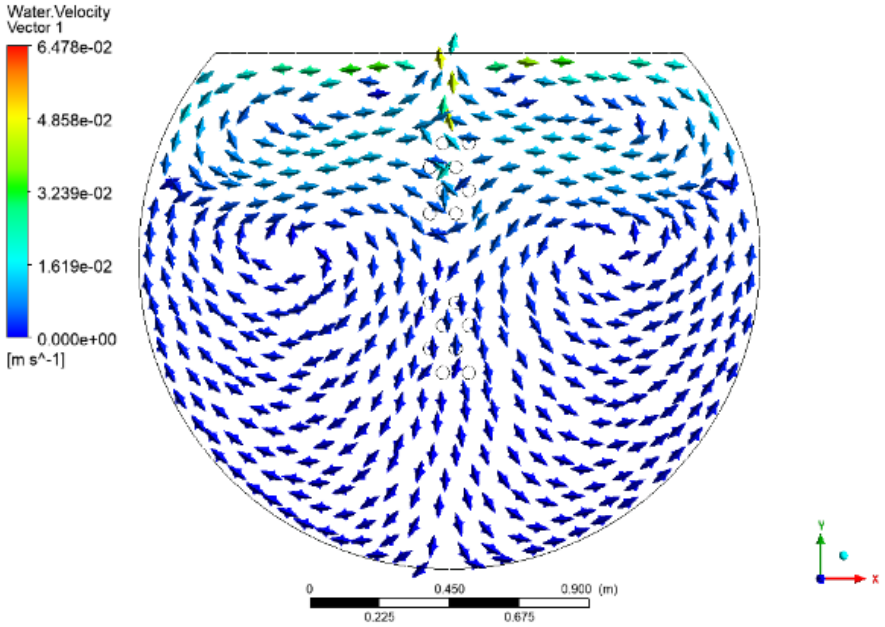

Figure 5-27. Velocity vectors of CFD calculation with Inhomogeneous Eulerian framework with Lee model at t=400s

Figure 5-27, Figure 5-28 and Figure 5-29, represent the velocity vectors of CFD calculations with Inhomogeneous Eulerian framework with Lee model, their distribution and their progress during heat up process. The evolution of velocity contours also exhibits apparent variations. Initially, similar to mixture model, velocity gradients are primarily evident at higher elevations closer to the upper tube bundle. However, in Eulerian model, as the heating-up process continues, additional vortices emerge at the bottom of the tank due to heat transfer from the lower tube bundle. Moreover, as phase change phenomena commence after a certain duration, the velocity distribution

in the bottom of the tank is further influenced. This phenomenon contributes to an abrupt increase in temperature in the lower regions of the tank.

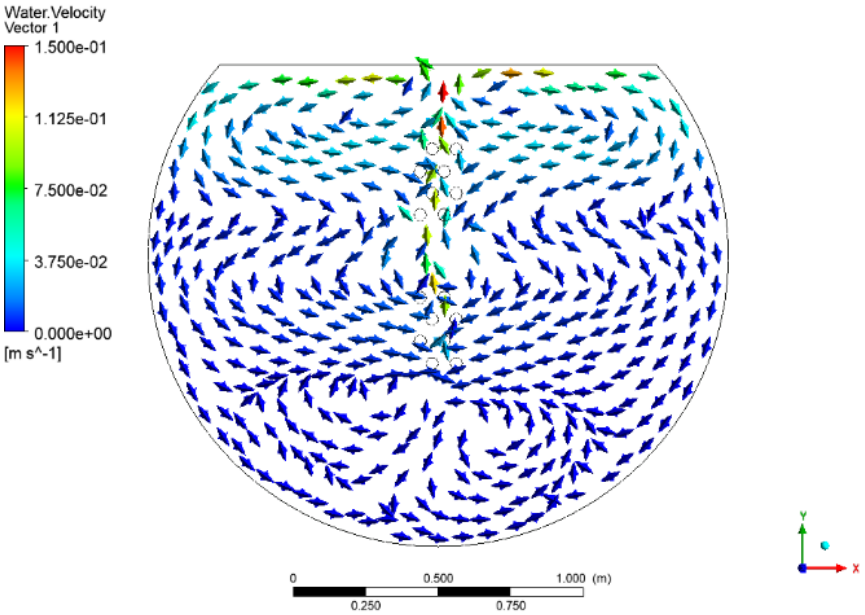

Figure 5-28. Velocity vectors of CFD calculation with Inhomogeneous Eulerian framework with Lee model at t =1400s

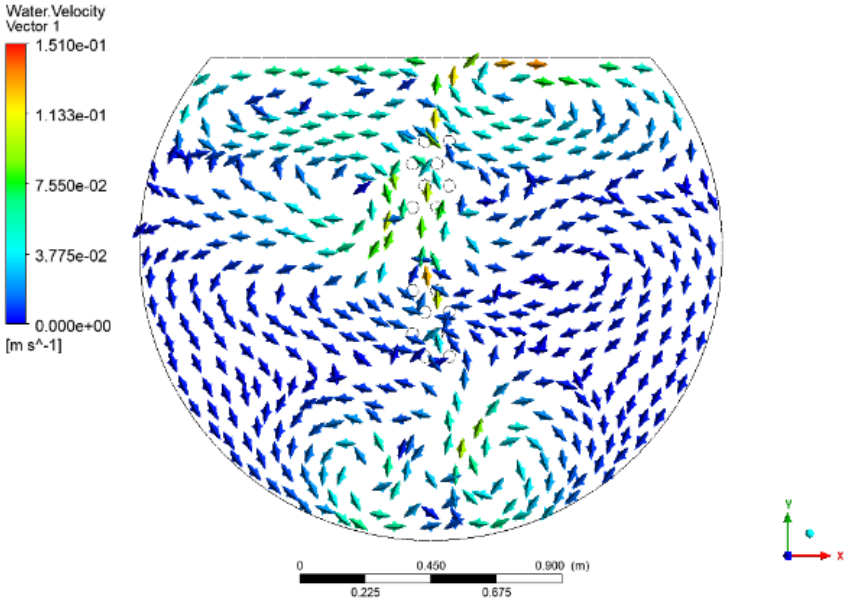

Figure 5-29. Velocity vectors of CFD calculation with Inhomogeneous Eulerian framework with Lee model at t =1800 s

The execution of this simulation, employing the same configuration on HPC cluster with an unstructured mesh comprising 123,707 elements, demanded 240 hours of CPU time.

To show the pattern of the phase change in the secondary side, the volume fraction of liquid water in the secondary side at the same simulation time is depicted in Figure 5-31Figure 5-30. As anticipated, the initiation of phase change on the heated surface of the tubes commences from the

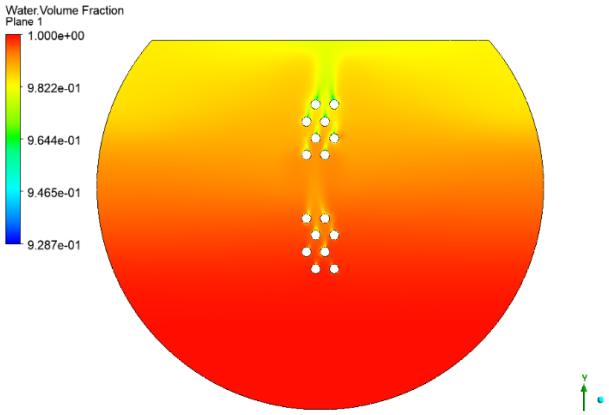

Figure 5-31. Volume fraction of water liquid in secondary side from simulation in Eulerian framework with Lee model at t=1400 s

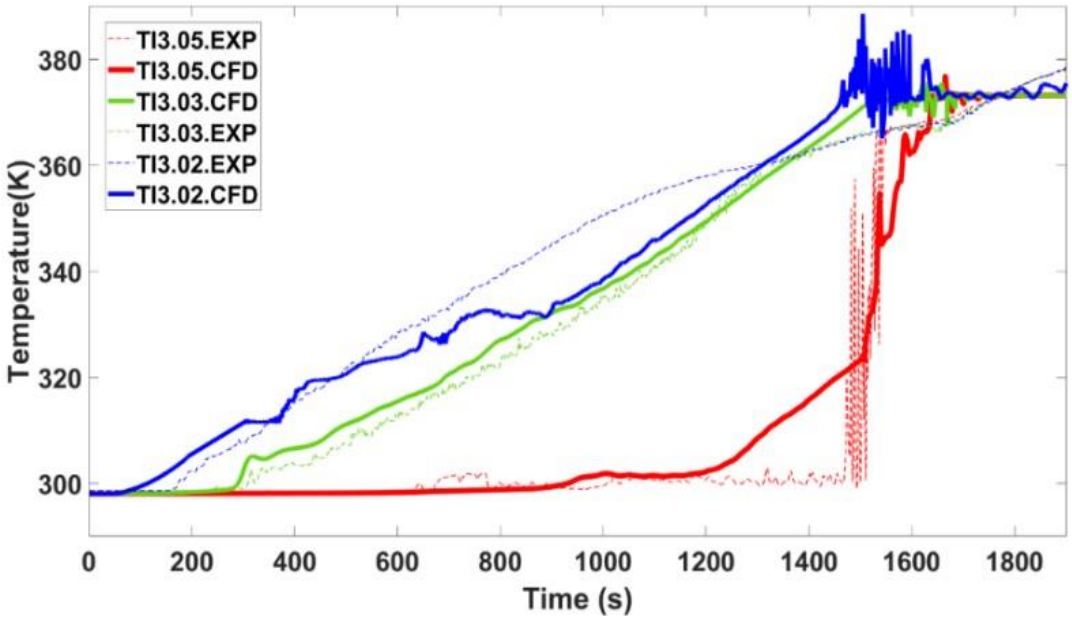

Figure 5-30. Calculated and measured transient temperature of simulation in Inhomogeneous framewrokd with Lee model

upper segment, wherein a transition to vapor phase occurs. Conversely, the lower segment of the tube exhibits a singular phase comprising liquid water, indicative of the occurrence of natural convection exclusively within this region.

The transient temperatures of the identical three locations, as observed in the case of the mixture model, have been compared with the experimental data, as illustrated in Figure 5-30. As can be seen in this figure, the utilization of the Eulerian approach has significantly enhanced the accuracy of the numerical results. Remarkably, the abrupt temperature surge noted in experiments in the lower region of the secondary side is accurately reproduced.

In this simulation, the average Y+ value for heated surfaces is set at 10, ensuring proper calculation of phase change phenomena with enhanced wall functions. To assess the grid independence of the model, five different sets of computational grids are analyzed. The characteristic of each mesh is shown in Table 5-2.

Table 5-2. Features of each mesh structure for mesh independancy study in Eulerian framework

Mesh	Number of nodes	Number of elements	Inflation layer		CPU time (hour)
			Maximum Layers	Growth rate	
A	205940	99985	3	1.1	168
B	259486	124813	5	1.2	216
C	249274	123707	No inflation layer		210
D	272953	135612	No inflation layer		240
E	327236	158723	No inflation layer		284

The same critical point of the case study which is related to the temperature of the fluid at the location of thermocouple No. TI3-D5 has been chosen to compare the results. Figure 5-32 shows the extracted results from each simulation.

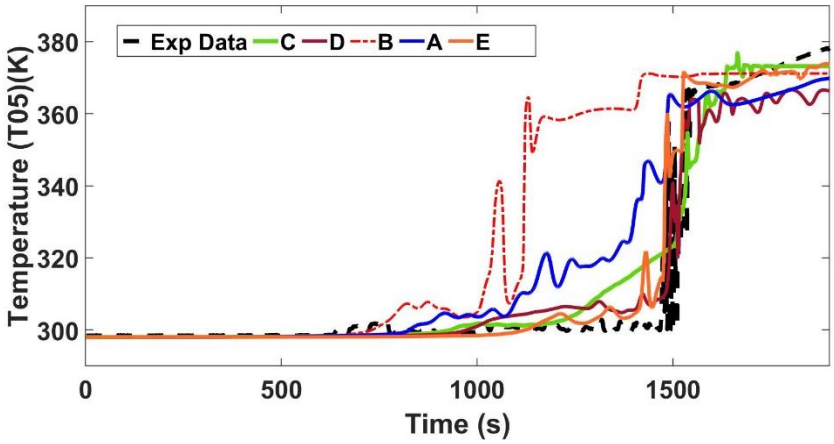

Figure 5-32. Measured and calculated transient temperature of thermocouple TI3-D5 for Inhomogeneous framework with Lee model with mesh A-E

As depicted in Figure 5-32, the computed temperature transients exhibit notable variations across distinct mesh structures of A and B and shows converging behavior between mesh C, D and E. It also shows that the sudden temperature increase (temperature jump) happens at the same time for the results of mesh C, D and E as well as experimental data.

To explore alternative models in multi-phase CFD simulation, the RPI wall boiling model has been incorporated into the simulation setup. The details of the sub-models used in this boundary model is described in 5.3.2 section. The benefit of RPI wall boiling model is that it is specifically developed to accurately model the bubble formation on the heated surfaces with precise calculation of the heat flux transferring to the adjacent fluid considering all possible heat transfer mechanisms.

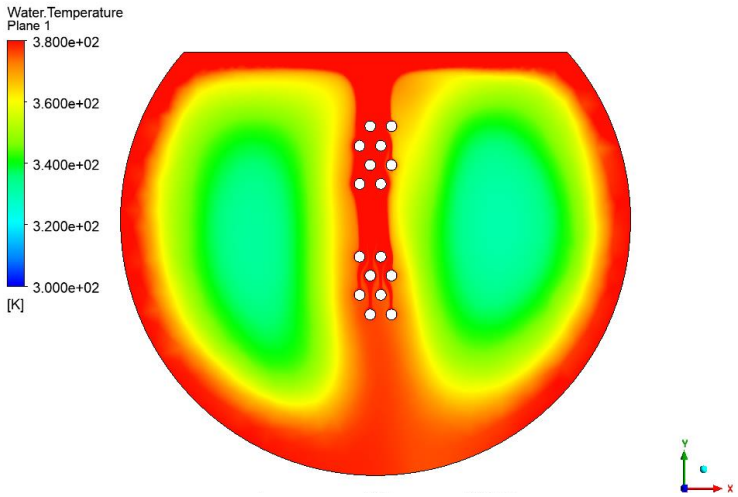

Figure 5-33. Temperature distribution of liquid water in secondary side using Inhomogeneuos Eulerian framework with RPI wall boiling at t=1400s

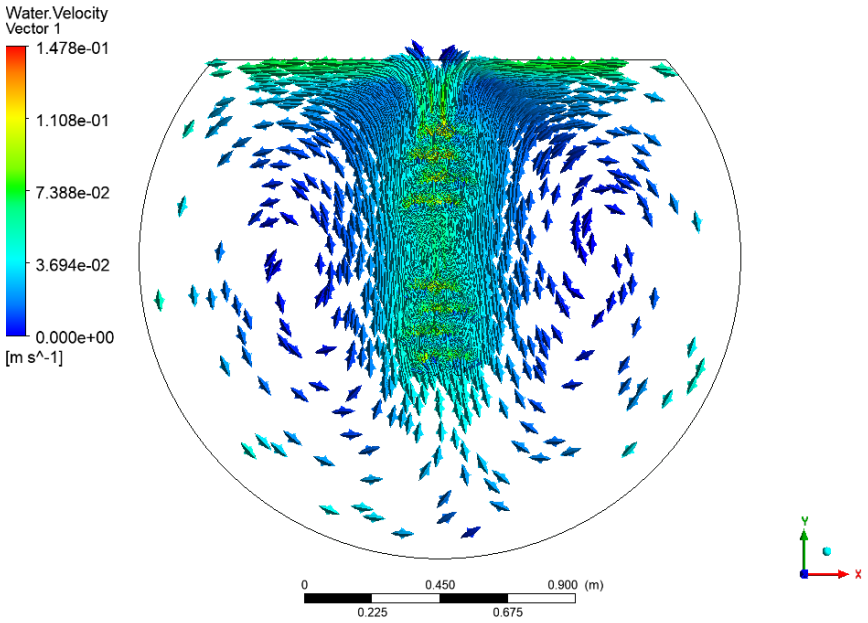

Figure 5-34. Velocity countours of liquid water in secondary side using Inhomogeneuos Eulerian framework with RPI wall boiling at t=1400s

However, this effort to accurately model the phase change on the heated surface increases the complexity of the simulation model as well as the computational costs. Moreover, the RPI wall boiling model was initially designed for boiling under high-pressure operating conditions. Consequently, achieving convergence in this case study, where the pressure is close to ambient pressure, has presented significant challenges. The execution of this simulation, employing the same configuration on HPC cluster with an unstructured mesh comprising 123,707 elements, demanded 336 hours of CPU time.

Temperature distribution and velocity contours of the fluid in the secondary side have been represented in Figure 5-33 and Figure 5-34, respectively.

As evident from the preceding Figure 5-33 and Figure 5-34, the outcomes of simulations employing the RPI wall boiling model exhibit visible distinctions compared to the outcomes derived from prior models. These results manifest an augmented fluid circulation rate, achieving complete mixing as the temporal evolution of the process follows. Furthermore, the observed dynamics indicate that the stagnant fluid in the lower regions of the tank deviates from the

anticipated clarity in its spatial configuration. The volume fraction of the liquid water is also extracted from simulations to show how it differs from prior models, Figure 5-35.

Figure 5-35. Volume fraction of liquid water in the tank extracted from simulation in Eulerian framework with RPI wall boiling at t=1400 s

The calculated volume fraction in this framework shows similar behavior in this modeling set up compared to prior modeling. However, to investigate more, the identical three locations, chosen in previous modeling, have been compared with the experimental data, as illustrated in Figure 5-36. This figure elucidates a heightened impulsivity in the transient temperature profiles at all three monitored locations, as compared to previous CFD results. These pronounced fluctuations underscore the RPI boiling model's heightened sensitivity to a range of factors like pressure in the given setup. Notably, the RPI model has historically been employed in high-pressure systems; however, its application under the quasi-ambient pressure conditions of this experiment reveals a marked increase in discrepancy. This discrepancy arises from the circulation of fluid driven by the heat transfer process, rather than accurately reflecting the temperature stratification observed in experiments. Despite this, the model is able to capture the abrupt temperature elevation in the tank's lower section. This can be seen in Figure 5-36. However, the impulsive behavior of calculated results with RPI boiling model doesn’t show significant improvement compared to Lee evaporation condensation model. It also must be emphasized that the computational demands of

integrating the RPI wall boiling model into the simulation framework are substantial, thus posing significant implications for its practical deployment.

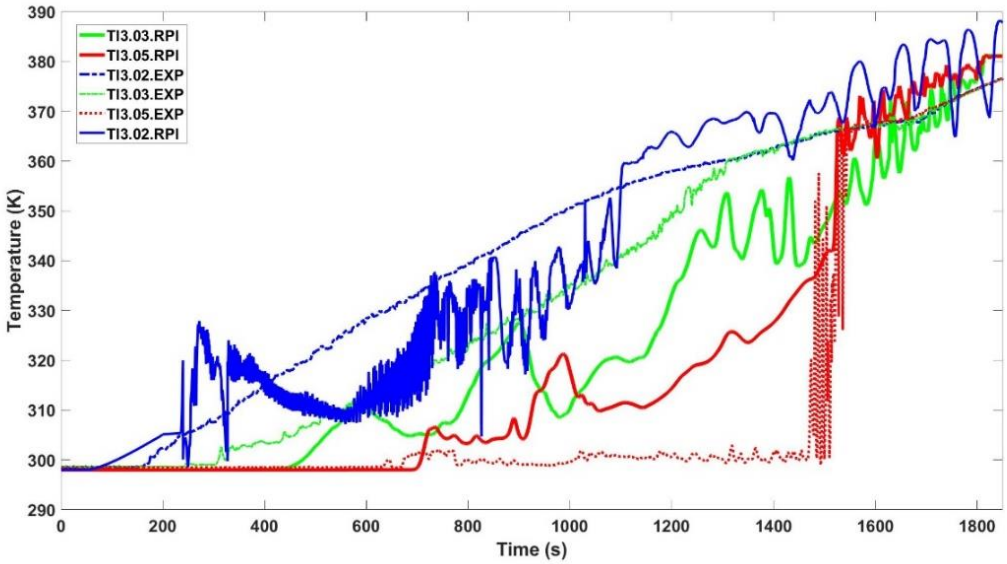

Figure 5-36. Calculated and measured transient temperature of simulation in Inhomogeneous framewrokd with RPI wall boiling model

An evaluation of the proficiency of simulations conducted within the Eulerian framework employing the Lee model and RPI wall boiling model has been delineated for the purpose of

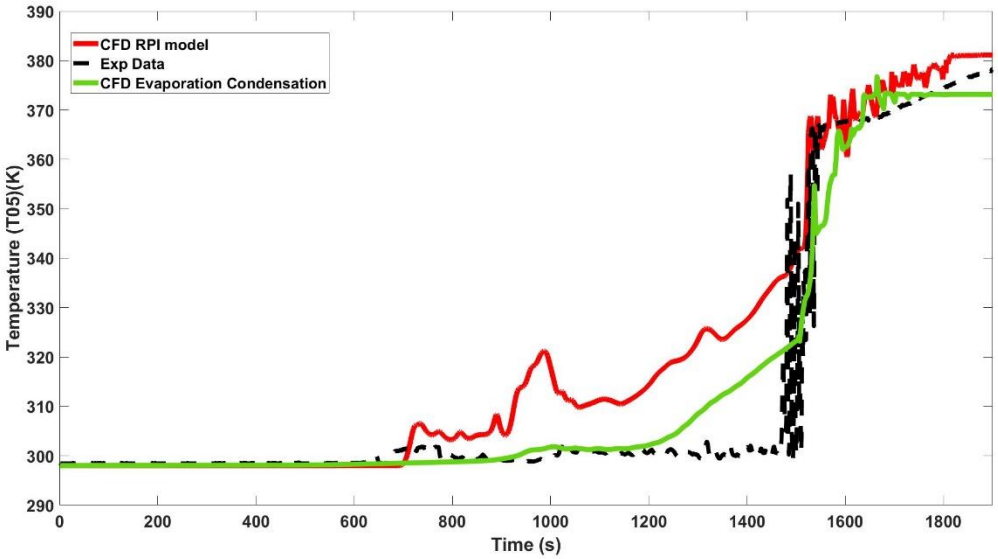

Figure 5-37. Transient temperature of the RPI simulation and its comparison with NOKO experiments and Lee model

replicating the critical dynamics of transient temperature at the designated position of thermocouple No. TI3-05, as illustrated in Figure 5-37.

The outcomes of the comparative analysis also show the sufficiency of the CFD calculations within inhomogeneous Eulerian Framework with Lee model over RPI wall boiling model. Despite successfully replicating the temperature jump phenomenon in the lower region, the Lee model exhibits a comparatively more stable behavior in depicting the transient temperature dynamics of the fluid within this particular domain.

5.3.6 Energy Balance Evaluation for 2D CFD simulations

To further validate the CFD methods, an energy balance evaluation has been carried out. The purpose of this assessment is to demonstrate the agreement between the computed total heat flux transferred to the fluid on the secondary side and the corresponding experimental data. The validation is based on the total heat flux when the steady state condition is reached in the process. This determination has been carried out through the utilization of Equation 5-30 in experimental data.

$$\dot{Q} = \dot{m}.C_p.\Delta T + \dot{m}.\Delta h_{phase} \qquad 5\text{-}30$$

Where ΔT it the temperature difference between inlet and outlet fluid of primary side, $\dot{m}$ is the mass flow rate and Δh_{phase} is latent heat of the fluid.

The transient heat flux transferred from tubes' wall to the adjacent fluid has been recorded in CFD codes for Mixture and Eulerian models. The results of this calculation can be seen in Figure 5-38. The feasibility of calculating transient heat flux from experiments is hindered by the instrumentation utilized in NOKO facility. The temperature measurement in the primary loop was conducted only at the inlet and outlet. For the first 200 seconds of the experiment, the condensate does not reach the outlet, so the available temperature data is not representative of the actual temperature drop in the condensate and does not provide reliable means to calculate sensible heat transferred to the coolant. In addition, until all the initial cold water is removed from the primary loop, at least part of the heat of condensation and further cooldown is removed by mixing within the primary loop, rather than transported via tube wall to the pool. Therefore, a comparison was made between the calculated heat flux results from CFD and the steady-state heat flux observed in

experiments. In practical terms, the heat flux transferring from the tube walls to the secondary side gradually increases throughout the process. This has been also represented in Figure 5-38. It is noteworthy that the steady state condition is achieved earlier in experiments compared to CFD calculations due to the delay in sensing heat in the secondary side relative to the primary side. As it can be seen in Figure 5-38, the discrepancy between the calculated heat flux, as derived from the CFD simulation and experimental data under steady-state conditions, is approximately 12.5%. This variance reflects an underestimation when employing the Mixture and Eulerian framework with Lee's model, whereas an overestimation of around 13% is observed when using the RPI wall boiling model.

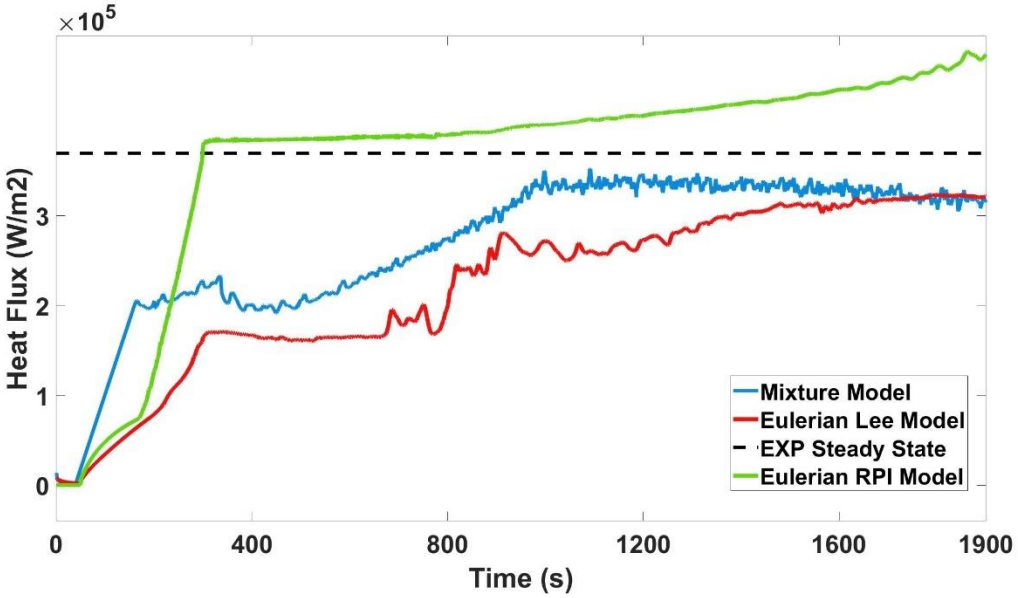

Figure 5-38. Total heat transfer rate from primary side to the secondary side unsing different CFD models and experimental data

5.4. 3D CFD Simulation with Inhomogeneous Eulerian model

Upon the conclusion of the 2D CFD simulation, an endeavor to extend the investigation to 3D simulation has been undertaken in this study. The objective is to elucidate the three-dimensional thermal behavior of the fluid within the secondary side, thereby enhancing the understanding of phenomena in passive heat removal systems. However, the intricate and expansive geometry of

the NOKO test facility results in prohibitively high computational costs, rendering a comprehensive 3D simulation economically unfeasible. Consequently, a degree of simplification is imperative for the execution of the 3D CFD simulation.

In order to constrain computational expenses to a manageable range, a pragmatic approach involves modeling a singular U-shaped tube with equivalent area of all eight tubes present in the NOKO apparatus. This streamlined representation facilitates the simulation process while retaining key aspects of the thermal behavior. The chosen singular U-shaped tube is immersed within a cooling water reservoir designed to replicate the dimensions of the NOKO facility. The adopted 3D geometry with the boundary and initial conditions of simulation set up is illustrated in Figure 5-39.

In this geometric configuration, the meshing comprises 4,599,400 elements. The substantial augmentation in element count has resulted in a notable escalation in computational requirements, quantified at 672 CPU hours. To streamline the simulation, boundary conditions have been simplified by deducing them from the steady state condition of the primary side. This simplification assumes a linear decrease in temperature along the length of the tubes and is applied as a boundary condition. Additionally, the tank's wall is treated as an adiabatic surface.

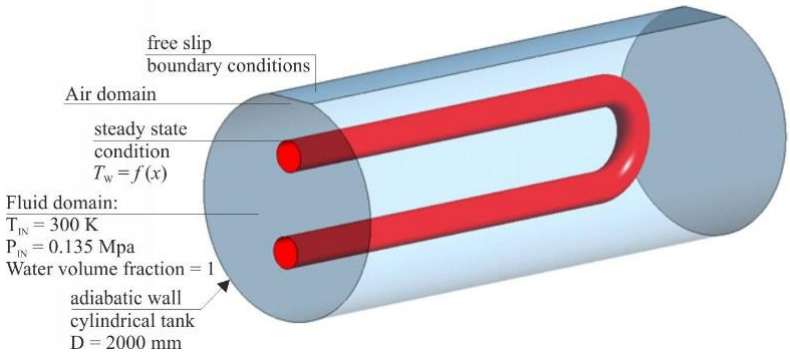

Figure 5-39. Simplified geometry for 3D simulation

The initial temperature of the fluid in the secondary side is 300 K. On the upper portion of the cooling fluid, a thin layer of air is introduced to incorporate free surface effects on the liquid.

The simulation configuration precisely replicates the simulation setup employed within the context of the Inhomogeneous Eulerian framework with Lee model presented in section 5.3.2 . The rationale for adopting the present simulation setup over preceding models lies in its capacity to

offer an acceptable level of accuracy in predicting the thermal-hydraulic behavior of the fluid within the 2D simulation, while concurrently maintaining computational efficiency within reasonable bounds.

The calculated temperature distribution of the secondary side on a cross-sectional plane perpendicular to the U-shaped tube can be seen in Figure 5-40. This figure shows relatively uniform temperature distribution in the secondary side. However, there is a slight non-uniform behavior in the area close to the edge of U part of the tube.

To illustrate the natural circulation of the fluid resulting from the heat transfer process, the velocity contours of the fluid on the same cross-sectional plane perpendicular to the U-shaped tube are presented in Figure 5-41. As depicted in this figure, the fluid's velocity is higher in areas close to the upper surface of the heated tube. It demonstrates that the fluid circulating on the upper part of

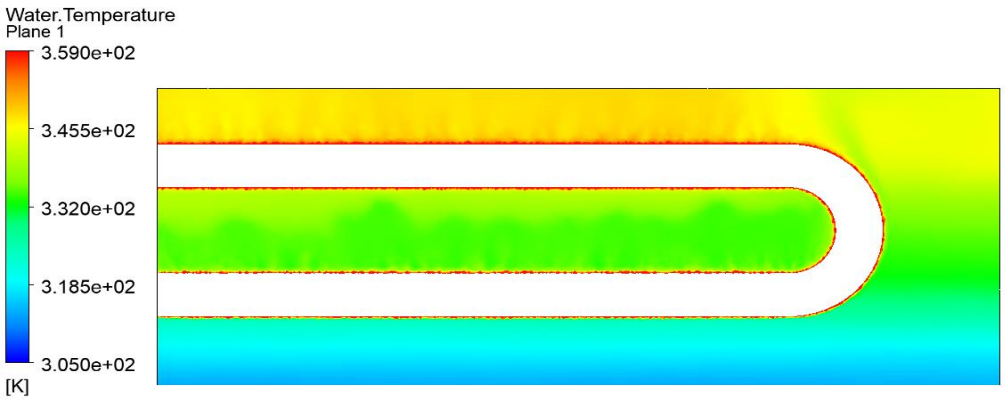

Figure 5-40. Temperature distribution of the secondary side on a cross-sectional plane perpendicular to the U-shaped tube at t = 1400 s

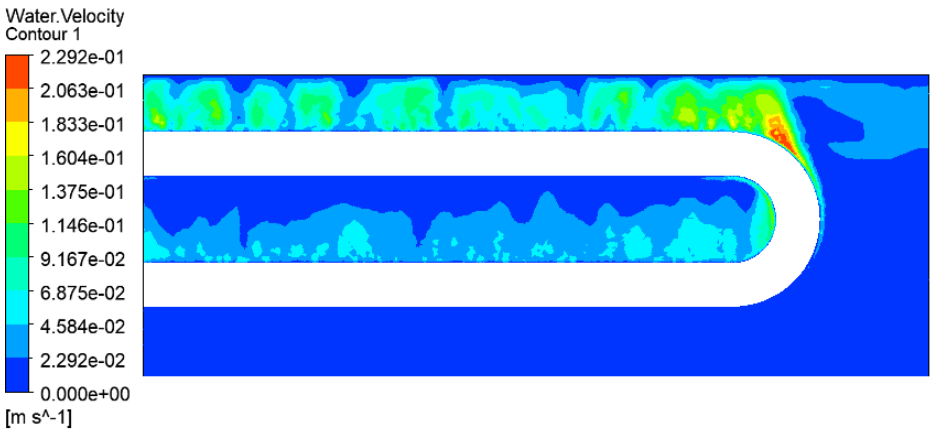

Figure 5-41. Velocity magnitude of water in the secondary side at t=1400 s

a cylindrical geometry maintains a higher velocity compared to the bottom part of the tubes, despite an equally applied temperature boundary condition for all angular positions.

Investigating liquid volume fraction also reveals that gas formation is much more pronounced in the upper section of the tube (see Figure 5-42) as well as the results observed in 2D CFD simulations.

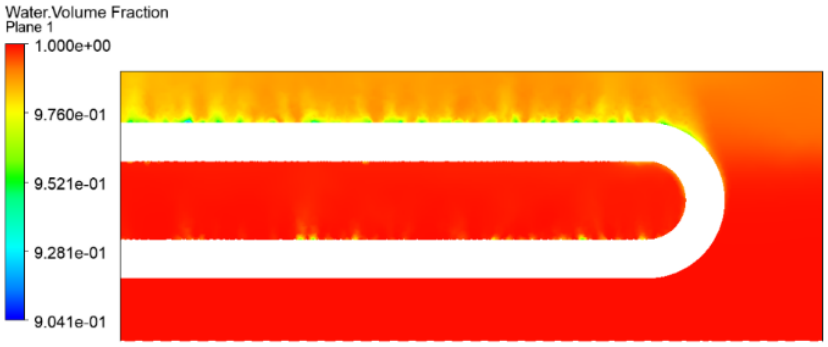

Figure 5-42. Volume fraction of liquid water along the length of the tubes at t=1400 s

5.4.1 Energy balance evaluation for 3D CFD simulation

In this section, similar to the CFD simulations conducted in 2D, a thorough examination of energy balance pertaining to 3D CFD simulations has been undertaken. For this aim, the transient total heat flux transference from the primary side to the secondary side has been derived from CFD

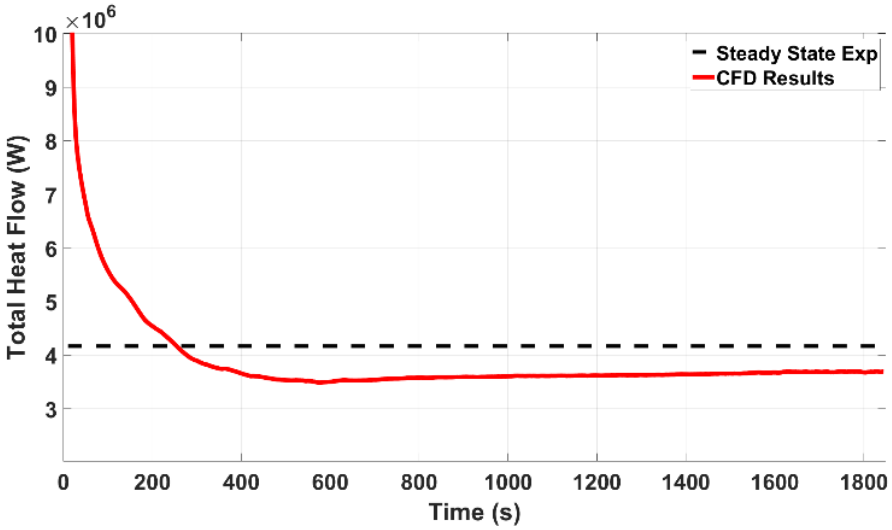

Figure 5-43. Total heat flow from primary side to the secondary side

codes. The resulting data is presented in Figure 5-43 where it is compared with the total steady-state heat flow obtained through experimental data.

As it can be seen in Figure 5-43, the steady state condition is reached relatively quick in this simulation due to steady state boundary conditions. Nevertheless, a temporal interval of approximately 300 seconds is required for the convergence of results. Subsequent to convergence, the discrepancy between computational outcomes and experimental data is approximately 13.37%. This discrepancy underscores a good agreement between the CFD calculations and experimental observations.

5.5. Conclusion

In this chapter, Computational Fluid Dynamics (CFD) simulations have been conducted to analyze the secondary side of the designated test facilities, namely NOKO and COSMEA. Specifically, a single-phase CFD simulation has been performed to model the cooling process occurring in the secondary side of COSMEA. The simulation results depict the temperature distribution of the circulating water within the secondary side, revealing a noteworthy concordance with experimental data. Notably, the simulation showcases commendable accuracy in the computation of the heat transfer coefficient within this specific section. This outcome addresses a key research question pertaining to the optimal numerical approach for this particular application.

It is pertinent to highlight that the computational costs associated with conducting this simulation are relatively low. This attribute enhances the practical feasibility of utilizing CFD simulations for investigating the thermal-hydraulic behavior of the secondary side in COSMEA. As a result, the cost-effectiveness and accuracy of this simulation approach render it a favorable choice for examining the thermal characteristics of the secondary side in the COSMEA system.

Conversely, diverse CFD simulation methodologies have been employed to emulate the secondary side of the NOKO test facility, commencing with single-phase CFD computations. Due to the intricate nature of phenomena occurring in this domain, particularly evaporation-condensation processes, a pronounced incongruity has been identified between the outcomes of single-phase CFD simulations and the experimental data obtained from the NOKO facility. Consequently, the complexity of the CFD simulations has been incrementally heightened in a sequential manner,

aiming first to enhance system accuracy and subsequently to maintain computational costs within an affordable range.

Initially, the utilization of a mixture model marked the initiation of the multi-phase CFD simulation approach. Nevertheless, a substantial discord between the calculations employing this method and the experimental data underscored its inefficacy in predicting the thermal-hydraulic behavior of the system. Subsequently, the Inhomogeneous Eulerian method was considered as the most efficacious model to replicate such intricate processes. The simulation within this framework, incorporating an Evaporation-Condensation model named Lee, exhibited a notable enhancement in CFD calculations, demonstrating a closer alignment with experimental data.

Advancing one step further, the incorporation of the RPI wall boiling model within the Inhomogeneous Eulerian framework was undertaken. Contrary to expectations, this worsened disparities in results and increased computational costs. Consequently, for accurately modeling the thermal-hydraulic behavior of the NOKO secondary side, the simulation within the Inhomogeneous Eulerian framework utilizing the Lee model yielded the most favorable outcomes. However, the substantial computational resources necessitated by this approach prompt further exploration of alternative methodologies or approaches to predict the system's behavior under diverse operating conditions.

6 Heat Transfer Model Development for NOKO secondary side

While CFD simulations provide valuable insights into the thermal-hydraulic features of fluids, the substantial computational requirements associated with these methods have driven the exploration of analytical substitutes for assessing heat transfer performance on the secondary side. On the other hand, in chapter 4, it was shown that heat transfer models sourced from existing literature which were applicable in this heat exchanger failed to compute the heat transfer coefficient on the secondary side of NOKO test facility. The observed disparity between the computed outcomes from classical heat transfer models and the empirical data obtained from the NOKO facility underscores the imperative to develop an enhanced correlation. Such a correlation is essential for accurately predicting the heat transfer performance of the respective heat exchangers, addressing the existing discrepancy and improving the fidelity of the predictive models.

To achieve the stated objective, the initial phase involves the identification of factors influencing the heat transfer performance in nucleate pool boiling within a large volume. The Prandtl number (*Pr*) emerges as a critical variable in natural circulations, predicated upon the thermodynamic characteristics of the fluid under consideration. Notably, among various nucleate heat transfer models, the Labuntsov model [22] exhibits the minimal deviation when compared to experimental data, underscoring its efficacy. Upon closer examination of the Labuntsov model, it becomes apparent that, in addition to the *Pr* number, an additional term is present to calculate *Nu* number in the heating up process. This term is dependent upon various thermodynamic properties of the fluid, including thermal conductivity, temperature differential from the saturation temperature, and other relevant parameters. Consequently, a reformulated correlation to calculate *Nu* number in this

case is proposed, incorporating both the *Pr* and this additional term denoted as '*G*' in this study, as expressed in the following equation:

$$Nu = f(Pr, G) \quad 6\text{-}1$$

$$\mathrm{G} = \frac{\lambda \Delta \mathrm{T}}{\mathrm{r}\, \rho_{\mathrm{st}} \mathrm{v}} \quad 6\text{-}2$$

In Equation 6-2, λ is thermal conductivity of the fluid, r is specific heat of vaporization, ρ_{st} is the density of gas phase, v is kinematic viscosity and ΔT is temperature difference between fluid and saturation temperature.

Among the diverse modifications to heat transfer correlations, a preference is given to non-linear configurations akin to the Labuntsov model. The objective herein is to refine the Labuntsov model by adjusting three key constant parameters—designated as C, γ, and β in Equation 6-3—with the aim of augmenting its predictive accuracy.

$$Nu = C.Pr^{\gamma}.G^{\beta} \quad 6\text{-}3$$

This approach aims to enhance the predictive accuracy of the heat transfer performance in nucleate pool boiling within large volumes, recognizing the multifaceted influence of the fluid's thermodynamic properties on the process.

In MATLAB, a non-linear regression method can be employed to adjust parameters in a correlation model based on experimental data. In Equation 6-3, *Nu* is calculated from experiments, and *Pr* and *G* are derived from the thermodynamic characteristics of the process. To adjust the parameters C,

γ, and β, a non-linear regression approach, such as the trust-region reflective algorithm in MATLAB, can be utilized.

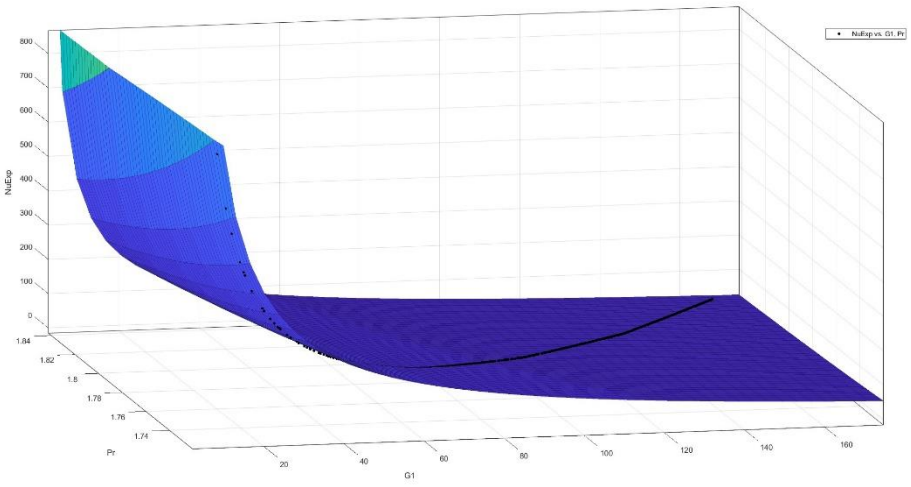

Figure 6-1.3D regression analyses of nucleate pool boiling

The training process involves organizing the experimental data and determining the appropriate independent variables (*Pr* and *G* in this case). The objective is to find the optimal values for C, γ, and β that minimize the difference between the calculated *Nu* values using the correlation model and the actual *Nu* values obtained from experiments. This method takes the correlation model, initial parameter guesses, and experimental data as inputs, optimizing the parameters iteratively until a satisfactory fit is achieved. This nonlinear optimization approach enables the adjustment of C, γ, and β, ensuring that the correlation model accurately captures the relationship between *Nu*, *Pr*, and *G* based on experimental observations. The refined parameters can then be extracted and used to update the correlation model for improved predictive accuracy.

Figure 6-1, presents the outcomes of the regression analysis applied to nucleate pool boiling, wherein the dependent variable, Nu_{exp} , is directly derived from experimental observations. The independent variables, *Pr* and *G*, are computed based on the operating conditions specific to the NOKO test facility. Nu_{exp} is a key parameter in the context of nucleate pool boiling. The utilization of regression analysis in this investigation enables the examination and quantification of the interdependence between Nu_{exp}, *Pr*, and *G*, facilitating a comprehensive understanding of the heat transfer characteristics within the nucleate pool boiling regime. The computed values of *Pr* and *G*,

reflective of the thermodynamic conditions in the NOKO test facility, contribute to the establishment of a robust regression model, enhancing the predictive capability of the correlation between $Nu_{exp,}$ Pr, and G in the studied boiling system.

The refined correlation, derived from the analysis and featuring adjusted constants, is presented in the subsequent section:

$$Nu = C.Pr^{\alpha}.G^{\beta} \qquad 6\text{-}4$$
$$C = 2.599 \times 10^{6}$$
$$\alpha = -0.9624$$
$$\beta = -10.72$$

In the regression analysis for the investigation of the relationship between Nu_{exp} and Pr and G, insightful results on the goodness of fit have been achieved. The estimated coefficients, accompanied by their 95% confidence bounds, revealed significant associations. The model demonstrated a robust fit as evidenced by key metrics: A Sum of Squared Errors (SSE) of 1.202e+05, an impressive R-square (R^2) of 0.9722, an Adjusted R-square of 0.9722, and a Root Mean Square Error (RMSE) of 5.199. Notably, the high R-square value suggests the model explains a substantial proportion of the variance in the dependent variable, and the low RMSE underscores the accuracy of the predictions.

As mentioned earlier, NOKO experiments have been conducted across four distinct operational conditions, as presented in Table 3-2. The regression analysis incorporated data derived from three of these conditions (Experiments No. 10, 30 and 50 bar), reserving one dataset (Experiment No.65 bar) for the purpose of evaluating the modified correlation. This deliberate partitioning ensures

rigorous evaluation of the performance of adjusted constants across a spectrum of scenarios, thereby enhancing the comprehensiveness and robustness of the assessment.

6.1. Evaluation of refined model

To assess the adequacy of the proposed correlation, the computed Heat Transfer Coefficient (HTC) values employing the newly introduced correlation were compared with the corresponding experimental HTC data and HTC values derived from preceding models for nucleate pool boiling, specifically under transient conditions. This comparative analysis serves as a critical examination of the proposed correlation's efficacy by evaluating its performance against established

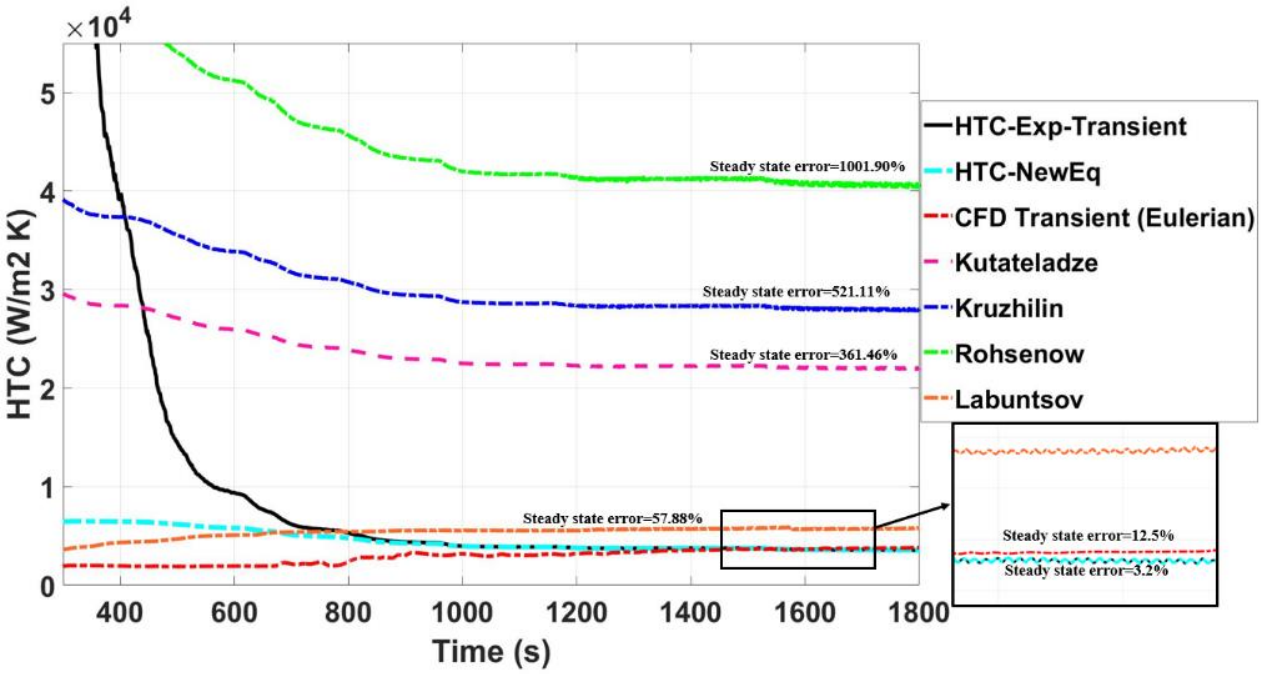

Figure 6-2. Evaluation of the proposed correlation against experimental data, CFD calculations and empirical nucleate pool boiling models

benchmarks and previous theoretical frameworks in capturing the dynamic nuances of nucleate pool boiling. Figure 6-2 shows the results of this comparison.

The experimental HTC is calculated using Equation 5-30 and the conduction equation for the surface of the tubes using transient temperatures and thermodynamic properties. This is the reason of high values of HTC in the beginning of the process. This should not be considered in the evaluation due to the explanation given in section 5.3.6 for the transient heat flux. However, after passing this transient condition, the figure illustrates, a notable alignment between the proposed correlation and experimental data, particularly evident after t=700 s, showcasing substantial improvements compared to widely employed nucleate pool boiling models. The significant deviation observed in the initial phase of the proposed correlation can be primarily attributed to the commencement of the heating-up process, where the dominant heat transfer mechanism is single-phase natural convection, in contrast to the models developed for nucleate pool boiling. Therefore, their accuracy is enhanced post the initiation of boiling on the secondary side, a phenomenon occurring later in the heating process. Furthermore, the calculated HTC via CFD simulation in an inhomogeneous framework is presented in this section to highlight the proximity

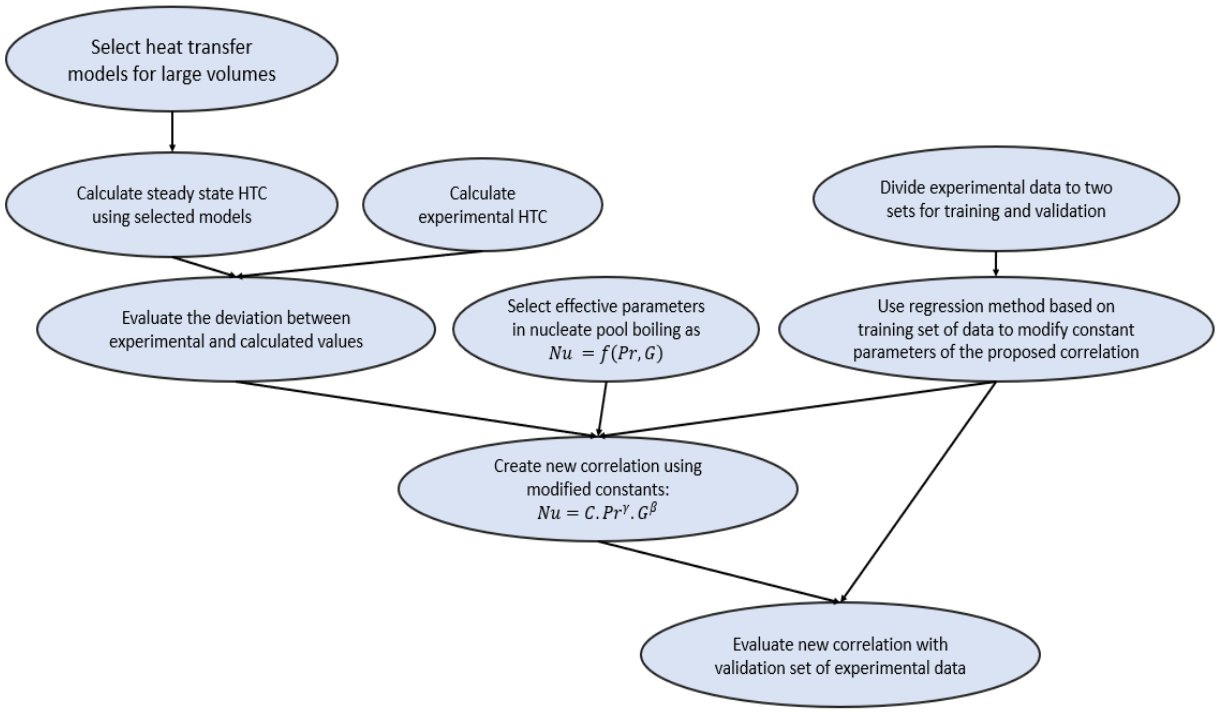

Figure 6-3. Summary of procedure done for heat transfer model developement for nucleate pool boiling

of the calculated HTC via the proposed new correlation to experiments and CFD results obtained in the previous section. Thus, this model offers a reliable, cost-effective, and practical methodology for computing nucleate pool boiling heat transfer coefficients in emergency condensers. A summary of the process done in this section to obtained the new developed heat transfer model for nucleate pool boiling in passive heat removal systems is shown in Figure 6-3.

6.2. Conclusion

This chapter presents an effort to formulate a heat transfer model for the computation of the heat transfer coefficient on the secondary side. The motivation behind this endeavor is the mitigation of extensive computational expenses associated with CFD calculations. Following an evaluation of existing heat transfer models in the literature, the Labuntsov model was selected for refinement. Utilizing the regression method in MATLAB, the constant parameters of the Labuntsov model were adjusted to minimize deviation based on experimental data from the NOKO facility. The refined model demonstrated favorable agreement in predicting the heat transfer coefficient on the secondary side within the NOKO test facility.

This approach offers a cost-effective means to estimate the heat removal capacity of the secondary side and is compatible with 1D simulation software employed in nuclear power plants, such as ATHLET or RELAP. Addressing another research question, this chapter explores the potential development of an empirical heat transfer model for calculating the performance of passive heat removal systems.

While the proposed model exhibits accuracy in predicting the heat transfer coefficient of the adjacent fluid on the secondary side, it is important to note that an in-depth examination of the thermal-hydraulic behavior of the fluid in a larger region within the confined volume of coolant, distant from heated surfaces, including aspects like temperature distribution and velocity development, necessitates comprehensive CFD simulations. Nevertheless, it raises a question regarding the feasibility of employing a data-driven analysis to investigate the potential for predicting the thermal-hydraulic behavior of the fluid in regions more distant from heated tubes within expansive pools, while minimizing computational expenses.

7 Artificial Neural Network Model Development for Temperature Distribution in NOKO secondary side

The heat transfer model developed in the preceding chapter provides an accurate prediction of the heat transfer coefficient on the secondary side in close proximity to the fluid adjacent to the heated tube surface. Nevertheless, it fails to offer a cost-effective prediction for the fluid situated farther away from the heated surfaces. Particularly, the intricate temperature rise pattern within different regions of the secondary side cannot be adequately captured by any specific empirical correlations. This phenomenon can be relatively accurately predicted through multiphase CFD simulations, which offer a comprehensive understanding of the physical processes occurring on the secondary side. However, the prohibitive computational costs associated with these CFD methods prompt the exploration of alternative, more cost-effective approaches to predict the temperature behavior.

As previously mentioned, a significant challenge in modeling the temperature distribution on the secondary side is linked to the regions at the bottom of the pool, where a sudden temperature increase occurs (refer to Figure 3-7). This occurrence is not exclusive to NOKO experiments; other passive heat exchangers also grapple with this phenomenon, presenting a formidable challenge in modeling the thermal-hydraulic behavior of the system. For instance, this phenomenon has been observed in experiments involving C-shape heating rods submerged in cooling water within a passive residual heat removal heat exchanger (PRHR HX)[32]. Another example of this phenomenon's observation is associated with experiments conducted on the Integral Test Loop (ITL), a scaled test facility designed for investigating the thermal stratification phenomenon in an advanced heavy water reactor (AHWR). The sudden temperature jump in the lower regions of the extensive volume of cooling fluid has been documented in experiments related to the isolation condenser (IC) system[66]. Furthermore, at HZDR, a small-scale test facility has been developed to observe thermal stratification in a cylindrical pool when the wall of the pool is uniformly heated. Similar to other observations, a sudden temperature increase (temperature jump) has been observed in this experimental data [41].

In this section, a neural network model is formulated to forecast the transient temperature distribution on the secondary side at various thermocouple locations within the NOKO test facility,

contingent upon the operational parameters of the primary side. The efficiency of the developed model, which exhibits notable accuracy in predicting the thermal-hydraulic behavior of the secondary side when compared to NOKO experimental data, underscores the potential applicability of this approach in diverse passive heat removal systems employing substantial coolant volumes. This utilization serves to avoid the formidable computational expenses associated with CFD simulations.

7.1. ANN model development

Artificial Neural Networks (ANNs), with their adept learning capabilities, exhibit enhanced predictive efficacy in contrast to traditional mathematical methodologies. Effectively tuning the hyperparameters of ANNs can mitigate challenges associated with resource-intensive CPU time and memory consumption [67]. Different ANN models have been developed to serve diverse purposes, yet they adhere to a uniform algorithmic structure for modeling input-to-output relationships. Key parameters influencing ANN performance include the configuration of hidden layers, input and target layers, selection of transfer functions, learning algorithms, momentum factors, and learning rates. The importance of thoughtful data selection cannot be overstated, as it significantly impacts the efficacy of the ANN model. This case study focuses on evaluating the experimental data of NOKO, considering data variants, patterns, coverage of operating scenarios, and data distribution to ascertain the efficiency of the dataset for ANN model development. This comprehensive evaluation serves as the basis for determining the suitability of the dataset for developing an ANN model. The initial step in training an ANN involves the preparation of input-output data. Subsequently, an appropriate learning method is employed to establish the relationship between input and output data. The NOKO experimental data is found to be sufficiently robust for developing an ANN model, considering its diverse variants, patterns, coverage of operating scenarios, and well-distributed data. The training process involves iteratively adjusting the parameters of the ANN until the network output aligns with the desired outputs (targets) established as the required dataset for the model. This study underscores the significance of parameter selection and data quality in the development and training of ANN models. The NOKO experimental data, having undergone a thorough evaluation, emerges as a suitable candidate for constructing an ANN model. The training process involves a meticulous alignment of network parameters until the desired output is achieved, paving the way for the effective representation of

complex relationships within the data [68, 69]. Figure 7-1, shows the flow chart of the training process with an ANN network. This systematic approach contributes to the advancement of ANN methodologies, with potential applications in various fields.

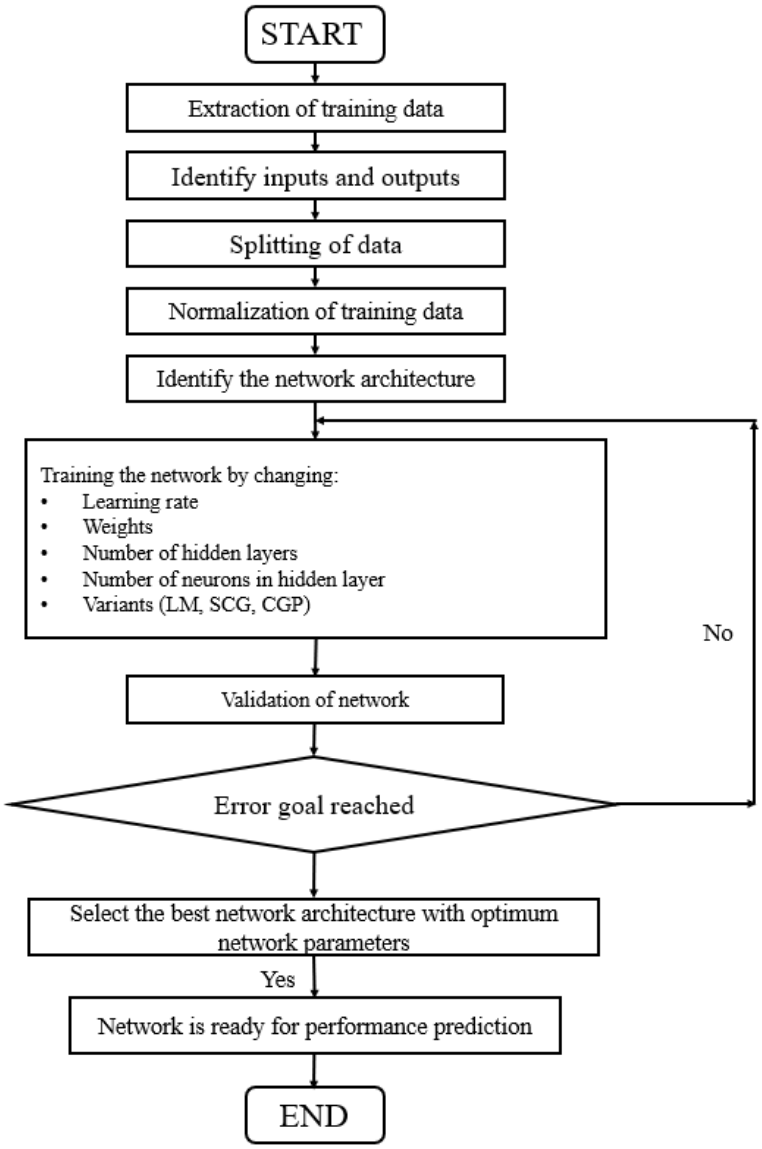

Figure 7-1. ANN training process [68]

In this section, an ANN model utilizing the multilayer perceptron (MLP) architecture is constructed to forecast the temperature distribution across various locations on the secondary side. The utilization of MLP

is motivated by its robust learning proficiency and structural attributes, allowing for the modeling of intricate processes without excessive computational resource utilization [70].

MLP model functions as a feedforward neural network (FFNN), serving the purpose of delineating intricate connections among variables and forecasting forthcoming values in a given process. As it can be seen in Figure 7-2, it consists of layers, including input, hidden, and output layers, with computational units linked to layer nodes through weight coefficients and governed by activation functions.

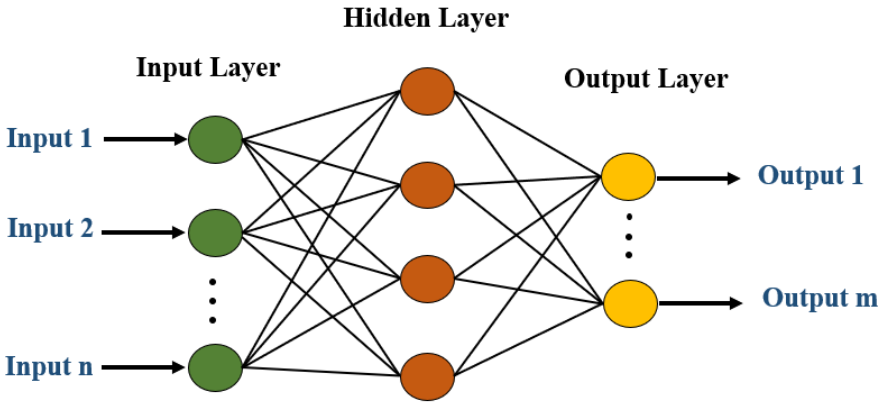

Figure 7-2. Stracture of ANN model with MLP architecture

While MLP generally allows for the incorporation of one or more hidden layers, it's noteworthy that, in many scenarios, a single hidden layer might be ample to achieve an acceptable level of accuracy [71]. However, the important factor to reach a good accuracy in MLP model is the number of neurons in hidden layer. In this model, Azoff formula is used to define the number of neurons in the hidden layer based on the number of inputs as follows [72]:

$$N_h = 2 \times N_u + 1 \qquad 7\text{-}1$$

Where, N_h is the number of neurons in hidden layer and N_u is the number of inputs.

Utilizing the second-order derivative-based Levenberg–Marquardt (LM) method, the adjustment of model parameters was executed. This algorithm is widely employed for training parameters in moderate-sized MLPs. The training process employed the mean square of error (MSE) as the objective function.

$$e = \frac{1}{p}\sum_{i=1}^{p}(y_i^* - y_i)^2 \qquad 7\text{-}2$$

Where, y_i^* is the target output and y_i is the real output of the data set. p is the total number of training set of the data.

As other ANN models, in Multilayer Perceptron (MLP) networks, data moves from the input layer to the hidden layer and finally to the output layer. The model calculates the difference between predicted and target values. This difference is used to adjust the model, minimizing errors. The training phase aims to achieve the lowest error value, indicating optimal learning. After training, it's essential to verify its success. This phase is called validation phase. A separate dataset is used to assess the model's reliability, ensuring it has learned effectively. In this model, 15% of the total samples are used as validation date set. Confirming ideal completion helps ensure the model is ready for broader application. Then it comes to testing phase. This phase assesses how well the model performs on new, unseen data. A separate test dataset (15% of total data set), distinct from the training and validation sets, is employed. The goal is to understand how closely the model's outputs align with real values. Successful testing suggests the model is robust and reliable for various scenarios.

In this model, the dataset of 9400 samples are originated from Experiments No. 10bar, 50bar and 65bar acquired from the NOKO test facility (see Table 3-2). The dataset encompasses five input parameters designed to characterize the operational conditions of the primary side. These inputs include temporal information, primary side operating pressure, inlet mass flow rate, as well as the inlet and outlet temperatures of the fluid in the primary side. The model's outputs are represented by the temperatures recorded by thermocouples positioned at the bottom, middle, and upper sections of the secondary side. Specifically, these temperatures correspond to the thermocouples identified as TI3-D02, TI3-D03, and TI3-D05 which address the general pattern of temperature changes in top, middle and bottom of the tank, respectively. It is noteworthy that a subset of

experimental data corresponding to experiment No.30 bar is reserved for subsequent validation of the developed Artificial Neural Network (ANN).

The proposed model employs a consistent ANN architecture across multiple measuring planes, resulting in a comprehensive structure comprising eight distinct MLP networks. Despite sharing the same input data, each MLP network yields different outputs corresponding to the characteristics of individual measuring planes. This division of the networks based on the outputs related to each measuring plane helps to increase the accuracy of each network in predicting the temperature of different locations. Consequently, the overall accuracy of the model is enhanced, providing a more robust prediction of the temperature distribution in the 3D configuration of the secondary side.

To illustrate the overall structure of the model, refer to Figure 7-3. This configuration, characterized by its uniform input but different outputs, facilitates the prediction of temperature distribution in the 3D configuration of the secondary side.

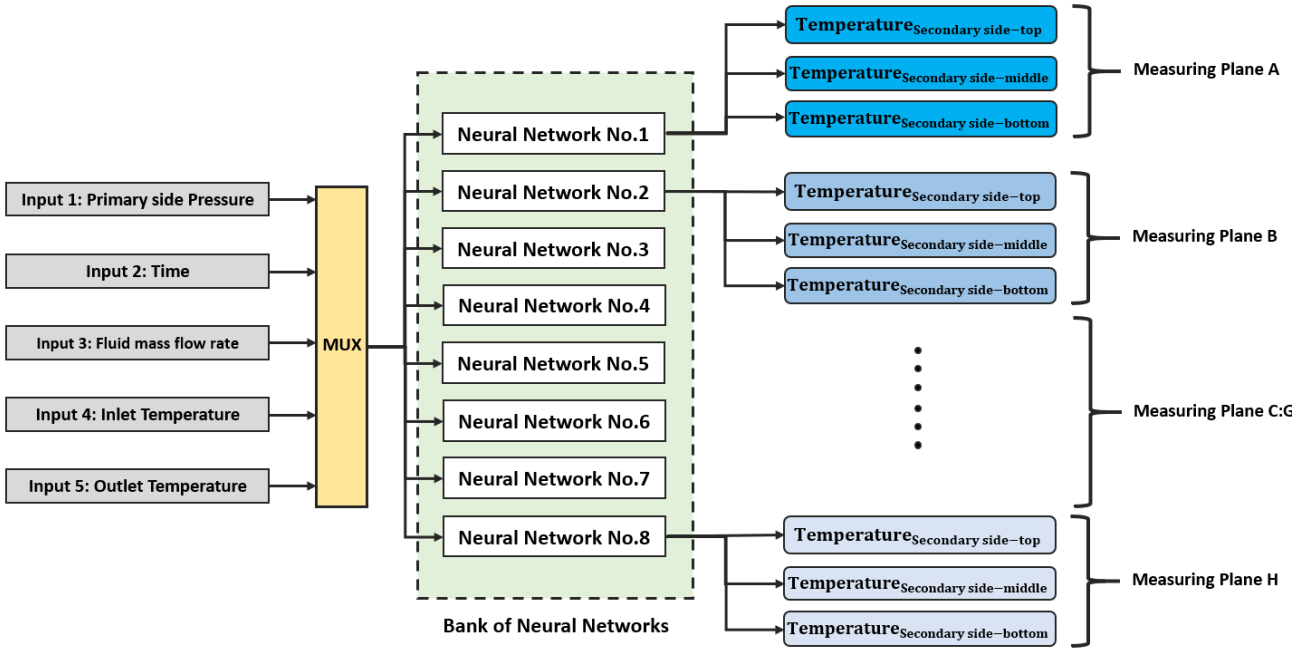

Figure 7-3. Structure of proposed neural network model

7.2. Results and validation of developed ANN

The results obtained from each developed artificial neural network (ANN) model demonstrate the efficacy of the selected network architecture in accurately modeling the provided data. The

regression curves depicting the training, validation, and testing datasets for one ANN model associated with measuring plane D are presented in Figure 7-4. In this graphical representation, the output corresponds to the values predicted by the trained neural network, while the target represents the actual data utilized during the training process. The paramount metric for assessing the trained model is the correlation coefficient (R), denoting the degree of concordance between predicted and actual values. R values approaching 1 signify a robust positive correlation between these two parameters.

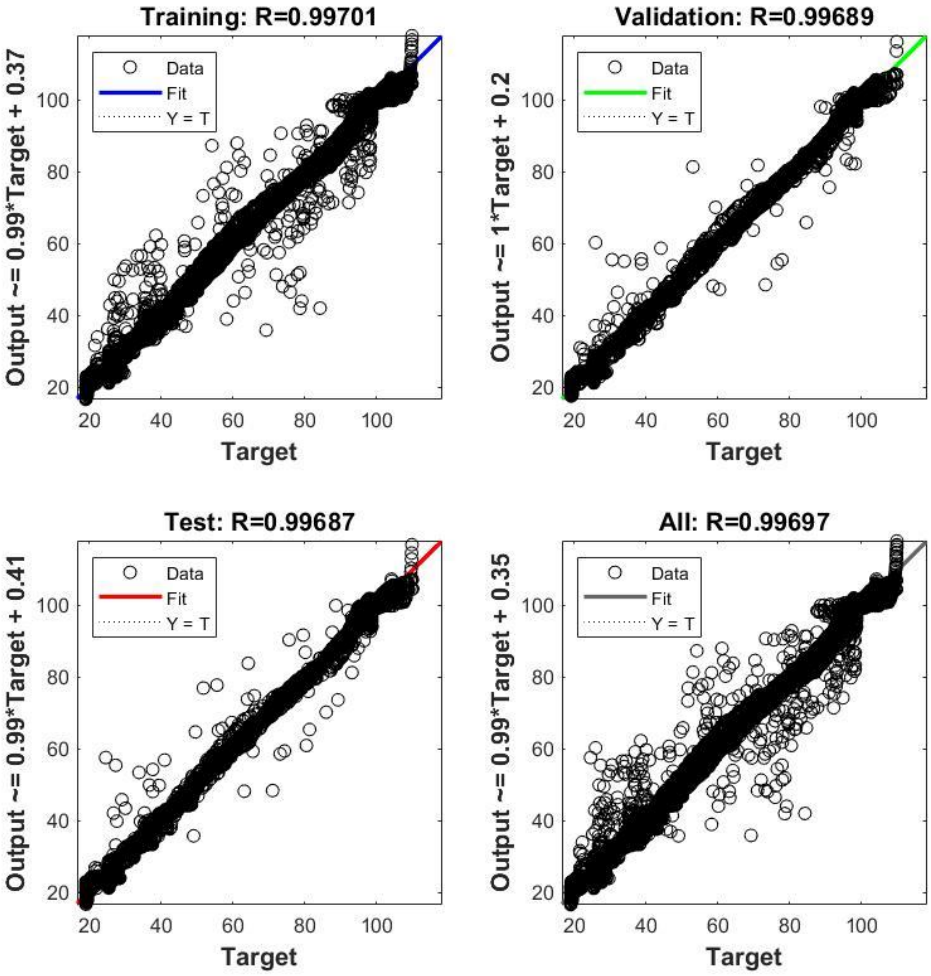

Figure 7-4. Regression results for ANN model od measuring plane D

Moreover, the performance graph of the established ANN model in the current investigation is delineated in Figure 7-5. Within this graphical depiction, the Mean Square Error (MSE) values

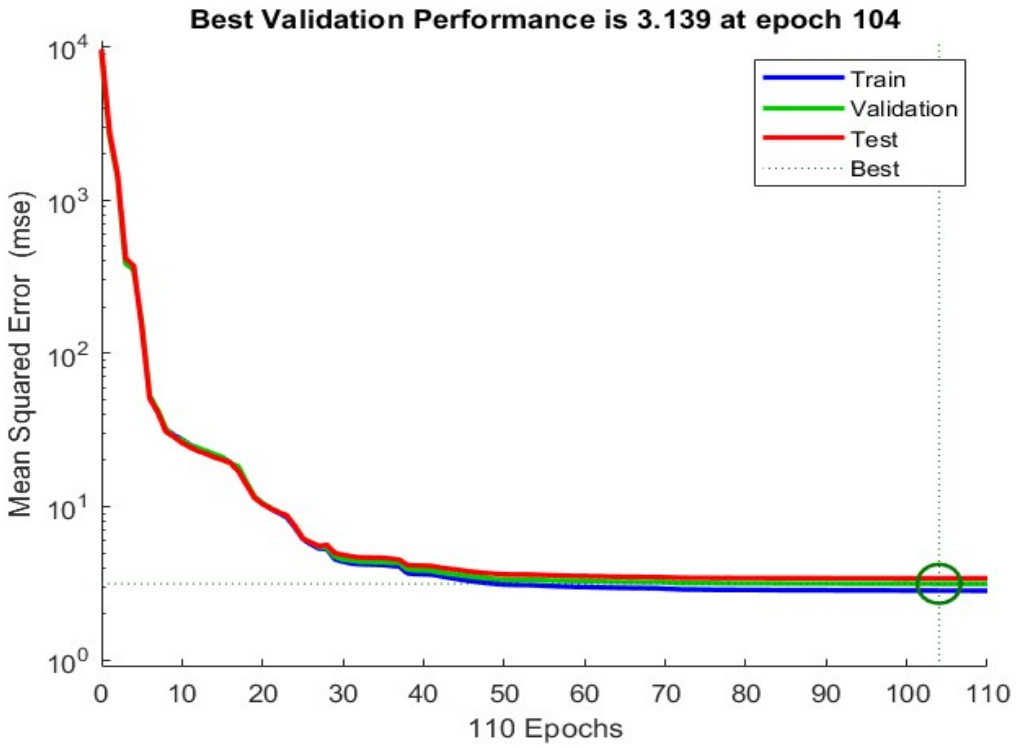

Figure 7-5. Performance graph of ANN model for measuring plane D

across each epoch during the entirety of the training phases are illustrated. An epoch denotes a complete iteration through the dataset, during which the network processes each input, computes the corresponding output, compares it with the target output, and adjusts the network weights through backpropagation to minimize the error. Hence, the MSE values start from higher values and progressively decrease over successive epochs. In this particular model, the minimum MSE value is attained after 104 epochs, indicating optimal performance. At this juncture, the training of the ANN model is considered complete. Following the satisfactory completion of training, validation, and testing phases, the model undergoes optimization. The optimized ANN is subsequently prepared for implementation, enabling the generation of predictive values for new

data. The identical procedure is iteratively applied to each measuring plane resulting a set of 8 ANN models.

Table 7-1 provides a detailed summary of the results obtained from each ANN model corresponding to measuring planes A to H.

Table 7-1. Performance of each developed ANN model

	ANN model	ANN A	ANN B	ANN C	ANN D	ANN E	ANN F	ANN G	ANN H
R	Train	0.9984	0.9985	0.9986	0.99701	0.9986	0.9983	0.9987	0.9997
	Validation	0.9982	0.9988	0.9985	0.99689	0.9989	0.9988	0.9986	0.9997
	Test	0.9984	0.9987	0.9988	0.99687	0.9983	0.9985	0.9988	0.9997
MSE	Train	2.7969	2.6296	2.4307	2.8324	2.5064	2.1828	1.9547	0.3745
	Validation	3.3191	2.0575	2.5822	3.1390	1.8658	2.1828	1.9119	0.3841
	Test	2.9631	2.3723	2.1387	3.4076	3.0870	2.6615	1.9002	0.3835

In the context of implementing the Artificial Neural Network (ANN) model, the dataset corresponding to experiment No. 30bar is employed for analysis. The results could predict the temperature distribution of the secondary side in the three distinct locations (top, middle and bottom) of the tank for all 8 measuring planes. The ensuing predicted outcomes for measuring plane D, suited midway along the tank's length, are visually represented in Figure 7-6 .Notably,

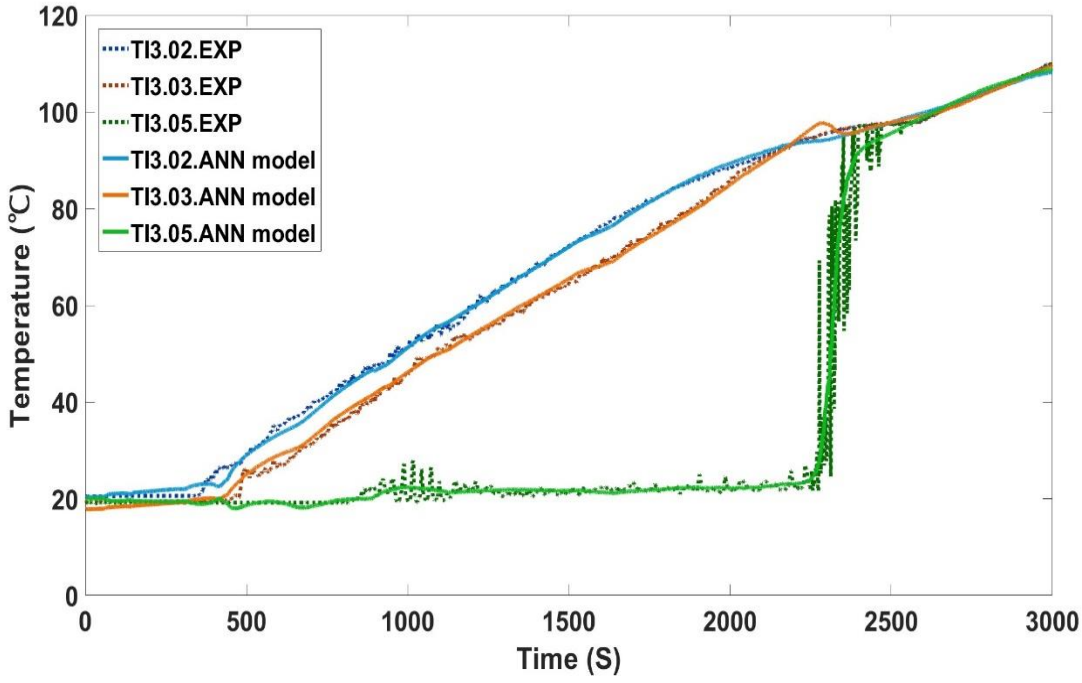

Figure 7-6. Evaluation of developed ANN model for measuring plane D with seperate data of experiment No. 30 bar

the depicted figure illustrates the successful anticipation of a sudden temperature escalation in the lower region of the secondary side as well as the uniform temperature increase in other locations by the ANN model. This outcome demonstrates a strong agreement with the experimental data, highlighting the design network's excellent capability to accurately predict the transient temperature distribution in large pools of passive heat removal systems during the heating-up process.

While the temperature increases trends across various measuring planes exhibit a consistent pattern, slight variations emerge in the results recorded by thermocouples on measuring plane H, positioned outside the heated tube bundles within the tank. Figure 7-7 illustrates the prediction outcomes of the developed ANN model for this plane, compared with experimental data No.30 bar. Once more, the notable agreement between the predicted results and experimental data serves as further evidence affirming the adequacy of MLP neural networks for predicting temperature distribution in passive heat removal systems.

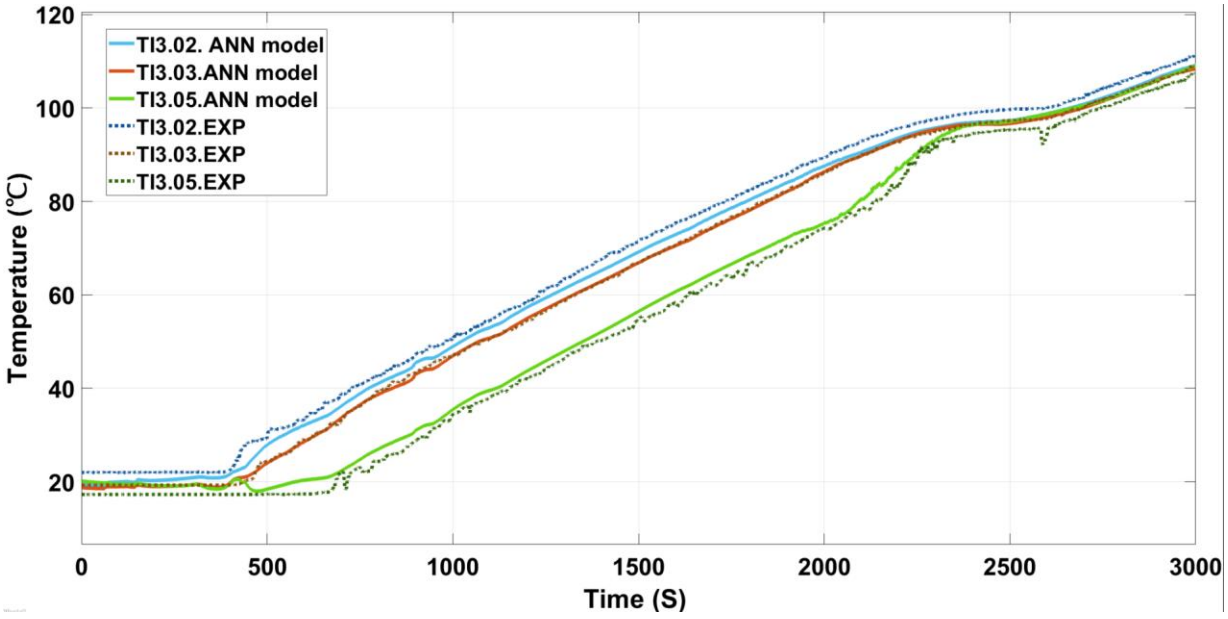

Figure 7-7. Evaluation of developed ANN model for measuring plane H with seperate data of experiment No. 30 bar

The outcomes derived from this developed ANN architecture offer a viable alternative for real-time prediction of temperature distribution across various passive heat exchangers. By inputting

sensor data into this model, the thermal-hydraulic behavior of the fluid can be accurately forecasted at different locations. Furthermore, it enables preventive measures to be taken to mitigate any undesirable temperature spikes or unexpected thermal-hydraulic behaviors before they occur.

The proposed model has been implemented in Simulink MATLAB (refer to Figure 7-8). This implementation serves as a crucial step toward its industrial application, enabling real-time prediction of temperature distribution or any critical variables. Beyond emergency condensers, this approach is applicable to various passive heat removal systems featuring large volume pools, offering broader utility in industrial settings.

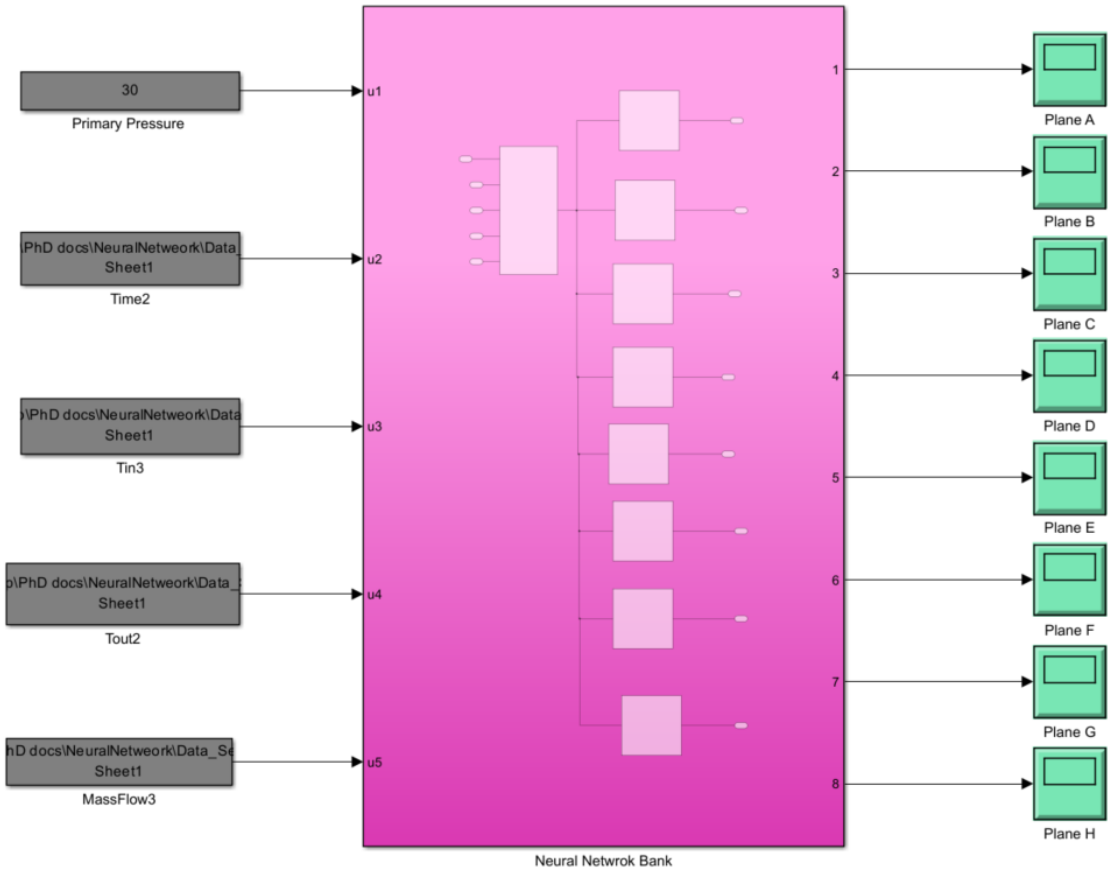

Figure 7-8. Simulink implementation of proposed ANN for real time predictions

7.3. Conclusion

In this chapter, a data-driven methodology was employed to elucidate the behavioral dynamics of the NOKO secondary side in a cost-effective manner. The approach employs a series of artificial

neural network (ANN) models, specifically multi-layer perceptron (MLP) architectures, to forecast the transient temperature profiles at various elevations within the tank – specifically, the top, middle, and bottom areas. These ANNs are developed for eight measuring planes strategically positioned along the length of the secondary side.

The resulting set of ANN models successfully yields a comprehensive 3D temperature distribution along the length of the secondary side across eight distinct cross-sectional areas corresponding to each measuring plane. Through rigorous training and validation, the ANN models exhibit a favorable agreement with experimental data, indicating their efficacy in capturing the dynamic thermal behavior of the system.

This innovative approach provides a valuable alternative for predicting the thermal-hydraulic characteristics of large pools without resorting to computationally intensive computational fluid dynamics (CFD) calculations. While CFD simulations offer more physically accurate and detailed insights into the process, the proposed methodology offers a cost-effective solution with relatively accurate predictions. By circumventing the need for expensive computational efforts, this approach stands as a practical and efficient tool for assessing the thermal behavior of fluids in large-scale passive heat removal systems.

8 Conclusion and Outlook

8.1. conclusion

The primary objective of this thesis was to enhance the comprehension of the heat transfer mechanisms inherent in passive safety systems, with the overarching goal of establishing a foundational understanding for the optimization of their performance and the augmentation of their efficiency. This pursuit is integral to the overall safety enhancement of nuclear power plants.

The focal point of this investigation primarily centered on elucidating the role of emergency condensers (EC) within passive safety systems. This emphasis was directed towards augmenting existing studies pertaining to the primary aspects of such systems. To achieve this objective, the initial step involved the selection of appropriate test facilities to serve as a validation base for the study. Subsequently, an evaluation of the state-of-the-art heat transfer models prevalent in the literature was conducted, with a focus on assessing their efficacy in predicting the performance of passive safety systems.

The assessment specifically targeted the secondary side of the designated test facilities, namely COSMEA and NOKO. The outcomes of this evaluation revealed a substantial incongruity between the calculated results derived from empirical and semi-empirical models in comparison to the experimental results obtained from the secondary side of COSMEA and NOKO. This dissonance served as the impetus for subsequent steps aimed at delving deeper into the underlying processes within the secondary side, and devising methods to accurately predict the thermal-hydraulic behavior of these systems.

In the context of heat transfer processes within a confined large volume of coolant, the establishment and elimination of temperature stratification play pivotal roles. This phenomenon induces early local evaporation in proximity to heated surfaces, leading to the generation of steam and subsequent distribution within the coolant pool. The dynamics of steam generation profoundly influence the velocity development within the fluid. Notably, the condensed steam reverts to liquid state after sufficient distance is attained from the heat source.

The transient nature of continuous evaporation and condensation results in diverse temperature patterns across distinct regions of the large volume coolant. Over time, a sudden temperature increase occurs in areas closer to the bottom of the tank, which are concurrently farther from the

saturation condition. Additionally, saturation conditions may manifest in upper areas closer to the pool surface, exerting a noticeable impact on the thermodynamic behavior of the system.

To comprehensively model this intricate process, CFD calculations were employed, providing essential insights for research purposes. Initially, a single-phase CFD simulation of the COSMEA secondary side was conducted, representing the first foray into CFD calculations in this study. Despite the dissimilarities between the COSMEA secondary side process and real-scale emergency condensers, these calculations facilitated the evaluation of CFD's capability to determine the heat transfer coefficient, an aspect challenging for other heat transfer models.

Subsequently, CFD calculations for the NOKO secondary side were initiated, starting with a single-phase modeling approach. However, significant disparities between the calculated results and experimental data indicated the inadequacy of single-phase modeling to capture the complexity of the described process. This underscored the imperative need for a multi-phase CFD simulation. In an attempt to manage computational costs, the multi-phase calculations commenced with a simpler modeling approach, namely the mixture model. Nevertheless, the observed deviations necessitated a shift towards a more sophisticated CFD framework, specifically the inhomogeneous Eulerian methods.

Within this framework, two models were employed to incorporate phase change phenomena: the Lee condensation-evaporation model and the RPI wall boiling model. The Lee model demonstrated superior performance in terms of accuracy and stability, albeit at the expense of increased computational costs. The application of inhomogeneous Eulerian methods not only yielded results that aligned more closely with experimental data but also provided detailed insights into the intricacies of the process. These insights surpassed the scope of experimental observations.

While the computational efforts were substantial, they instigated a quest for alternative methodologies to assess system performance. This pursuit aims to balance computational efficiency with the acquisition of accurate and detailed information about the system's operational dynamics.

The investigation subsequently shifted towards an analytical approach, culminating in the development of an empirical correlation aimed at more accurately determining the heat transfer coefficient of the NOKO secondary side. To achieve this objective, a regression method implemented in MATLAB was employed to formulate a correlation capable of precise heat transfer coefficient calculations for the secondary side. This endeavor holds practical significance

in nuclear applications, where the exclusive knowledge of the system's heat transfer performance is paramount.

Concurrently, efforts were directed towards exploring alternative methodologies for predicting the transient temperature distribution of the secondary side. To achieve this objective, an Artificial Neural Network (ANN) was devised utilizing the experimental data obtained from the NOKO test facility. The model was constructed with a foundation rooted in the operational parameters of the primary side, enabling predictions of the transient temperature profiles of the coolant at various locations within the tank, spanning from the bottom to the top. The primary motivation behind employing this modeling approach was to establish a data-driven model capable of forecasting the temperature distribution on the secondary side solely based on the primary side's operational conditions. This approach affords notable cost-effectiveness and expeditious adaptability to modifications.

However, it is essential to acknowledge that the efficacy of this method is contingent upon its alignment with the range of data used for model training. Consequently, for applications characterized by dissimilar operational ranges, the model necessitates re-training with relevant data from the specific application of interest. Despite this limitation, the rapid adaptability and cost-effectiveness inherent in this approach render it well-suited for diverse applications, provided that re-training is undertaken to accommodate the unique operational context of each application.

8.2. Outlook

Prospective investigations should prioritize the application of diverse methodologies expounded in this dissertation to alternative test facilities of passive safety systems, thereby evaluating their generalizability. Of particular interest are passive residual heat removal heat exchangers (PRHR HX), extensively utilized in nuclear contexts, and analogous test facilities such as the Integral Test Loop (ITL), which could serve as pertinent validation platforms for examining and affirming the methodologies delineated in this study—ranging from proposed Computational Fluid Dynamics (CFD) techniques to analytical and data-driven approaches.

An advanced phase of inquiry may involve a deliberate exploration into directions for process optimization, involving modifications to the system's design parameters, including but not limited to its geometric configuration. This investigation aims to discern the potential impact of such

alterations on the thermal-hydraulic and heat transfer performance of the system, with the ultimate goal of enhancing the overall efficiency of passive safety systems.

Appendix:

The detailed correlations of heat transfer models of single-phase natural convection are provided in Table 0-1.

Table 0-1. Summary of natural convection models for horizontal tubes

No.	Author	Main correlations
1	Churchill [26]	$Nu = 0.579\left\{\frac{Ra}{\left[1+(0.442/Pr)^{9/16}\right]^{16/9}}\right\}^{1/4}$, $Gr\,\mathrm{Pr} > 10^{-1}$
2	Churchill and Chu [27]	$Nu = \left\{0.60 + \frac{0.387Ra^{1/6}}{\left[1+(0.559/Pr)^{9/16}\right]^{8/27}}\right\}^2$, $Ra < 10^{13}$ turbulent $Nu = 0.36 + \frac{0.518Ra_d^{1/4}}{\left[1+(0.559/Pr)^{9/16}\right]^{\frac{4}{9}}}$, $Ra \le 10^9$, Laminar
3	McAdams [28]	$Nu = 0.53(Gr \cdot Pr)^{1/4}$, $10^3 < Gr\,Pr\, < 10^9$
4	Eckert [29]	$Nu = 0.555Ra^{0.25}$
5	Morgan [30]	$Nu_D = 0.59Ra_D^{0.233}$
6	Lu et al. [32]	$\overline{Nu} = 1 \times 10^{-5}Ra^{*0.756}$
7	Dittus-Boelter [33]	$Nu = 0.023Re^{0.8}Pr^{0.4}$
8	Kuehn-Goldstein [34]	$\frac{2}{Nu_D} = ln\left[1 + \frac{2}{\left[\left\{0.518Ra_D^{0.25}\left[1+\left(\frac{0.559}{Pr}\right)^{3/5}\right]^{-5/12}\right\}^{15} + \left(0.1Ra_D^{1/3}\right)^{15}\right]^{1/15}}\right]$

A summary of the mentioned model with their proposed correlations for nucleate pool boiling in application range are presented in Table 0-2.

Table 0-2. Heat Transfer models for nucleate pool boiling in large volumes

No.	Authors	Correlation	Application range
1	Mostinski [35]	$h = 0.00417 q^{"0.7} P_c^{0.69} F_p \ . P_c[KPa]$ $F_p = 1.8P_r^{0.17} + 4P_r^{1.2} + 10P_r^{10}$	Single tube
2	Stephen and Abdelsalam [13]	$h = 0.246 \times 10^7 \left(\frac{D_b^{-0.967} T_{sat}^{0.587} q^{"0.673} C_{p.l}^{0.62} k_l^{0.967} (\rho_l - \rho_v)^{5.22}}{h_{fg}^{1.58} \rho_l^{5.86}}\right)$ $D_b = 0.0146 \times 45 \left(\frac{2\sigma}{g(\rho_l - \rho_v)}\right)^{0.5}$	Single smooth tube
3	Cooper [14]	$h = 55 P_r^{0.12 - 0.21 log_{10} R_P} (-log_{10} P_r)^{-0.55} M^{-0.5} q^{"0.67}$	Single tube including the roughness of the surface
4	Gorenflo [15]	$h = 5600 F_{PF} \left(\frac{q"}{20000}\right)^{nf}$ $F_{PF} = 1.73 P_r^{0.27} + \left(6.1 + \frac{0.68}{1 - P_r}\right) P_r^2 \ ; \ nf = 0.9 - 0.3 P_r^{0.15}$	Single tube with different material and surface roughness
5	Kutateladze [20]	$Nu = 0.44 K_*^{0.7} Pr^{0.35}$ Or $h = 0.44 \cdot \left(\frac{\lambda}{l_*}\right) \cdot \left[\frac{10^{-4} q_F p_{sat}}{gr \rho_{st} \mu} \cdot \frac{\rho_w}{\rho_w - \rho_{st}}\right]^{0.7} \cdot Pr^{0.35}$	Large volume water, clean flat heating surfaces, pressure between 1 to 225 bar.
6	Rohsenow [17]	$\frac{c_p \Delta T_b}{r} = C_{sf} \left[\frac{q_F l_*}{\mu r}\right]^{0.33} \left(\frac{c_p \mu}{\lambda}\right)^n ; h = \frac{q_F}{\Delta T_b}$ $C_{sf} = 0.008, \ n = 1$	Large volume water and other coolants (such as Ethanol, R-113, and n-Heptane), a plate heating surface, Pressure between 1 to170 bar
7	Kruzhilin [21]	$h = 0.082 \left[\frac{q_F r}{g T_{sat} \lambda} \cdot \frac{\rho_{st}}{\rho_w - \rho_{st}}\right]^{0.7} \left[\frac{T_{sat} c_p \sigma \rho_w}{r^2 {\rho_{st}}^2 l_*}\right]^{0.33} \left(\frac{\lambda}{l_*}\right) Pr^{-0.45}$	Large volume water and other coolants, a thick metal plate heating surface with different materials (Copper, Aluminum, Brass, Chromium and St.St.),

8	Labuntsov [22]	$h = 0.075\left[1 + 10\left(\frac{\rho_{st}}{\rho_w - \rho_{st}}\right)^{0.67}\right]\left(\frac{\lambda^2}{\sigma v T_{sat}}\right)^{0.33} {q_F}^{0.67}$ Or $Nu = 2{,}63^{-2}\left(\frac{\lambda \Delta T}{r \rho_{st} v}\right)^{1.86} \cdot Pr^{0.952}$	Large volume water and other coolants, a thick metal plate heating surface with different surface material and roughness.

While forced convection isn't commonly witnessed in the secondary side of ECs, it stands out as the predominant mode of heat transfer within the COSMEA test facility's secondary side. Various heat transfer models have been devised to precisely compute the heat transfer coefficient, particularly for turbulent flow within concentric annuli akin to the secondary side of COSMEA. A concise overview of these chosen models is provided in Table 0-3.

Table 0-3. Heat Transfer Models for Concentric Annular Ducts

Author(s)	**Correlations**	**Application range**
Davis [73]	$Nu_{D_h} = 0.038a^{0.15}(a-1)^{0.2}Re_{D_h}^{0.8}Pr^{1/3}(\frac{\mu}{\mu_w})^{0.14}$	$1.18 \le a \le 6800$
McAdams [28]	$Nu_{D_h} = 0.03105a^{0.15}(a-1)^{0.2}Re_{D_h}^{0.8}Pr^{1/3}(\frac{\mu}{\mu_w})^{0.14}$	$1.18 \le a \le 6800$
Dittus-Boelter [33]	$Nu_{D_h} = 0.023Re_{D_h}^{0.8}Pr^n$ $n = 0.4\ for\ heating\ ,\ n = 0.3\ for\ cooling$	$Re \ge 10^4$
Foust and Christian [74]	$Nu_{D_h} = \frac{0.04a}{(a+1)^{0.2}}Re_{D_h}^{0.8}Pr^{0.4}$	$1.2 \le a \le 1.84$
Monard and Pelton [75]	$Nu_{D_h} = 0.023[\frac{2\ln(a) - a^2 + 1}{a - \frac{1}{a} - 2a.\ln(a)}]Re_{D_h}^{0.8}Pr^n$ $n = 0.4\ for\ heating\ ,\ n = 0.3\ for\ cooling$	$a = 1.65,2.45,17$ $12000 \le Re \le 220000$
Stein and Begell [76]	$Nu_{D_h} = 0.0200a^{0.5}Re_{D_h}^{0.8}Pr^{1/3}$	$a = 1.232,1.463,1.694$ $30000 \le Re \le 390000$
Dirker and Meyer [77]	$Nu_{D_h} = C_o Re_{D_h}^{P} Pr^{1/3}\left(\frac{\mu}{\mu_w}\right)^{0.14}$ $C_o = \frac{0.003a^{1.86}}{0.063a^3 - 0.674a^2 + 2.225a - 1.157}$ $P = 1.013e^{-0.067a}$	$1.7 \le a \le 3.2$ $4000 \le Re \le 30000$

Gnielinski [78]	$Nu_{D_h} = \frac{(f_{ann}/8)RePr}{k_1 + 12.7\sqrt{f_{ann}/8}\left(Pr^{\frac{2}{3}} - 1\right)}\left[1 + \left(\frac{D_h}{L}\right)^{\frac{2}{3}}\right]F_{ann}K$ $k_1 = 1.07 + \frac{900}{Re} - \frac{0.63}{(1 + 10Pr)}$ $f_{ann} = (1.8log_{10}Re^* - 1.5)^{-2}$ $Re^* = Re\frac{(1 + a^2)lna + (1 - a^2)}{(1 - a)^2 lna}$ $K = (\frac{Pr}{Pr_w})^{0.11}$; for liquids $F_{ann} = 0.75\ a^{-0.17}$; for heat transfer at inner wall and outer wall insulated $F_{ann} = (0.9 - 0.15a^{0.6})$; for heat transfer at outer wall and inner wall insulated	$Re \geq 10^4$

Bibliography

[1] A. Bieberle, A. Moonesi Shabestary, T. Geissler, S. Boden, M. Beyer, and U. Hampel, “Flow morphology and heat transfer analysis during high-pressure steam condensation in an inclined tube part I: Experimental investigations,” *Nuclear Engineering and Design,* vol. 361, 2020.

[2] "International Atomic Energy Agancy (IAEA)," https://www.iaea.org.

[3] E. E. Michaelides, and D. N. Michaelides, “Impact of nuclear energy on fossil fuel substitution,” *Nuclear Engineering and Design,* vol. 366, pp. 110742, 2020.

[4] S. Goldberg, and R. Rosner, "Nuclear reactors: Generation to generation", American Academy of Arts and Sciences.

[5] A. Moonesi Shabestary, F. Viereckl, Y. Zhang, R. Manthey, D. Lucas, C. Schuster, S. Leyer, A. Hurtado, and U. Hampel, “Modelling of Passive Heat Removal Systems: A Review with Reference to the Framatome KERENA BWR Reactor: Part I,” *Energies,* vol. 13, no. 1, 2019.

[6] IAEA, “passive Safety Systems and Natural Circulation in Water Cooled Nuclear Power Plants,” Vienna, Austria,, 2009.

[7] R. Bryk, H. Schmidt, T. Mull, T. Wagner, I. Ganzmann, and O. Herbst, “Modeling of KERENA emergency condenser,” *Archives of Thermodynamics,* vol. 38, no. 4, pp. 29–-51, 2017.

[8] IAEA, "Passive Safety Systems in Advanced Water Cooled Reactors (AWCRs).",2013, IAEA- TE-Doc. 1705.

[9] W. Brettschuh, and K. Wagner, “SWR 1000-Das innovative Sicherheitskonzept,” *atw,* vol. 41, pp. 244–247, 1996.

[10] Y. Zhang, “Investigation of condensation process inside inclined tube,” 2020, University of Luxembourg.

[11] T. Wagner, M. Wich, M. Doll, and S. Leyer, "Full Scale Tests with the Passive Core Flooding System and the Emergency Condenser at the Integral Test Stand Karlstein for KERENA."

[12] E. Krepper, E.-F. Hicken, and H. Jaegers, “Investigation of natural convection in large pools,” *International Journal of Heat and Fluid Flow,* vol. 23, no. 3, pp. 359-365, 2002.

[13] K. Stephan, and M. Abdelsalam, “Heat-transfer correlations for natural convection boiling,” *International Journal of Heat and Mass Transfer,* vol. 23, no. 1, pp. 73-87, 1980.

[14] M. Cooper, "Heat flow rates in saturated nucleate pool boiling-a wide-ranging examination using reduced properties," *Advances in heat transfer,* pp. 157-239: Elsevier, 1984.

[15] D. Gorenflo, “Pool Boiling, VDI Heat Atlas,” *VDI-Verlag, Dusseldorf, Germany,* 1993.

[16] M.-H. Chun, and M.-G. Kang, “Effects of heat exchanger tube parameters on nucleate pool boiling heat transfer,” 1998.

[17] W. M. Rohsenow, “A method of correlating heat-transfer data for surface boiling of liquids,” *Transactions of the American Society of Mechanical Engineers,* vol. 74, no. 6, pp. 969-975, 1952.

[18] H. Forster, and N. Zuber, “Dynamics of vapor bubbles and boiling heat transfer,” *AIChE Journal,* vol. 1, no. 4, pp. 531-535, 1955.
[19] K. Cornwell, and S. Houston, “Nucleate pool boiling on horizontal tubes: a convection-based correlation,” *International journal of heat and mass transfer,* vol. 37, pp. 303-309, 1994.
[20] S. S. Kutateladze, V. M. Borishanskii, and A. d JB, “A concise encyclopedia of heat transfer,” 2021.
[21] G. Kruzhilin, “Free-convection transfer of heat from a horizontal plate and boiling liquid,” *Doklady AN SSSR (Reports of the USSR Academy of Sciences),* vol. 58, no. 8, pp. 1657-1660, 1947.
[22] D. Labuntsov, “Heat transfer problems with nucleate boiling of liquids,” *Therm. Eng.(USSR)(Engl. Transl.), v. 19, no. 9, pp. 21-28,* 1973.
[23] A. Schaffrath, and H.-M. Prasser, “Theoretical support to the NOKO experiments,” 1998.
[24] Y. Zhang, A. H. Moonesi Shabestary, A. Bieberle, U. Hampel, and S. Leyer, “Evaluation of Stratified Condensation Models for a slightly inclined tube unsing ATHELT Code,” *NURETH-18,* 2019.
[25] A. M. Shabestary, F. Viereckl, Y. Zhang, R. Manthey, D. Lucas, C. Schuster, S. Leyer, A. Hurtado, and U. Hampel, “Modelling of passive heat removal systems: a review with reference to the Framatome KERENA BWR reactor: Part I,” *Energies,* vol. 13, no. 1, pp. 35, 2020.
[26] S. W. Churchill, “Laminar free convection from a horizontal cylinder with a uniform heat flux density,” *Letters in Heat and Mass Transfer,* vol. 1, no. 2, pp. 109-111, 1974.
[27] S. W. Churchill, and H. H. Chu, “Correlating equations for laminar and turbulent free convection from a horizontal cylinder,” *International journal of heat and mass transfer,* vol. 18, no. 9, pp. 1049-1053, 1975.
[28] W. McAdams, “Heat Transmission, McGraw-Hill,” *New York,* pp. 252-262, 1954.
[29] E. R. Eckert, and R. M. Drake Jr, “Analysis of heat and mass transfer,” 1987.
[30] V. T. Morgan, "The overall convective heat transfer from smooth circular cylinders," *Advances in heat transfer,* pp. 199-264: Elsevier, 1975.
[31] Q. Men, X. Wang, X. Zhou, and X. Meng, “Heat transfer analysis of passive residual heat removal heat exchanger under natural convection condition in tank,” *Science and Technology of Nuclear Installations,* vol. 2014, 2014.
[32] D. Lu, Y. Zhang, X. Fu, Z. Wang, Q. Cao, and Y. Yang, “Experimental investigation on natural convection heat transfer characteristics of C-shape heating rods bundle used in PRHR HX,” *Annals of Nuclear Energy,* vol. 98, pp. 226-238, 2016.
[33] F. Dittus, and L. Boelter, “Heat transfer in automobile radiators of the tubular type,” *International communications in heat and mass transfer,* vol. 12, no. 1, pp. 3-22, 1985.
[34] T. H. Kuehn, and R. J. Goldstein, “Numerical solution to the Navier-Stokes equations for laminar natural convection about a horizontal isothermal circular cylinder,” *International Journal of Heat and Mass Transfer,* vol. 23, no. 7, pp. 971-979, 1980.
[35] I. Mostinski, “Application of the rule of corresponding states for calculation of heat transfer and critical heat flux,” *Teploenergetika,* vol. 4, no. 4, pp. 66-71, 1963.
[36] W. Rohsenow, J. Hartnett, and Y. I. Cho, "Handbook of heat transfer, Third Edit," McGraw-Hill, New York, 1998.
[37] I. Pioro, “Experimental evaluation of constants for the Rohsenow pool boiling correlation,” *International Journal of Heat and Mass Transfer,* vol. 42, no. 11, pp. 2003-2013, 1999.

[38] I. Pioro, W. Rohsenow, and S. Doerffer, “Nucleate pool-boiling heat transfer. II: assessment of prediction methods,” *International Journal of Heat and Mass Transfer,* vol. 47, no. 23, pp. 5045-5057, 2004.
[39] Y. Tian, Zhang, K., Wang, N., Cui, Z., & Cheng, L. , “Numerical study of pool boiling heat transfer in a large-scale confined space,” *Applied Thermal Engineering,* vol. 118, 188-198, 2017.
[40] E. Krepper, B. Končar, and Y. Egorov, “CFD modelling of subcooled boiling—concept, validation and application to fuel assembly design,” *Nuclear engineering and design,* vol. 237, no. 7, pp. 716-731, 2007.
[41] E. Krepper, and M. Beyer, “Experimental and numerical investigations of natural circulation phenomena in passive safety systems for decay heat removal in large pools,” *Nuclear Engineering and Design,* vol. 240, no. 10, pp. 3170-3177, 2010.
[42] E. Krepper, A. Schaffrath, and A. Aszódi, “Numerical simulation of the emergency condenser of the SWR-1000,” *Nuclear science and engineering,* vol. 135, no. 3, pp. 267-279, 2000.
[43] K. P. S. T. Adili, S. Leyer, A. Moonesi, “HEAT TRANSFER ASSESSMENT OF THE COSMEA TEST FACILITY COOLING SIDE

” in 19th International Topical Meeting on Nuclear Reactor Thermal Hydraulics (NURETH-19), Brussels, Belgium 2022.
[44] H. A. T. Hollands, C. Bals, S. Buchholz, S. Ceuca, H. Hristov, A. Langenfeld, P. Pandazis, S. Palazzo, J. Preuß, L. Tiborcz, S. Weber, *Validierung von Rechenprogrammen zur Simulation des Reaktorkühlkreislaufs unter Störund Unfallbedingungen,* GRS, 2016.
[45] M. T. Cichelli, and C. F. Bonilla, *Heat Transfer to Liquids Boiling Under Pressure by Mario T. Cichelli [and Charles F. Bonilla]. A Dissertation... of the Johns Hopkins University*, 1945.
[46] A. CFX, “19.1,” *ANSYS CFX-Solver Theory Guide,* 2018.
[47] T. Hibiki, and M. Ishii, “One-group interfacial area transport of bubbly flows in vertical round tubes,” *International Journal of Heat and Mass Transfer,* vol. 43, no. 15, pp. 2711-2726, 2000.
[48] K. Lawrence, *ANSYS Tutorial Release 2020*: SDC Publications, 2020.
[49] W. Lee, “A Pressure Iteration Scheme for Two-Phase Modeling. Technical Report LA-UR 79-975,” *Los Alamos, New Mexico,* 1979.
[50] S. Das, and H. Punekar, “On development of a semimechanistic wall boiling model,” *Journal of Heat Transfer,* vol. 138, no. 6, pp. 061501, 2016.
[51] M. Manninen, V. Taivassalo, and S. Kallio, “On the mixture model for multiphase flow,” 1996.
[52] L. Schiller, “A drag coefficient correlation,” *Zeit. Ver. Deutsch. Ing.,* vol. 77, pp. 318-320, 1933.
[53] T. Frank, J. Shi, and A. D. Burns, "Validation of Eulerian multiphase flow models for nuclear safety application." pp. 22-25.
[54] A. D. Burns, T. Frank, I. Hamill, and J.-M. Shi, "The Favre averaged drag model for turbulent dispersion in Eulerian multi-phase flows." pp. 1-17.
[55] H. Scholz, “Modellierung und Untersuchung des Wärme-und Stofftransports und von Flutungsphänomenen in Niedertemperatur-PEM-Brennstoffzellen,” *Diss. RWTH Aachen,* 2015.
[56] J. E. Matsson, *An Introduction to Ansys Fluent 2023*: Sdc Publications, 2023.

[57] A. Fluent, “ANSYS Fluent Theory Guide, ANSYS,” *Inc., Release,* vol. 15, 2013.
[58] N. Kurul, and M. Z. Podowski, "Multidimensional effects in forced convection subcooled boiling."
[59] V. H. Del Valle, and D. Kenning, “Subcooled flow boiling at high heat flux,” *International Journal of Heat and Mass Transfer,* vol. 28, no. 10, pp. 1907-1920, 1985.
[60] M. Lemmert, and J. Chawla, “Influence of flow velocity on surface boiling heat transfer coefficient,” *Heat Transfer in Boiling,* vol. 237, no. 247, 1977.
[61] V. Tolubinsky, and D. Kostanchuk, "Vapour bubbles growth rate and heat transfer intensity at subcooled water boiling."
[62] H. Ünal, “Maximum bubble diameter, maximum bubble-growth time and bubble-growth rate during the subcooled nucleate flow boiling of water up to 17.7 MN/m2,” *International Journal of Heat and Mass Transfer,* vol. 19, no. 6, pp. 643-649, 1976.
[63] W. Friz, “Maximum volume of vapor bubbles,” *Physic. Zeitschz.,* vol. 36, pp. 379-354, 1935.
[64] R. Cole, “A photographic study of pool boiling in the region of the critical heat flux,” *AIChE Journal,* vol. 6, no. 4, pp. 533-538, 1960.
[65] A. Schaffrath, *Experimentelle und analytische Untersuchungen zur Wirksamkeit des Notkondensators des SWR600*, Jülich Forschungszentrum Zentralbibliothek, JuSER: Jülich, Germany, 1997.
[66] S. Kumar, P. Vijayan, U. Kannan, M. Sharma, and D. Pilkhwal, “Experimental and computational simulation of thermal stratification in large pools with immersed condenser,” *Applied Thermal Engineering,* vol. 113, pp. 345-361, 2017.
[67] T. Calisir, A. B. Colak, D. Aydin, A. S. Dalkilic, and S. Baskaya, “Artificial neural network approach for investigating the impact of convector design parameters on the heat transfer and total weight of panel radiators,” *International Journal of Thermal Sciences,* vol. 183, pp. 107845, 2023.
[68] M. Mohanraj, S. Jayaraj, and C. Muraleedharan, “Applications of artificial neural networks for thermal analysis of heat exchangers–a review,” *International Journal of Thermal Sciences,* vol. 90, pp. 150-172, 2015.
[69] S. Mohanty, “ANFIS based prediction of monthly average global solar radiation over Bhubaneswar (State of Odisha),” *Int. J. Ethics Eng. Manag. Educ,* vol. 1, no. 5, pp. 97-101, 2014.
[70] B. Vaferi, F. Samimi, E. Pakgohar, and D. Mowla, “Artificial neural network approach for prediction of thermal behavior of nanofluids flowing through circular tubes,” *Powder technology,* vol. 267, pp. 1-10, 2014.
[71] S. A. Kalogirou, “Artificial intelligence for the modeling and control of combustion processes: a review,” *Progress in energy and combustion science,* vol. 29, no. 6, pp. 515-566, 2003.
[72] E. M. Azoff, *Neural network time series forecasting of financial markets*: John Wiley & Sons, Inc., 1994.
[73] E. S. Davis, “Heat transfer and pressure drop in annuli,” *Transactions of the American Society of Mechanical Engineers,* vol. 65, no. 7, pp. 755-759, 1943.
[74] A. Foust, and G. Christian, “Non-boiling heat transfer coefficients in annuli,” *American Institute of Chemical Engineers,* vol. 36, pp. 541-554, 1940.
[75] C. Monrad, “Heat transfer by convection in annular spaces,” *Trans. AIChE,* vol. 38, pp. 593-611, 1942.

[76] R. P. Stein, and W. Begell, “Heat transfer to water in turbulent flow in internally heated annuli,” *AIChE Journal,* vol. 4, no. 2, pp. 127-131, 1958.
[77] J. Dirker, and J. P. Meyer, “Convective heat transfer coefficients in concentric annuli,” *Heat Transfer Engineering,* vol. 26, no. 2, pp. 38-44, 2005.
[78] V. Gnielinski, “Heat transfer coefficients for turbulent flow in concentric annular ducts,” *Heat transfer engineering,* vol. 30, no. 6, pp. 431-436, 2009.